SHORT ELECTRODYNAMIC TETHERS

ESTEC Contract No. 13395/98/NL/MV

Final Report for Work Packages 100 and 300

Juan R. Sanmartín
Eduardo Ahedo
Luis Conde
Jesús Peláez
Manuel Ruiz

July 13, 1999

Prepared for:

Marc Weinberger
Alain Hilgers
European Space Agency
ESTEC

Escuela Técnica Superior de Ingenieros Aernáuticos
Universidad Politécnica de Madrid
Pl. Cardenal Cisneros, 3
28040 Madrid
SPAIN

SHORT ELECTRODYNAMIC TETHERS

WP-100 (110-120) *and* 300. *Final Report*

J. R. Sanmartín

E. Ahedo

L. Conde

J. Peláez

M. Ruiz

1 Preliminary Considerations

* *Short tethers*: A short deorbiting tether, as contemplated in this Study, faces three basic difficulties:

i) The greatest difficulty lies in the fact that the braking force is

Magnetic drag ~ Current × Geomagnetic field × Length ≡ IBL.

Since B is given, and collecting electron (anodic) current from the ambient plasma is hard,

a short length will probably mean a weak drag.

Forward et al. [1] stated that the drag of a deorbiting tether depends on its mass but not on its length. This results from assuming the collection impedance negligible against the ohmic impedance no matter how large the current, which does not seem to make sense. Taking L = 50 m in their example of a 10 Kg aluminum tether driven by a 136 V/Km induced field, the collection impedance for the corresponding current, I = 370 A, would have to be small compared to the ohmic resistance for that short length (and large cross-section area), which is 0.0185 Ω! Assuming both impedances comparable for all lengths [2] does not modify our conclusion.

ii) The induced voltage is

Induced Voltage ~ Orbital speed × Magnetic field × Length ≡ $v_{sat}BL$.

Since both v_{sat} and B are given,

a short tether will need a voltage (power) source to drive the current.

($v_{sat}BL \sim 20$ V for $L \sim 100$ m and an induced field ~ 200 V/Km).

iii) Until recently, the problem of anodic collection was supposed to be solved by using either large metallic spheres or inflatable balloons [3, 4], or plasma-emiting contactors. An alternative concept, the bare-tether, would use a positively biased

segment of the tether itself (lacking insulation) to capture electrons as a large and efficient cylindrical Langmuir probe; the fact that this concept has revitalized tether electrodynamics suggests anodic plasma contactors are not convincingly efficient. However,

a tether too short might not profit from the bare-tether scheme,

which follows the collection law

Current to a bare tether ~ √Bias × Plasma density × Perimeter × Length.

(The advantage of bare tethers against another type of passive anode, the large TSS1 collecting sphere, rests in geometry effects on plasma kinetics, not in some common surface-physics effects revealed by TSS1R flight data, as suggested in Ref. 1).

* *High inclinations*: The usual vertical orientation of tethers will probably not work for the high orbital inclinations considered, for which the geomagnetic field is close to the orbital plane. This motivates the use of short tethers, ending in no single deorbiting scheme working for both the lower and the higher inclination ranges. At the proper orientation the tether may not benefit from gravity-gradient pulling, and may need to be rigid, and thus probably short. A short, rigid tether could be given an optimal orientation, although some sort of control might be needed.

* *Low masses*: A short, light tether maybe an optimal system for deorbiting small satellites. Also, a rigid tether may be a robust system, free of the instabilities inherent to the operation of flexible tethers, and highly reliable as regards both deployment and survival against space debris. In addition, it would barely increase the cross-section area of its spacecraft as a debris itself.

* *High altitudes*: At the high LEO altitudes contemplated in the study, plasma density is both more dependent on solar activity and smaller than in the F-layer. This might

limit use of a short-tether deorbiting scheme to part of the solar cycle. The fact that at such altitudes hydrogen, rather than oxygen, is the dominant ion species, may have effects of interest, too.

* *References*:

[1] R.L.Forward, R.P.Hoyt, and C.Uphoff, "The Terminator Tether: A Near -Term Commercial Application of the NASA/MSFC ProSEDS Experiment", Proc. Tether Technology Interchange Meeting, NASA/CP-1998-206900, 109-129 (1998).

[2] R.L.Forward, R.P.Hoyt, and C.Uphoff, "Application of the Terminator Tether Electrodynamic Drag Technology to the Deorbit of Constellation Spacecraft", Proc. 34th Joint Propulsion Conference, Cleveland, OH, 13-15 July 1998, AIAA 98-3491.

[3] L.Iess et al., "Satellite Deorbiting by means of Electrodynamic Tethers: General Concepts and Requirements", 49th Int. Astron. Congress, Melbourne, Australia, Sept.28-Oct 2, 1998.

[4] L.Iess et al., "Satellite Deorbiting by means of Electrodynamic Tethers: System Configuration and Performance", 49th Int. Astron. Congress, Melbourne, Australia, Sept.28-Oct 2, 1998.

2 Short Tether Concept

* A mass M under a weak tether magnetic drag, in circular orbit, descends at a rate

$$\frac{1}{2} M\Omega \frac{da}{dt} = \frac{\bar{v}_{sat} \cdot \bar{F}}{v_{sat}}, \qquad (v_{sat} = a\Omega, \quad \Omega^2 a^3 = \Omega_E{}^2 R_E{}^3 = GM_E), \tag{1}$$

R_E and M_E being Earth radius and mass, and a and Ω orbital radius and angular velocity. We then write

$$\bar{v}_{sat} \cdot \bar{F} = \bar{v}_{sat} \cdot \int Id\bar{u}_T \wedge \bar{B} \equiv -\tilde{I} E_m L . \tag{2}$$

Here $\tilde{I}$ is the current averaged over the tether (allowing for bare-tether collection); $\bar{u}_T$ is the unit vector along the wire such that $\tilde{I} > 0$; and the induced electric field is

$$E_m \equiv \bar{u}_T \cdot (\bar{v}_{sat} \wedge \bar{B}) \tag{3}$$

* We will use the dipole model of the geomagnetic field

$$\bar{B} = B_{eq}(a)\{3(\bar{u}_m \cdot \bar{i})\bar{i} - \bar{u}_m\} = -B_{eq}(a)[2A_1\bar{i} + A_2\bar{j} + A_3\bar{k}], \tag{4}$$

$$B_{eq}(a) \equiv B_0 \frac{R_E{}^3}{a^3}, \qquad (B_0 = 0.31 \text{ gauss})$$

where B_{eq} is the field at the magnetic equator; $\bar{u}_m$ is the dipole unit vector, forming a small angle $\beta_m \approx 11.5° \approx 0.20$ radians, with the vector to the geographical South pole; and $\bar{i}$ (upward local vertical), $\bar{j}$ (horizontal and perpendicular to the orbital plane), and $\bar{k}$ ($\equiv \bar{v}_{sat}/v_{sat}$) are unit vectors in the orbital frame. One finds

$$A_1 \equiv \cos\beta_m \sin i \sin\theta + \sin\beta_m (\cos\theta \cos\varphi + \cos i \sin\theta \sin\varphi), \tag{5a}$$

$$A_2 \equiv \cos\beta_m \cos i - \sin\beta_m \sin i \sin\varphi, \tag{5b}$$

$$A_3 \equiv -\cos\beta_m \sin i \cos\theta + \sin\beta_m (\sin\theta \cos\varphi - \cos i \cos\theta \sin\varphi), \tag{5c}$$

where i is the geographical inclination; $d\theta/dt$ is Ω, with $\theta = 0$ at the ascending node; and $d\varphi/dt$ is the difference between the rotation rates of Earth and orbital line of nodes (caused by the J_2-term in the Earth's gravitational field). One then has

$$\tilde{I}E_m = v_{sat}B_{eq}\tilde{I}\,\bar{u}_T \bullet \left[A_2\,\bar{i} - 2A_1\bar{j}\right], \qquad (6)$$

* Note that coefficient A_2 in Eq. (6) oscillates in time with a period of 24 hours, while A_1 oscillates with the orbital period (1½ - 2 hours). For current driven by the induced voltage E_mL, the direction of $\bar{u}_T$ at any given tether orientation naturally makes E_m positive in (6), resulting in continuous drag ($\bar{v}_{sat} \bullet \bar{F} < 0$); a voltage source, if dominant in driving the current, can achieve the same result by proper electrical switching. For the constant vertical orientation of usual tethers one should have $\bar{u}_T = \bar{i}$ × sign (A_2), or $\bar{u}_T \bullet \left[A_2\,\bar{i} - 2A_1\bar{j}\right] = |A_2|$, at all times. For $i < \pi/2 - \beta_m$, A_2 is positive throughout; using $<>$ to denote averages over 1 orbit, we have

$$\langle \tilde{I}\,\bar{u}_T \bullet \left[A_2\,\bar{i} - 2A_1\,\bar{j}\right]\rangle = \langle \tilde{I}\,|A_2|\rangle = \tilde{I}_{av}\cos i, \qquad (7)$$

with $\tilde{I}_{av}$ the orbit-averaged current. Equation (7) is correct to terms of order β_m, but its day-average is correct to higher order, because the second term in (5b), which oscillates with φ, will almost average out. For $\pi/2 - \beta_m < i < \pi/2$, $\bar{u}_T$ will be opposite $\bar{i}$ over part of each day, with the day-average of $\langle \tilde{I}\,|A_2|\rangle$ reaching a minimum for polar orbits,

$$\text{Minimum of } \langle \tilde{I}\,|A_2|\rangle \approx \tilde{I}_{av}\sin\beta_m \langle|\sin\varphi|\rangle = \tilde{I}_{av}\frac{2}{\pi}\sin\beta_m, \qquad \text{at } i = 90^\circ, \qquad (7')$$

where we took $\tilde{I}_{av}$ constant over 1 day for simplicity. Similar results hold for $\pi/2 < i < \pi$.

* If one wished to make the drag as large as possible, the tether should rotate (in the orbiting frame) to keep parallel to the slowly varying $A_2\bar{i} - 2A_1\bar{j}$, with $\bar{u}_T$ pointing always in the proper direction. We would then have, to order β_m^2,

$$\langle \tilde{I}\bar{u}_T \bullet \left[A_2\,\bar{i} - 2A_1\,\bar{j}\right]\rangle \approx \tilde{I}_{av}\,\langle\sqrt{\cos^2 i + 4\sin^2 i \sin^2\theta}\,\rangle \equiv \tilde{I}_{av}K(i). \qquad (7a)$$

$K(i)$, given in terms of the complete elliptic integral of the second kind, varies from $K(0°) = 1$ to $K(90°) = 4/\pi$. Clearly, cumbersome tether rotations are not justified for low inclinations, for which the law (7) for the stable vertical orientation is close to (7a).

* For high inclinations, one can also make do without tether rotation by making the tether lie along $\bar{j}$ (tether horizontal, and perpendicular to the orbital plane), with the direction of current switching back and forth, twice along the orbit, when $sin\theta$ changes sign. For not too low inclinations, one finds

$$\langle \tilde{I}\bar{u}_T \bullet \left[A_2 \bar{i} - 2A_1 \bar{j} \right] \rangle = 2\langle \tilde{I} \left| A_1 \right| \rangle \approx \tilde{I}_{av} \frac{4}{\pi} sini . \qquad (7b)$$

At $i = 90°$, (7b) exceeds (7') by a factor $2/sin\beta_m \approx 10$. Note, however, that this is an unstable orientation, the gravity gradient force being here a compressive force. This will limit the tether length, making necessary the use of a voltage source.

Figure 2.1 shows laws (7, 7') - for the full i range -, (7a), and (7b), for the angle factor multiplying $\tilde{I}_{av}$, which is $E_m/v_{sat}B_{eq}$. Although the rotating-tether law (7a) is optimal, one can avoid rotation for all inclinations, by using the close and simpler law (7, 7') with long, flexible, vertical tethers, for $i < 45°$; and (7b) with short, rigid, horizontal tethers, for $45° < i < 90°$.

* Using then Eqs.(1), (2), (6) and (7b), one finds the average rate of descent,

$$\frac{1}{2} M\Omega_E \langle \frac{da}{dt} \rangle = -\tilde{I}_{av} B_0 L \times \left(\frac{R_E}{a} \right)^{3/2} \times \frac{4}{\pi} sini . \qquad (8)$$

The rate of descent scales simply with total satellite mass M, (twice averaged) tether current $\tilde{I}_{av}$, length L, and orbital inclination; at $i = 70°$ the rate is smaller by 6 %. For both drag laws (7, 7') and (7a) the inclination is found to (slowly) approach 90°. With our law (7b), however, the rate di/dt actually vanishes: The rate of change of orbital inclination for a small perturbing (here tether) force comes from its projection onto the

normal to the orbital plane, which of course vanishes in our case if the tether does keep in its nominal orientation.

Taking, as an example, initial radius $a_0 = R_E + 1600$ Km and

$$i = 90°, \quad \tilde{I}_{av} = constant = 1 \text{ A}, \quad L = 200 \text{ m}, \quad M = 500 \text{ Kg}, \tag{9}$$

with $R_E = 6370$ Km, $\Omega_E = 1.24 \times 10^{-3}$ s^{-1}, the time to drop to 800 and 250 Km would be

$$\Delta t = 1.29 \text{ and } 2.06 \text{ years},$$

respectively. We also find drag values,

$$- <\bar{v}_{sat} \bullet \bar{F}>/v_{sat} \approx 4.0 \text{ mN and } 7.0 \text{ mN},$$

at 1600 and 250 Km, respectively; and corresponding induced voltages,

$$<E_m>L = 28.5 \text{ V and } 54.5 \text{ V}.$$

At a 250 Km height, the lifetime of satellite + tether would be a few days at most.

* *For the high i range, we propose using two uninsulated tethers of length $L/2$, one on each side of the spacecraft, carrying identical plasma contactors at the ends.* The two tethers would be electrically connected to a power source of voltage V_S at the spacecraft. At any given half-period, and for negligible ohmic resistance and (moderately) small induced voltage E_mL, one (anodic) tether would be biased at a near uniform potential $\Phi_a > 0$, collecting a bare-tether current $I_{BT}(\Phi_a)$ over its $L/2$ length, and a small electron current $I_a(\Phi_a)$ at its contactor [1]. The opposite (cathodic) tether would be polarised at a near uniform bias $\Phi_c < 0$, and collect a negligible ion current over its length, ejecting an electron current

$$I_c(\Phi_c) = I_a(\Phi_a) + I_{BT}(\Phi_a) \tag{10}$$

at its end contactor, with

$$\Phi_a - \Phi_c \approx \Phi_a + |\Phi_c| = V_S + E_mL. \tag{11}$$

Anodic tether and contactor appear connected in parallel, and its arrangement connected in series to the cathodic contactor (Fig. 2.2). In the next half-orbit, electrical switching would reverse the direction of the current and the way each tether works, so as to indeed have drag (rather than thrust) all the time.

* As shown in Fig. 2.2, the current flowing along the tether on the anodic side would vary linearly from the anodic end ($I = I_a$ at, say, $y = - L/2$) to the satellite at the middle ($I = I_c$ at $y = 0$). In drawing that figure we ignored both the induced voltage $E_m L$, and the very small ohmic drop. The average current would thus be

$$\tilde{I} = I_a + 3I_{BT}/4. \qquad (12)$$

Note that, as long as there is bare-tether current, the magnetic torques acting on both tethers are unequal. The net torque is proportional to a tether 'magnetic moment', $I_{BT} L^2/12$. This torque would be reversed every half-orbit, as a result of the oscillation of the magnetic field in the orbital frame, and might have an effect on the attitude stability of the tether (see Sec.7).

* In conclusion, a tether horizontal and perpendicular to the orbital plane is optimally oriented for getting maximum drag at high inclinations (with a factor of about 10 in drag gain over vertical tethers), but it faces several difficulties. To some extent, however, there may be ways out of those difficulties.

i) The horizontal tether is in unstable equilibrium even in the absence of net magnetic torque: The tether might be stabilised at some energy cost by making it spin around its axis (Thomson stability); see Sec. 7.

ii) The horizontal tether is under compression from the gravity gradient; it must thus be rigid: A rigid-tether system can be more robust and reliable than the usual flexible (vertical) tethers. There exist long masts or booms that are flexible when rolled

up around a drum and rigid when deployed, deployment having been proved and validated in space. Also, rigid masts are free of the instabilities that plague flexible tethers.

iii) *The tether cannot be too long, to avoid structural problems such as buckling. This results in low anodic bare-tether collection, low drag, and low induced voltage*: While a short tether will deorbit slowly, it will also survive longer against space debris; in addition, it will keep current moderately high by allowing a large perimeter p with no penalty from a large tether mass. With a solar-power voltage source (V_S) to enhance the current, a fraction $\sim E_m L/V_S$ of that power would go into magnetic braking.

* *References*

[1] J.R.Sanmartín, M.Martínez-Sánchez, and E.Ahedo, J. Propul. Power **9**, 353 (1993).

3 Tether Design and Performance

* *Bare Tether Current*

As discussed in Sec.5, the collection impedance of a bare tether is small compared with the anodic contact impedance, $I_{BT} >> I_a$, Eq.(2.10) then reading

$$I_c(\Phi_c) \approx I_{BT}(\Phi_a). \tag{1}$$

On the other hand, the impedance of cathodic contactors is small compared with that of bare tethers if short (Sec.4), Eq.(1) then giving $\Phi_a >> |\Phi_c|$. Equation (2.11) now reads

$$\Phi_a = V_S + E_m L - |\Phi_c| \approx V_S. \tag{2}$$

The current-voltage characteristic of a bare tether then determines the current, $I_{BT}(V_S)$. Also, the small current to the anodic contactor can follow if its characteristic is approximately known, while the cathodic characteristic would just yield Φ_c in (1), leading to a small correction to Φ_a in Eq.(2.11). The simplicity and certainty of bare-tether current collection thus allows a detailed, though approximate, discussion of tether design and system capabilities in the face of considerable uncertainties in active contactors.

* The electron current to a long, circular cylinder at rest in an unmagnetized Maxwellian plasma of density N_∞ and temperatures T_e and T_i, may be written as

$$I/I_{th} = a\ function\ of\ (e\Phi_a/kT_e,\ R/\lambda_{De},\ T_i/T_e), \tag{3}$$

where $I_{th} \equiv surface\ area \times eN_\infty \sqrt{kT_e / 2\pi m_e}$ is the random current to the wire, R and Φ_a are wire radius and positive bias, and $\lambda_{De} \equiv \sqrt{kT_e / 4\pi e^2 N_\infty}$ is the Debye length. We note, however, that there exists a domain in the dimensionless parameter space $(e\Phi_a/kT_e, R/\lambda_{De}, T_i/T_e)$ where I/I_{th} depends only on $e\Phi_a/kT_e$; this is the orbital-motion-

limited (OML) regime of cylindrical Langmuir probes. For large $e\Phi_a >> kT_e$, in particular, one has

$$I/I_{th} = I_{OML}/I_{th} \approx \sqrt{\frac{4e\Phi_a}{\pi\, kT_e}}, \qquad (4)$$

$$I_{OML} \approx \frac{perimeter}{\pi} \times length \times eN_\infty \sqrt{\frac{2e\Phi_a}{m_e}}. \qquad (4')$$

* The fact that the current law is independent of the ratios R/λ_{De} and T_i/T_e in some proper domain means that one could substantially alter plasma and cylinder parameters, thus fully modifying the structure of the potential field, without reaching the boundary of the OML domain, that is, keeping (4) valid. This is a case quite opposite to that of large spherical collectors, as used in the TSS1 tethers.

The OML current law (4) is valid in a broad parameter domain. For given $e\Phi_a/kT_e$ and T_i/T_e, the law is valid for R less than some value R_{max}. In particular, for $T_i/T_e \sim 1$ (the ionospheric case) and $e\Phi_a/kT_e \sim 10^3$ (corresponding to $\Phi_a \approx V_s \sim 200$ V, $kT_e \sim 0.2$ eV) one finds $R_{max} \approx \lambda_{De}$ [1].

Actually, the current keeps close to the OML value for some range $R_{max} < R < \tilde{R}_{max}$. For $T_i/T_e \sim 1$ and $e\Phi_a/kT_e \sim 10^3$, one finds $\tilde{R}_{max} \approx 3.4\, \lambda_{De}$. Beyond $R = \tilde{R}_{max}$, I/I_{OML} drops fast with increasing R (the current growing too slowly with R, $I \propto R^{1/4}$) [2]; this results in a lower current-to-mass wire ratio, reducing the collection efficiency of the wire.

* The OML law is quite robust. It is independent of the cross-section shape of the cylinder if convex enough, as emphasized by the way we wrote Eq.(4') [3]. It will apply to a tether if uninsulated (bare), whether in the shape of a wire or, for instance, a tape. It has been found that a thin tape of full width $4R$ behaves as a wire of radius R

as regards OML validity [1]. Bare tethers prove quite useful for electrodynamic applications, where substantial electron collection from the ionosphere is required [4-6].

* In the case of an orbiting bare tether, one must consider additional effects, both due to its motion relative to the plasma (effect of ion ram energy), and to the geomagnetic field. We note in this respect that:

1) The law is independent of the ion distribution function in the unperturbed plasma. It will apply for an orbiting tether even if the characteristic ram energy is large compared with the thermal energy, implying a strongly nonisotropic ion distribution function, as in the F-layer, where the ram energy of oxygen ions is

$$\tfrac{1}{2} m_i v_{sat}^2 \approx 4.5 \text{ eV} >> kT_i \approx 0.15 \text{ eV}.$$

Note that, at high bias, the OML law is also independent of the unperturbed electron distribution function, as long as it is isotropic, as in the case of an orbiting tether (v_{sat} << electron thermal velocity). Note, in particular, that T_e does not appear in (4').

2) The law applies even if the potential has no rotational symmetry, as in the case of a tape. It may thus hold in the presence of a magnetic field, or with an electric field that exhibits ram and wake behavior.

3) Ram energy and magnetic effects then just result in a reduction of the domain of validity of Eq.(4). Magnetic effects are weaker when the tether keeps perpendicular to the magnetic field, as in our case; one can then roughly say that (4) is valid if neither R nor λ_{De} approach the thermal electron Larmor radius [1]. Concerning ram effects, (4) is valid, for $R/\tilde{R}_{max}$ below unity, at altitudes in the range 800-2000 Km, where H^+

instead of O^+ is the dominant ion especies, and v_{sat}^2 and $1/T_i$ are somewhat lower than in the F-layer, the ram energy then being about thermal (weak anisotropy).

* It has been suggested (Ref.1 in Sec.1) that use of a multiline bare-tether (a mesh of wires) would collect current proportional to the width of the mesh; this might then result in large currents with light tethers, even at very low densities. Actually, OML theory, arising from simple conservation laws (particle energy, velocity along cylinder axis, and distribution function - through the Vlasov equation -), shows that the perimeter to use in Eq. (4') is the *actual physical* perimeter p [1]. Further, for two bare tethers not to interfere in collection their distance should be larger than about $\frac{1}{2}p\sqrt{e\Phi_a / kT_e} \sim 1$ m, rather than $\lambda_{De} \sim 1$ cm, as suggested in Ref.1 of Sec.1. This makes multiline tethers problematic. Also, use of two parallel tethers here appears difficult.

* *Tether Design*

Actually, our tether, as noted in Sec.2, could not be a wire or a flexible tape, which would buckle under gravity-gradient compression. One should use, instead, long masts or booms that may be stored during launch and are rigid when deployed. Slender rods have been repeatedly used as antennas or for 'inertia augmentation' purposes; the Radio Astronomy Explorer satellite (RAE, 1968), for instance, used an antenna made of two booms, 460 m tip to tip (and a 96 m damper boom to help in gravity stabilisation). A technology of long, light-weight tubes has been developed for space applications [7, 8]. Note that our possible use of this technology would pose very weak alignment requirements, as compared with scientific or communication uses.

* Such tubes need not have circular cross-sections, a particular European example being Sener's CTM family of masts [9]. In using them as electrodynamic tethers, note first, as regards the domain of OML validity, that results on maximum

radius for a wire R_{max}, or $\tilde{R}_{max}$, may be extended to cover other convex cross-sections. For elliptical shapes, one finds the simple correspondence $\frac{1}{2}(a_e + b_e) \rightarrow R$, with a_e and b_e the semiaxes of the ellipse; the perimeter is $p = 4a_eE(m)$, where E is the complete elliptical integral of the second kind, and $m \equiv 1 - b_e^2/a_e^2$ its *parameter*. This leads to

$$p = \frac{8E(m)}{1+b_e/a_e}R, \qquad (m \equiv 1-\frac{b_e^2}{a_e^2}); \tag{5}$$

for the limit case of a thin tape ($b_e = 0$) one would find the known result, $p = 8R$ [1]. For a given plasma density (i.e., a given λ_{De}), the approximate condition $R < 3\lambda_{De}$ determines in (5) an upper bound for perimeter of ellipses of given eccentricity.

* The cross-section of a tube mast in SENER's CTM family has two symmetry axes, C and H being the dimensions along axes, with a ratio $H/C \approx 0.70$. (For structural reasons, cross-sections in the family are geometrically similar, all CTM properties, including mass per unit length, profile thickness, stiffness around axes, etc, being readily scaled). Taking $C/2$ and $H/2$ as semiaxes of an ellipse, we have $m = 0.51$, $E(m) \approx 1.35$, Eq.(5) then yielding $p \approx 6.35\,R$ (very close to the circle limit) and an upper bound,

$$p < 19.0\,\lambda_{De}. \tag{6}$$

As regards the use of the OML law itself, Eq.(4'), note that the law fails at too large a cross-section ($R > R_{max}$ -or $R > \tilde{R}_{max}$- in the case of wires) because of behavior in the faraway perturbed potential, which only depends on gross features of the cross-section, in addition to size (this allowed approximating the CTM cross-section as an ellipse). On the other hand, the OML law also fails, independently of size, for cross-sections that are not convex everywhere, which is the CTM case. The OML law,

however, remains very approximately valid if one uses as *perimeter* in Eq.(4'), not the actual value p but the value p^* for the minimum-perimeter convex envelope of the actual cross-section. For the CTM masts one finds that this modified perimeter is very close to p,

$$p^* \approx 0.92p. \qquad (7)$$

* Assuming that a possible dynamical instability of the Thomson-spinning tether can be avoided (see Sec.7), an upper bound to mast length is placed, for each cross-section, by the need to avoid buckling caused by the gravity-gradient compressive force; with the mast spinning, its bending due to the transverse magnetic force should be small. Euler's critical force for buckling is proportional to Young's modulus E, moment of inertia of the cross-section I_{sec}, and inverse squared mast length, while the compressive force is proportional to mast length and mass,

$$EI_{sec}/(L/2)^2 \sim F_{cr} \sim \Omega^2 \times L/2 \times \rho p t L/2, \qquad (8)$$

with $I_{sec} \sim p^3 t$ (ρ and t are mast density and thickness). This yields a critical tether length

$$L_{cr}^2 \sim p\sqrt{E}/\Omega^2\rho. \qquad (9)$$

Since $p_{max} \sim \lambda_{De} \sim 1/\sqrt{N_\infty}$, the maximum plasma density allowing OML collection (whatever the safety factor used for buckling) decreases fast with increasing mast length,

$$Max\ N_\infty\ for\ OML\ current \sim 1/L^4. \qquad (10)$$

* The smallest cross-section (Size 1) in the CTM family has $C = 3.08$ cm, $H = 2.16$ cm, $p = 8.32$ cm (perimeter of corresponding ellipse = 8.29 cm) and $p^* = 7.65$ cm. From (6) one finds $\lambda_{De} \approx 0.44$ cm; this Debye length corresponds to a plasma density $N_\infty \approx 5.7 \times 10^5$ cm^{-3} (for $T_e = 0.2$ eV). The simple relation (9) (with no

numerical factors) gives a critical mast length $L_{cr}/2 \sim 265$ m; considering buckling with a (full) contactor mass equal to mast mass, reduces $L_{cr}/2$ to 225 m. A more detailed estimate (WP-200 Report) gives $L_{cr}/2 \sim 175$ m. With a profile thicknes of 0.05 mm, the Size-1 CTM mast, made of Beryllium (and Copper), has a mass per unit length of 34.3 g/m; two such masts of length $L/2 = 125$ m (for which the gravity-gradient compressive force is 1/5 Euler's critical value), one on each side, would make a total tether mass of 8.6 kg. The electric resistance of the full two-mast tether would be negligible ($\approx 1\ \Omega$).

* *Tether Performance*

Since our bias Φ_a is approximately fixed at the value V_S, the current $I_{BT} \approx I_{OML}$ depends just on N_∞, which is the critical parameter. A drawback of the bare tether in our scheme is that its collection length is fixed, and thus the current I_{BT} decreases as N_∞ (bare tethers used for power generation or propulsion can adjust to drops in plasma density). Most of the deorbiting life of the spacecraft would then take place at the upper altitudes. Between, say, 800 and 2000 Km, N_∞ is nearly independent of height, but shows substantial day-night and latitude variations. More troubling, at those heights (even down to 600 Km) and the high latitudes of interest for our high inclination orbits, N_∞ is strongly dependent on solar activity. This means that, except for the lowest initial altitudes, the rate of descent will be greatly affected by the phase of the solar cycle, our scheme, possibly, being only valid for part of that cycle.

In our calculations we used the best ionospheric model available, the International Reference Ionosphere (IRI) 95, developed over the last 30 years [10]. IRI 95 is currently regarded as the standard model to predict environment plasma conditions for platforms, in both polar and low inclination orbits [11]. Although quantitative uncertainties remain, specially so at high latitudes in the topside and plasmaspheric ionosphere, and

interpolation in the numerical model allows for some artificial discontinuities in density profiles, IRI 95 should give reliable results for the long-average calculations required here.

* Figures 3.1 and 3.2 show IRI profiles for N_∞ versus latitude at 1600 km height and 0:0:0 UT, for a few longitudes (this being roughly equivalent to giving day-night variations). The two dates correspond to end of the solar-cycle minimum and beginning of maximum. Differences are moderate at low latitudes, but dramatic at high latitudes, where $|A_1|$ in Eq.(6) of Sec.2 is maximum. With $|A_1| \approx sini\ |sin\theta|$, the proper average for the rate of descent when Eq.(4') is used gives

$$\frac{1}{2} M\Omega_E \left\langle \frac{da}{dt} \right\rangle = -\ \tilde{I}_{ref}\ B_0 L \left(\frac{R_E}{a} \right)^{3/2} \times \langle \frac{N_\infty}{N_{\infty ref}} |sin\theta| \frac{\pi}{2} \rangle \times \frac{4}{\pi}\ sini\ , \qquad (11)$$

to be compared with Eq.(8) in Sec.2. Here, $\tilde{I}_{ref}$ is $\tilde{I}$ (= ¾ I_{BT} + I_a) at some reference density $N_{\infty ref}$; as we shall see in Sec.5, a reasonable though crude model for the small current to an active anode, gives $I_a \propto N_\infty$, as with passive, bare-tether collection. For polar orbits, θ in Eq.(11) is just the latitude. Figures 3.3 and 3.4, giving $N_\infty\ |sin(latitude)|\ \pi/2$ for the conditions of Figs.3.1 and 3.2, show a extreme latitude dependence; the effect will be smaller at lower inclinations (and the more so for vertical tethers).

Figures 3.5-3.12 show N_∞ at 800, 600, 400, and 300 Km altitudes, for the same conditions of Figs.3.1, 3.2. Basic features of these last figures are still found down at 800 Km: equatorial densities quite similar at solar minimum and maximum, polar densities 1½ orders of magnitude larger at solar maximum. Actually, N_∞ appears to be nearly independent of altitude in the range 800-1600 Km. This is clearly shown in Figs.3.13, 3.14 for a high latitude. At 600 Km, and the more so at 400 Km, low latitude

densities are substantially larger at solar maximum; also, at the lower altitudes, equatorial densities keep larger than polar densities at both solar maximum and minimum. Note finally that at low latitudes, and contrary to the case of Figs.3.13, 3.14, the density increase for height decreasing below 800 Km is very large.

* The strong latitude dependence in Figs.3.2, 3.6, 3.8, is a hindrance to our scheme. Since both R_{max} and $\tilde{R}_{max}$ decrease with $\lambda_{De} \propto 1/\sqrt{N_\infty}$, the perimeter will be limited by the maximum densities to consider; clearly, flatter N_∞-profiles (at the same N_∞-average) would had allowed larger perimeters. As previously shown, the (CTM mast) Size-1 cross-section would collect near-OML current for $N_\infty < 5.7 \times 10^5$ cm^{-3}, covering almost the entire range of plasma densities of interest.

* Figure 3.4 for solar maximum and high altitudes makes the average in (11) about unity for a reference value $N_{\infty ref} = 2.6 \times 10^5$ cm^{-3}. Use of Size-1 mast values $p^* = 7.65$ cm and $L/2 = 125$ m, at $N_\infty = 2.6 \times 10^5$ cm^{-3}, $\Phi_a \approx V_S = 200$ V, and $I_a = 0.15\, I_{BT}$, then yields

$$I_{BT} \approx I_{OML} \approx 1.06 \text{ A} \rightarrow \quad \tilde{I} = I_{BT}\,(3/4 + I_a/I_{BT}) \approx 0.96 \text{ A}. \qquad (12)$$

At lower altitudes the current I_{OML} will be larger because densities are higher (Figs.3.8, 3.10, 3.12). At the lowest altitudes, however, I_{BT} will be less than the corresponding OML value both because the Debye length will be too small, and because ram effects are now important. Aerodynamic drag, here ignored, would come into play, however, at these altitudes; anyway, crossing the F-layer peak region, where N_∞ is largest, would take a short fraction of the full deorbiting time.

* Figure 3.15 presents results on deorbiting time from 1600 Km, obtained from a detailed numerical simulation for a S/C mass $M = 750$ kg, $p = 8$ cm, $L = 200$ m, $i = 90°$, $\Phi_a \approx V_S = 200$ V, and $I_a/I_{BT} = 0.15$. We integrated the linear momentum equation

in the geocentric inertial frame, including the J_2-term in the gravitational field, using the IGRF 85 geomagnetic field and IRI 95 models, and ignoring aerodynamic drag. Clearly, the short tether might only be effective during part of the solar cycle. For spacecraft with mission lifetime over 10 years, the tether might be effective if one would be allowed to advance or delay deorbiting by one or two years. For spacecraft with 1-2 years mission lifetime, the short tether could be useful, depending on the time of launch relative to the solar cycle. Figure 3.16 shows the solar activity cycle.

* *References*

[1] J.R.Sanmartín and R.D.Estes, Phys. Plasmas **6**, 395 (1999).

[2] R.D.Estes and J.R.Sanmartín, "New Results on Bare-Tether Current", to appear in Proc. Spacecraft Charging Technology Conf., Hanscom Air Force Base, MA, 2-6 Nov. 1998.

[3] J.G.Laframboise and L.W.Parker, Phys. Fluids **16**, 629 (1973).

[4] M.Martínez-Sánchez and J.R.Sanmartín, J. Geophys. Res. **102**, 27257 (1997).

[5] R.D.Estes, J.R.Sanmartín, and M.Martínez-Sánchez, "Technology of Bare Tether Current Collection", Proc.Tether Technology Interchange Meeting, NASA/CP-1998-206900, 379-398 (1998).

[6] R.D.Estes, E.C.Lorenzini, J.R.Sanmartín, J.Peláez, M.Martínez-Sánchez, L.Johnson, and I.Vas, "Bare Tethers for Electrodynamic Spacecraft Propulsion", J. Spacecr. Rockets, in press (1999).

[7] C. L. Staugaitis and R. E. Predmore, "Mechanical Properties of Advanced Gravity Gradient Booms", NASA TN D-5997, Washington, D.C. (1970).

[8] "Tubular Spacecraft Booms (Extendible, Reel Stored)", NASA SP-8065 (1971).

[9] M. Aguirre, R. Bureo, F. del Campo, and M. Fuentes, "The CTM Family of Masts & the CTM Engineering Model", unpublished.

[10] D. Bilitza, K. Rawer, L. Bossy and T. Gulyaeva, Adv. Space Res. **13**, (3)3 (1993).

[11] D. E. Hastings, J. Geophysical Research **100**, 14,457 (1995).

4 Selection of Contactors: Existent Technology

* The selection of a plasma contactor for current exchange between tether and ionosphere would be first dictated by the need to keep the weight of the consumed expellant (neutral gas) low. The weight of the contactor, its associated electronic box, and the neutral gas bottle is not critical. The long working time required from both plasma contactors will demand long term stowage of large amounts of neutral gas if not efficiently used. Basic additional constraints arise from the limited electric power available in the spacecraft, and the requested levels of tether current.

Hollow cathodes of the simplest (*open keeper*) type consist of a tube with a small hole (typically 1 mm) at one extreme. Expellant gas flowing along the tube is first slightly ionized by a chemically impregnated tantalum foil heated up to thermoionic emission. As this weakly ionized gas leaks through the small exit at the end, an electric discharge is established between the tube, acting as electrode, and a holed plate (the keeper) located a few millimeters downstream. The minimum mass flow rate required to sustain the hollow cathode electric discharge is typically a fraction of sccm (standard cubic centimeter by minute) of Xenon. The open keeper hollow cathode is only capable of ionizing about 1% of the neutral gas employed as expellant in all cases. The neutral pressure inside the hollow tube is high, about 1-20 Torr, whereas the background pressure in laboratory tests lies in the range 10^{-6}-10^{-8} Torr.

This low fractional ionization results in strong requirements on neutral gas stowage. Volume requirements were solved in early models used in space by having mercury as working fluid [1]. However, the presence of chemicals in the plasma contactor exhaust damaged the exposed spacecraft surfaces and led to replacing mercury by inert gases such as Xenon or Krypton. This led to new technical difficulties in

expellant stowage and degree of purity, gas flow monitoring, and control of the electric discharge, which have not been solved until recently.

* An increase in the efficiency of the hollow cathode discharge is obtained by enclosing the space beween keeper and hollow tube. This (*enclosed keeper*) geometry raises the efficiency of the discharge from 1% up to 5%. A third plasma contactor design uses hollow cathodes as both primary plasma source and electron emitter, reaching up to 80% ionization of expellant in a secondary discharge in the presence of an anisotropic magnetic field (*ring cusp* devices, derived from the well known Kauffmann plasma sources).

Power consumption by hollow cathodes depends on the operational mode. A peak startup power is needed to initiate the hollow cathode discharge by heating the insert. The power is decreased in the running mode, when insert heating is no longer required to sustain the electric discharge. The peak power would be again needed for restart in the event of failure.

* In Table I we present a list of space plasma contactors, mostly hollow cathodes, only including those specially designed for use onboard spacecraft under LEO conditions. There exists a long list of commercial devices, available for use as electron emitters or ion beam sources in plasma-aided manufacturing, which do not meet space requirements and will not be discused here.

The different devices presented in Table I are divided in three different groups according to their origin: Europe, US and Russia. Note that each model has been designed for a given set of operational conditions, which can differ from those holding in the context of the present study. For instance, a requisite for the Space Station is an effective electron emission between 0.1 and 10 Amps, the contactor being considered a

mission-critical system [2]. This requires electric power (53.8 W startup and 36.0 W running in steady state) much larger than the power for the STRV device [3], which is intended to control differential charging of small satellites.

* *Discussion of available contactors*

The hollow cathode labeled STRV (Space Technology Research Vehicle) [3] is a derivation of those employed on T5 ion thrusters (a component of the UK-10 ion propulsion system), scheduled to fly on the ESA Artemis communications satellite. The original device was developed by the Defence Research Agency (DRA) of UK; STRV-1a was launched on June 17, 1994 (Ariane flight 64). One of the experiments of this package consisted in a hollow cathode neutraliser designed to detect and eliminate differential surface charging near apogee. They used mercury as propellant, whereas new versions employ Xenon. Both electrical power consumption (less than 20 Watts) and Xenon mass flow rate (1.5-6.0 Kg/Yr) are low to moderate and match the requirements for our proposed mission. Flight qualification studies for this device are under way.

The next three hollow cathodes, labelled Ncc A/300, A/5000 and A/10000 are members of a family developed by Proel Technologies at Firenze (Italy) under ASI (Agenzia Spaziale Italiana) contract [4]. The model A/300 presents characteristics somewhat lower than STRV: low electric power (38 Watts for startup and 7 Watts running) and Xenon consumption (about 1.5 Kg/Yr). The two other models are supposed to yield larger electron emission currents (more than 1 Amp), exceeding the requirements of our proposed mission. In fact, an intermediate model between A/300 (designed for 300 mA) and A/5000 (5 Amp) would ideally fit the requisite conditions of this study. Flight qualification (vibration, thermal stresses, ...etc) studies for these

devices, for purposes of charge satellite control, are also under way with support from ESTEC [4].

The hollow cathodes labelled GPC-1 and GPC-2 are manufactured by the Department of Electric Propulsion and Applied Plasmadynamics of the *Research Institute of Machine Building*, and are also commercially available [6]. Performances are similar to those of European models previously described, using inert gases (Xenon, Krypton and Argon) with similar mass flow rates. Although the power consumption is not quoted in the information available, it should be similar too.

American models cited in Table I were all flown in space missions but present different drawbacks. The ATLAS plasma contactor [7]-[8], was flown on Shuttle STS-4 as part of the SEPAC (Space Experiment with Particle Accelerators) experiment [8]. ATLAS was a ring cusp device that would exceed our limits on neutral gas stowage and electric power (more than 250 watts). Similar arguments apply to the ongoing development of a hollow cathode for the future Space Station [2] (a enclosed keeper device with moderate requisites, but still larger than the above mentioned developments by Proel and DRA). This plasma contactor is derived from those already used in the PMG (Plasma Motor Generator) flight [9], which also exceed the performances of other models for our purposes. The hollow cathode employed in the PMG mission used batteries to operate for a period of four orbits. Data on power consumption are therefore not well defined, although they should be close to Proel Ncc A/5000 because of similar performances.

Similar considerations apply to the Russian model labelled PROGRESS, developed under a collaborative INTAS Grant in the context of an electrodynamic tether experiment [10]. This device was developed by Bauman University according to

Russian spacecraft standards. Russian models OKA and EPICURE, designed by the above mentioned Research Institute of Machine Building, follow similar trends. These pulsed plasma sources were used in different suborbital flights during the period 1973-74, with Cesium as propellant, and were also tested on board meteorological rockets as well as in some COSMOS flights [11]. Use of Cesium as expellant presents drawbacks similar to mercury (highly reactive chemicals at the plasma contactor exhaust) and high electric power (Kilowatt range).

* *Determination of plasma contactor performances*

Relevant points for assessment of contactors, in addition to low power and neutral gas consumption (and low mass and size), concern certain contactor capabilities:

1. The production and transport of charges of both signs at the requested level of tether current, while sustaining a low potential bias (low contact impedance).
2. Self switching from electron emission to electron collection, according to the relative bias between the ambient background plasma and the hollow cathode.
3. Both long lifetime and capability for multiple restarts in the event of failure or switching off.

Plasma contactor performances can be verified to some degree in ground tests, previous to qualification for flight. Information from previous NASA flights and other sources allow determining the nature and characteristics of laboratory tests to be conducted for a long term tether mission. A tentative experimental checking program (from Ref. [4]) would cover the following items:

- Thermal and mechanical stresses. Heating cycling tests.

- Activation and ignition tests.
- Internal hollow-cathode discharge characterization.
- Current-Voltage characteristic response.
- Lifetime and restarts tests.

* *Thermal and mechanical stresses*

A critical point concerns the mechanical resistance to vibrations and thermal stresses. Although a detailed study of these effects falls beyond the scope of the present study, it is worth mentioning some of them. The hollow-cathode body reaches high temperatures (between 500 and 1500 °C) at the start of the discharge, when heating the insert up to large electron thermoionic emission. These effects are well known and several plasma contactors have been subjected to computer simulations with thermal mathematical models. Measurements of cathode tip temperature with an optical pyrometer confirmed results from simulations carried out for the Ncc series of Proel with the ESATAN code (figures 6, 7 and 10 in Ref. [4]). Similar conclusions have been obtained for other devices [12]. Problems arising from the high temperatures produced in the activation process would be shared by all devices previously cited.

The mechanical interface must thus be carefully designed to account for any undesired state of thermal stresses, as well as vibrations and thermal expansions of the device. Also, because the hollow cathode is biased with respect to different elements of the interface (ambient plasma, tether, ...), the contactor mechanical interface must be electrically insulated by means of some ceramic insulator. A broad variety of tests related to all such effects, including heating cycling tests, have already been conducted for the Ncc family of devices, in particular for the low power Ncc A/300.

* *Ignition tests and internal discharge characterization*

As mentioned before, hollow cathodes require an activation sequence for establishing the electric discharge. Ignition tests are meaningless unless experimental details, such as the characteristics of the power supply used, are clearly defined. After ignition the hollow cathode discharge reaches equilibrium at a given current or power value. This depends on the type of power supply used in the tests (constant current or power) [4], and these details may affect mission design.

For the purposes of the present study, the hollow cathode characteristics can be completely determined in the ground, under laboratory conditions. However, the data available in the scientific literature for contactor discharges provide strong indications that important elementary physical and gasdynamical processes are still poorly understood. Hollow cathodes represent today an active field of research and care must be taken in extrapolating predictions from simplified theoretical models to actual ionospheric conditions.

* *Current-Voltage characteristic response*

The electron and ion emission features can be well characterized with suitable laboratory tests, although procedures for flight qualification are still lacking. The two methods currently used to measure the emitted current (electrons or ions) require biasing the plasma contactor with respect to either an ambient background plasma or some flat metallic plate[1]. Emitted and/or collected currents are monitored at different bias voltages for fixed hollow cathode discharge conditions. There are, however, uncertainties involved in the procedure.

First, the actual ionospheric conditions can not be fully reproduced in laboratory simulations; this represents an unavoidable drawback in determining plasma contactor

[1]An schematic of this last experimental set up may be found in Figs. 2 and 3 of reference 5.

performances. The current collection process from an ambient plasma strongly depends on the ion and electron temperatures and density. Laboratory plasmas usually have electron temperatures more than one order of magnitude above ionospheric values, and charged particle densities up to two orders of magnitude larger. In fact, few plasma facilities (a case being the JONAS plasma chamber at ONERA, in Toulouse, France) are designed to simulate the low ionospheric densities and temperatures, using a special kind of plasma generator.

Secondly, in many hollow cathode tests, polarization voltages are not always clearly referenced to either a common ground or the ambient background plasma (see figures 13 and 14 in Ref. [4]), which often lies several volts over the plasma chamber walls (usually grounded). This may lead to an overestimation of bias voltages needed for large electron emission (or collection), depending on the particular experimental set up employed. This constitutes a key point because the bias voltage with respect to the ambient ionospheric plasma determines the switching from electron to ion emission modes in actual space situations.

* *Lifetime and capability for multiple restarts*

This point is also important here. First, if we could fully rest on a bare tether for anodic collection, it might be possible to reduce the consumption of Xenon expellant by keeping the contactor at the anodic tether end in idle mode (just discharge current) for every half orbit. Actually, it might even pay to fully switch off the contactor. The electrical energy for the starting sequence, with the low-work insert activated by heating into large thermoionic emission, is typically small (about 38 Watts over 120 seconds for the smaller contactor in the Ncc series) when compared with the energy requisites for quiet running along one orbit (about 7 Watts for 2 hours); the consumed electrical

energy could be cut in half.

In the case of our deorbiting tether, with about 12 orbits per day, more than 4000 restarts should take place over one year. Long term tests of very large numbers of restarts have been conducted for several models in Table I, more than 100,000 for the Ncc A/300. This has a start time of less than 120 seconds (a time similar for all models of the series), ion emission currents below 0.5 mA, and electron emission currents up to 1 A. An on-off switching sequence for both hollow cathodes, programmed along the orbit, might permit to optimize electrical power consumption, and the amount of neutral gas stored on board.

* To conclude, the most promising choice for a plasma contactor would be a low power, enclosed keeper, hollow cathode. In fact, as already mentioned, a Proel model in the NccA series intermediate between A/300 (designed for 300 mA) and A/5000 (5 Amp) would ideally fit the requisite conditions of this study. The SRTV contactor might also be close to optimal. As an example, for an estimated mass flow rate of 4 Kg/year (about 1,5 Sccm), each contactor would require 3 Kg for a total mission duration of 1 1/2 years, if anodic collection would entirely rest on the bare tether. This would require a 2 liters gas bottle for Xenon at supercritical conditions (density $\approx 1.5\times10^3$ kg/m^3), on each contactor. From the Table we could estimate a running power around 20 watts. Voltage-current characteristics from ground simulations suggest that 1A electron-emission currents can be reached at 30 V bias voltages [2-4] [10], [12, 13], making the cathodic impedance small compared with the impedance of our bare tether.

* *References.*

[1] W.R. Kerslake and L.R. Ignaczak, *Journal of Spacecraft and Rockets* **30**, (3), 258-290, (1993).

[2] M.J. Patterson, J.A. Hamley, C.J. Sarmiento, D.H. Manzella, T. Sarver-Verhey, G.C. Soulas and A. Nelson. Plasma contactor development for the space station., *NASA Technical Memorandum 106425, IEPC-93-266,* (1993).

[3] T.M. Jack. The characterization of the STRV small satellite charge alleviation cathode.Communication to the *III International Workshop on Transient Hollow Cathode Discharge Phenomena.* Univ. Pierre et Marie Curie, Paris, France, (1994).

[4] M. Minucci, A. Severi, M. Capacci, C. Bonifaci and F. Svelto. Plasma contactor device family for space use working up to 10 A: Review of the funcional testing activity. *Proceedings of the Fourth International Conference of Tethers in Space.* Vol: 2, pp. 873-880, Smithsonian Institute, Washignton DC, (April 1995).

[5] G. Saccoccia and A. Matucci, Plasma contactor technology for space charge neutralisation *Preparing for the future: ESA's Technology Programme Quartely*, **4**, (3), (September 1994).

[6] Department of Electric Propulsion and Applied Plasmadynamics. Research Institute of Machine Building }, 4, Pionerskaya, Kaliningrad, Moscow region, Russia.

[7] I. Katz, T. Neubert, W.T. Roberts, W.W. Taylor and J.R. Beattie. *Journal of Spacecraft and Rockets.* **31**, (6), 1079-1084, (1994).

[8] J.R. Beatie, J.N. Matossian, J.L. Burch and W.C. Wilson. System performance of ATLAS plasma contactor}. *IAAA paper* 90-2568, (1990).

[9] D. Chlouber, R.J. Jost and T.L. Wilson. Correlation of tether current with day/night cycles during PMG mission. *Proceedings of the Fourth International Conference of Tethers in Space.* Vol: 3, pp. 1857-1871, Smithsonian Institute, Washington DC, (April 1995). D. Chloubert, R.J. Jost, J.E. McCoy and T.L. Wilson.

Plasma motor generator (PMG) mission report}, *NASA, JSC-26714*, (August 1994).

[10] J.R. Sanmartin, L. Conde, G. Tacconi, N.A. Savich and Y. Protasov. Anodeless electrodynamic tether for propulsion and scientific applications. *Final Report, INTAS 94-3853*, (June 1996).

[11] This information, appearing in the commercial brochure of the firm, has been confirmed by personal communication. No data on these flights is available from authors.

[12] J.E. McCoy *et al.* Plasma motor generator (PMG) flight experiment results *Proceedings of the Fourth International Conference of Tethers in Space.* Vol: 1, pp. 57-82, Smithsonian Institute, Washignton DC, (April 1995).

[13] L. Iess *et al.* Satellite deorbiting by means of electrodynamic tethers: General concepts and requirements. Communication to the 49th International Astronautical Congress: IAF-98-S.05. Melbourne, Australia, (September. 1998).

5 Selection of Contactors : Theoretical Modeling

* *Electron emission (cathodic contactor)*

Electron emitters based on hollow-cathode (HC) devices are used satisfactorily as neutralizers of ion beams in ion thrusters. Electron emissions of several tens of amps have been reported [1]. An ion thruster consists of a HC inside a discharge chamber where the ion beam is produced, and an external HC emitting an electron cloud that neutralizes both electric charge and current in the ejected ion beam. A plasma contactor differs substantially from ion thrusters; the HC device emits an electron beam, its negative charge (but not the electron current) being neutralized by ions provided by either the HC itself or by a positively biased ambient plasma.

The space experience on HC electron emission is scarce and only covers low currents. The SERT-II [2] and ATS-series [3] experiments on potential control proved that low plasma emissions can modify the spacecraft potential by tens of volts. The PMG experiment, involving a complete tether system, suggested that the cathodic contactor made a small contribution to the system impedance; the maximum emitted current was 0.3 A [4]. In support of space experiments, ground tests with cathodic contactors [5,6] have showed good current-voltage (C-V) characteristics under a broad range of operational conditions. Experimental conditions in vacuum chambers are, however, quite different from those found in space. At the critical plasma densities of interest in the ionosphere, the emitted plasma cloud should reach distances far greater than the size of laboratory plasma chambers. Proper ground simulation of space conditions would then require to scale accordingly all characteristic lengths (Debye length, Larmor radius, square root of contactor area, ionization mean free path, ...), which is impossible in practice; in fact, it is not clear in general, PMG being an

example, how actual contactor areas (A_{ct}) compared with each other in space and laboratory. Two other dimensionless numbers hard to reproduce on the ground are temperature ratio T_i/T_e (about unity in space and very small in the ground), and plasma motion past the contactor (ion Mach number ~ $\sqrt{30}$ in space). Nevertheless, ground experiments are useful in understanding plasma response, and building up theoretical or semi-empirical models.

In spite of difficulties in reproducing actual space conditions, there is a general confidence that emission of large electron currents into the rarefied ionosphere is not problematic, as proved by the selection of a HC-device capable of emitting 10A to control the floating potential of the International Space Station (ISS) [6]. The large series of ground tests comparing enclosed-keeper (EK) and ring-cusp (RC) designs for the ISS cathodic contactor also proved that the EK design holds a clear advantage in terms of development cost, power consumption, simplicity, and robustness of design. The only penalty is a slightly larger mass consumption; a ring-cusp contactor provides a much larger ion production rate, a feature not clearly necessary, however, in sustaining high electron emissions.

* A simplified scheme of an enclosed-keeper HC operating as cathodic contactor is given in Fig.1a, which shows three plasma regions and both keeper and overall electrical circuits. It has been established experimentally that each HC geometry (tube and orifice diameters, particularly), requires minimum discharge current I_d and mass flow rate $\dot{m}$ for steady operation (with HC heater switched off). Thus, the keeper circuit is designed to operate with keeper current I_K somewhat larger than the minimum I_d, the HC being connected to tether and satellite at some point C to avoid undesirable limitations on emitted current (Fig.1a). The total discharge current is sum of

tether and keeper currents, $I_d = I_c + I_K$. For I_c and I_d given, HC and keeper voltages, Φ_c and V_K, self-adjust through the interaction of electric field and the various plasma species, the C-V response of the contactor verifying a formal relation,

$$\Phi_c = \Phi_c(I_c,\ I_K,\ \dot{m},\ \text{geometry, ambient conditions}).$$

* The influence of the mass flow rate on the current-voltage response is seen in Fig.1b, depicting the operational modes experimentally identified [5-7]:

(i) A plume mode at low $\dot{m}$, with an almost horizontal characteristic $I_c=I_c(\Phi_c)$, large fluctuations in keeper voltage, a luminous bluish plume extending several centimeters from the keeper and arising from neutral gas excitation, and an occasional potential hill attributed to external ionization.

(ii) A spot mode at large enough $\dot{m}$, with a current characteristic near vertical until maximum emission is attained. This mode presents higher electron densities and temperatures, more efficient internal ionization, and no fluctuations. The external potential profile shows neither hills nor sharp steps. Higher discharge currents and shorter HC to keeper distances favor this efficient operational mode.

(iii) A mixed mode at intermediate values of $\dot{m}$, with transition from plume to spot behavior at certain current level.

* The determination of contactor characteristics requires understanding complex physical processes in all three plasma regions. The internal HC region has been extensively studied both experimentally and theoretically [8]; although there is yet no conclusive physical model, empirical know-how suffices to build efficient hollow cathodes. Plasma profiles in the external region have been measured too; Fig.1c shows the electrostatic potential profile in the spot mode. Several theories have addressed the

keeper and external regions but none is fully consistent, or able to predict the different operational modes [9]. One thus relies, in part, on values given by experimentalists and manufacturers, although $\dot{m}_c(I_c)$ and $\Phi_c(I_c)$ laws, even if crude, are needed to evaluate the performance of tether systems.

* A tentative law for expellant flow rate was given in Ref.10,

$$\frac{\dot{m}_c}{I_c} \approx \frac{m_i}{e\eta_u}\frac{v_s}{\bar{c}_e} \rightarrow \frac{m_i}{e\eta_c}\sqrt{\frac{m_e}{m_i}}\,, \qquad (1)$$

where η_u is the effective fractional ionization (utilization efficiency) of the gas, v_S is the ambipolar sound speed and $\bar{c}_e \equiv \sqrt{kT_e / 2\pi m_e}$; we took $T_i << T_e$ in the expelled plasma and wrote $\eta_c \equiv \eta_u/\sqrt{10\pi/3}$. Comparing Eq.(1) to values $\dot{m}_c/I_c = 5.1$ and 2.1 kg/year×A for Proel Ncc A/300 and A/5000 (Xenon) contactors, one finds $\eta_c = 0.017$ and 0.042, respectively. This would give η_u = 5.5 % and 13.6 %, indicating an efficiency increase with current. level. The factor $\sqrt{10\pi/3}$, however, is only an estimate; also, there is no accurate method to measure η_u for electron emission. We propose using (1) with η_c estimated from experimental tests on the selected contactor.

Concerning $\Phi_c(I_c)$, experiments show the voltage Φ_c covering a limited range in the spot mode. For zero emission ($I_c \cong 0$), one has $V_K \cong 0$ and $|\Phi_c|$ ~ Ionization potential (17V in Ref.11, and 10V in Ref.6). As current emission increases, $|\Phi_c|$ increases slightly (to 30V for 1A [11], and just 12-14 V for 10A [6]), while cathode-to-keeper bias decreases monotonically (~ 12 and 8-10 V in Refs.11 and 6, respectively). These moderate potentials justify approximating the cathodic C-V characteristic, for I_c below maximum, as

$$\Phi_c(I_c) \cong const\,. \qquad (2)$$

* The extension of laboratory results to ionosphere conditions has rarely been considered in the literature. Even for the ISS plasma contactor, a critical subsystem with an emission requirement of 10 A, we could find discussions of neither that subject nor chamber pressure effects on the C-V response. The emitted electron beam has to be neutralized by ions provided by the contactor and the background plasma. Due to larger background density and limited chamber size, density profiles are much smoother in laboratory than in space; for instance, for 1A electron beam, the decrement of ion density is 5 to 6 orders of magnitude in space, and 1 to 3 orders in a vacuum chamber. Therefore, one might expect larger potential drops, disturbance regions, and magnetic effects in space. With the contactor moving through the ionosphere, and no wall confinement, gas consumption might possibly be larger too.

* *Electron (anodic) collection*

The PMG [4] and SEPAC [12] missions carried out flight tests of current collection by anodic contactors. The PMG experiment used two identical open-keeper contactors connected via a 500m conducting tether in elliptical orbit, with ionospheric plasma density N_∞ ranging from $5 \times 10^{10}\,m^{-3}$ to $10^{12}\,m^{-3}$. A battery on board could move the upper-lower contactor bias by an amount ranging from + 65 V to -130 V; each contactor operated in the cathodic or anodic mode depending on full bias. Although overall current data provided limited information about the C-V characteristic of each contactor, some measurements suggested good cathodic contact, while current-closure analyses predict a small radiation impedance (Sec.6); It can thus be assumed that the anodic impedance was dominant, the overall current response reflecting the anode characteristic $I_a(\Phi_a)$.

The basic result was that the anode could not accommodate plasma density changes along orbit (as in passive contact). As Table 1 later illustrates, current collection was moderately good at high densities (dayside, F-layer altitudes), with currents of about 200-300 mA, full plasma impedance (anodic and cathodic contacts + radiation) of about 100 Ω, and an effective collection area, $A_{eff} = I_a/J_{th}$ (random current density) ~ 15-25 m^2, about 100 times larger than the actual contactor area. At low densities, however, current just dropped with N_∞ with similar A_{eff} (~ 20-30m^2). A limited plasma production and, more probably, magnetic channeling of electrons seem to be the factors limiting A_{eff}.

* The very low expellant utilization (<1%) of the PMG open-keeper design might be partially responsible for the poor performance too. Ground and space experiments with enclosed-keeper contactors in the electron collection mode are lacking. The ATLAS1/SEPAC experiment, flown in the STS45 orbiter, used a ring-cusp device to limit S/C charging caused by an electron-gun emitted beam. Ground tests [13] registered (internal) ion production rates of up to 2A (compared with 25 mA for PMG), corresponding to utilization efficiencies above 75%. Flying on a 300 Km orbit at different orientations, the current at the anodic contactor reached 650 mA (the Orbiter conducting surfaces collected an additional 200 mA electron current); how SEPAC current was shared between emitted ions and collected electrons is unclear. The collected current yields a value A_{eff} ~100-300 m^2, which exceeds PMG by a factor 3-10. Actually, the SEPAC current might have been limited by the emission capability of the electron gun at the other end of the circuit. Although ring-cusp contactors are a potential solution for large anode currents, present operational uncertainties and the large gas consumption required make them unsuitable for long-time missions.

Currents up to 2A have been collected in ground experiments [11,14] with open- and enclosed-keeper designs but, again, laboratory parameters did not reproduce space conditions. A correct simulation is particularly necessary for anodic contactors, their C-V response being more dependent on the ambient plasma.

* Figure 5.2a shows the electric circuit of an anodic contactor, with tether connected to the keeper to minimize the contact impedance. Thus, a contactor operating alternatively as anode and cathode must allow for electrical switching. Figure 5.2b sketches high and low impedance modes of operation found in experiments, and related to gas emission rate and utilization. Figure 5.2c sketches external profiles of the electrostatic potential for the two operational modes. The main feature of the low-impedance mode is that the classical space-charge layer, where most of the potential drop takes place, lies away from the contactor and confines a quasineutral plasma cloud (the core); this intermediate layer is known as a double-layer (DL). The different potential profiles for cathodic and anodic contactors, indicate that there is no symmetry between the plasma processes for electron collection and emission.

* A spherical model for collisionless, unmagnetized, monoenergetic electrons, due to Ahedo et al. [15] explains the different operational modes of anodic contactors and computes the anodic current in terms of the emitted ion current I_i and the contactor bias, $I_a = I_a(I_i, \Phi_a)$. Operation in the low-impedance (core/DL) mode corresponds to an emission current above some 'space-charge-limit' value:

$$I_i > I_{SCL} \sim A_{ct} \sqrt{(T_e/m_i)},$$

where A_{ct} is the collecting area of the contactor. The C-V response is determined by the Langmuir law for double layers,

$$I_e (I_i, \Phi_a) = \mu_L(\Phi_a) I_i \sqrt{(m_i/m_e)}, \qquad I_a = I_i + I_e \approx I_e, \qquad (3a,3b)$$

with $\mu_L(\Phi_a) \sim 0.5$-1, typically. The DL acts as effective collection surface, satisfying

$$I_e \approx 1.5 \times 4\pi r_{DL}^2 J_{th}, \qquad (4)$$

with $J_{th} = eN_\infty \sqrt{kT_e / 2\pi m_e}$ [15].

* Equation (3a) is valid for conditions well outside the OML regime for spherical or sphere-like geometry. At large $e\Phi_a/kT_e$, the OML current is

$$I_a \approx I_e = I_{OML}(\Phi_a) \approx J_{th} A_{ct} \frac{e\Phi_a}{kT_e}. \qquad (5)$$

Electron currents larger than I_{OML} have been claimed in laboratory experiments, but it is unclear whether this was due to collisional effects. The OML current will be taken here as a conservative limit. The C-V response has three (no-core, core/DL, and OML) branches [15]. The anode current characteristic, $I_a = I_a(I_i, \Phi_a)$, depends mainly on I_i for the low-impedance (core/DL) branch, and on Φ_a for the other two branches. For given Φ_a, the optimum point in the C-V characteristic lies at the transition to the OML regime, corresponding to an emission current

$$I_i = I_{i,opt} = \frac{A_{ct}}{\mu_L} eN_\infty \frac{e\Phi_a}{\sqrt{2\pi\, m_i kT_e}}.$$

For typical mission conditions

$$J_{th} = 3 \text{ mA/m}^2 \ (N_\infty = 2.5 \times 10^{11} m^{-3}, T_e = 0.2 \text{ eV}), \quad \Phi_a = 200\text{V}, \qquad (6)$$

and $A_{ct} = 0.3$ m^2 the OML current is 0.9A and this is reached with a Xenon ion current of $I_{i,opt} \sim 3$mA, only.

* Ahedo [16] generalized the model of Ref.15 to include external ionization of the expelled gas by electron impact, which is important in most ground experiments with an intermediate DL. It was found that laws (3)-(4) are still valid, I_i now being the ion current reaching the DL. When external ionization is dominant, the core size, r_{co},

self-adjusts to produce the ion current required by the Langmuir law, Eq.(3a). If λ_{ion} is the mean free path for ionization, one has

$$\frac{r_{co}}{\lambda_{ion}} \sim \sqrt{\frac{m_e}{m_i}} << 1,$$

only a small fraction of the electron beam being thus affected by ionizing collisions. Since λ_{ion} depends on both Φ_a and gas density, the collected current can decrease when the gas density is increased, and the dependence of I_a on Φ_a is stronger for external ionization than for internal one. Anyhow, external ionization should be inefficient under space conditions because the density of emitted neutrals decays fast away from the contactor.

* Gas consumption rate $\dot{m}_a$ and emitted ion current I_i keep the identity

$$\dot{m}_a = \frac{m_i I_i}{e\eta_u}, \qquad (7)$$

with the fractional ionization η_u around 1% and 5% for open and enclosed keepers, respectively. From Eqs. (3) and (7) one obtains a relation similar to that holding for cathodic contactors [Eq. (1)],

$$\frac{\dot{m}_a}{I_a} \sim \frac{m_i}{\eta_a e}\sqrt{\frac{m_e}{m_i}}, \qquad \eta_a = \eta_u \mu_L . \qquad (8)$$

For a typical (enclosed-keeper) figure of η_a=0.03 and Xenon, one has $\dot{m}_a/I_a$ = 2.9 kg/year. Therefore, the core/DL mode of operation requires low mass consumption (even when η_u is low), making unnecessary the use of complex ring-cusp contactors (with η_u about 80%).

* In a magnetized plasma electron flow tends to be channeled along field lines, and electron collection becomes anisotropic. There is yet no consistent theory of current collection in magnetized plasmas. For a discussion of the different theories see

Laframboise and Sonmor [17]; most of the works cited below are discussed in this review. A frequently invoked theory is that of Parker and Murphy, developed for a cold ($e\Phi_a/kT_e >> 1$), collisionless plasma. It gives an upper-bound, I_{PM}, to current collected by a sphere-like object of radius R_{cl},

$$I_{PM} = 2A_{PM}J_{th}, \qquad A_{PM} = \pi R_{cl}(R_{cl} + 2r_M), \qquad r_M = l_e\sqrt{2e\Phi_a / kT_e}, \qquad (9)$$

where A_{PM} is the cross-section area of the magnetic tube that collects electrons, $l_e = (kT_e m_e)^{1/2}/eB$ is a thermal Larmor radius ($l_e \sim 3.5$ cm), and r_M is the Larmor radius at energy $e\Phi_a$. The validity of this theory for space conditions is under revision: PMG currents are up to 12 times larger than the Parker-Murphy upper-bound, and TSS-1 and TSS-1R [18] currents (collected with a passive sphere) were 2-3 times larger than that limit. Different effects that favor plasma transport perpendicular to the magnetic field have been proposed to explain the enhancement of current.

* A persistent suggestion has been that plasma turbulence induced by current instabilities might result in large, anomalous collisional scattering of electrons, breaking down magnetic channeling (and dominant orbital motions) [19]. Ground experiments (in an unmagnetized plasma) show low-to-moderate fluctuation levels in the plasma response, and occasional thermalization of the electron beam, both possibly originated by current-driven instabilities. However, there is no direct evidence that turbulence shields out magnetic guiding and enhances substantially current collection. A second suggestion, by Thompson, is that, for a moving spacecraft, plasma drift across the lateral walls of the magnetic tube of Parker-Murphy could enhance the current. Several authors [19, 20] have proposed a modified Parker-Murphy formula

$$I_e \approx I_{MPM} = 2\mu_{PM}A_{PM}J_{th}. \qquad (10)$$

Experimental data yields $\mu_{PM} \sim$ 2-3 for TSS-1R; for PMG (see table 1) one has $\mu_{PM} \sim$ 6-12 when only the contactor was collecting electrons, and $\mu_{PM} \sim$ 2-3 when the metallic structure of the rocket did collect a significant fraction. However, even Eq. (10) is disputed for TSS-1R: Vannaronni et al. [19] have shown that the C-V response of TSS-1R fits much better the scaling law of Langmuir-Blodgett theory for unmagnetized plasmas than the modified Parker-Murphy formula; besides, in-situ measurements detected no electron guiding inside the sheath. A recent analysis [21] gives theoretical support to a weakly-magnetized, thick sheath around TSS-1R.

* Analysis of PMG and TSS-1R results indicates that a plasma-emitting contactor has a certain capability to diminish magnetic guiding effects. The large experimental value of μ_{PM} for PMG suggests that Eq. (10) is not very appropriate for plasma-emitting contactors. We propose here a crude model on how a core/DL plasma structure could enhance the collection of current. Since the core potential is close to the contactor potential, electrons come into the core with energy $\sim e\Phi_a$. Due to the large potential jump at the DL and the magnetized trajectory of electrons, collisions, although infrequent, will probably trap electrons within the core and they will be collected eventually by the contactor. Accepting this scenario, plasma conservation laws indicate the core size r_{co} is self-adjusted to about r_M. Parker-Murphy theory is then applied with the core external surface as 'virtual anode'; substituting R_{ct} by $R_{ct} + r_M$ in (9) and introducing a factor μ_M to take into account additional transverse transport (by satellite motion, for instance) one has

$$I_e \approx I_M = 2\mu_M A_M J_{th}, \qquad A_M \equiv \pi(R_{ct} + r_M)\,(R_{ct} + 3r_M). \tag{11}$$

Table 1 compares PMG results with Parker-Murphy law (9) and with Eq. (11). Although the available data is scarce, the crude model proposed here yields a much better

agreement, with μ_M ~1-1.7. It will be accepted here, at least as the extrapolation algorithm of PMG results for estimates of anodic current in our mission conditions.

J_{th}(mA/m^2)	12	12	12	12	0.5	0.5	0.5	0.5
$\Phi_a+\|\Phi_c\|$(V)	-40	-9	16	59	-79	-15	53	112
I(mA)	-300(*)	-130(*)	70	180	-4 ?	-1 ?	13	15
r_M(cm)	71	34	45	86	100	43	81	118
μ_{PM}	3.3(*)	2.2(*)	7	10			7.6	6.3
μ_M	1.11(*)	1.13(*)	1.23	1.04			1.67	1.01

Table 1: PMG results at maximum and minimum thermal current. Minus and plus signs in $\Phi_a+|\Phi_c|$ and I correspond to the two directions of the current along the tether; $\Phi_a+|\Phi_c|$ is estimated neglecting radiation losses; r_M is calculated taking $\Phi_a+|\Phi_c| \approx \Phi_a$; A_{ct}=0.3m^2 except in (*) where A_{ct}=4.5m^2 due to electron collection by the Delta II metallic structure.

For $r_M >> R_{ct}$, Eq.(11) yields $A_M \approx 3\pi r_M^2$ whereas $A_{PM} \approx \pi R r_M$, that is for large $e\Phi_a/kT_e$ one has

$$I_M = \mu_M 12\pi l_e^2 \frac{e\Phi_a}{kT_e} J_{th}, \qquad (12)$$

instead of the Parker-Murphy scaling law $I_{PM} \propto \sqrt{\Phi_a}$. Equation (12), having the Φ_a-dependence of the OML law (5), also determines a maximum collected current. The relation

$$I_M / I_{OML} \approx 3\mu_M l_e^2 / R_{ct}^2, \qquad (13)$$

shows the magnetic channeling limit as the lowest upper-bound for $l_e < R_{ct}\sqrt{3\mu_M}$, which is the case of ionospheric applications. Since Eq.(12) is based in the core/DL model, we assume that the minimum ion current needed to collect $I_e = I_M$ is given by the

Langmuir law (3a); then, Eq. (8) is still valid for $\dot{m}_a(I_a)$. The ratio between the current collected by the anodic contactor and the bare tether is

$$\frac{I_M}{I_{BT}} \approx \mu_M 12\pi^{3/2} \frac{l_e^2}{pL}\sqrt{\frac{e\Phi_a}{kT_e}}. \qquad (14)$$

For Eq. (12) --but not for Parker-Murphy law (10)--, large anode potentials favor collection by the contactor. For mission conditions (6), Eq. (12), with μ_M~1-1.7, yields I_e ~ 160-260mA, and Eq.(10), with μ_{PM} ~6-12, yields I_e ~ 60-120mA. These two estimates indicate that the anodic contactor will be unable by itself to collect the level of current required by the mission, so the presence of a large bare boom is essential. The marginal role attributed to the anodic contactor suggests also that contactor selection be made on the basis of cathodic performances.

* *References*

[1] V.J. Friedly and P.J. Wilbur, J. Propulsion and Power **8**, 635 (1992).

[2] W.R.Kerslake and L.R.Ignaczac, J. Spacecraft **30**, 258 (1993).

[3] R.Olsen, J. Spacecraft **18**, 462 (1981).

[4] J.E.McCoy et al, in Proc. Fourth Int. Conf. on Tethers in Space, 57-82 (1995).

[5] J.D. Williams and P.J. Wilbur, J. Spacecraft **29**, 820 (1992).

[6] M.J.Patterson et al, IEPC-93-246 (1993), and Paper AIAA-94-3308 (1994).

[7] G.A.Csiky, NASA TN D-4966 (1969); J.D. Williams and P.J. Wilbur, J. Spacecraft **29**, 820 (1992); M.Monterde, A.Dangor, M.Haines, A.Malik, and D.Fearn, Paper AIAA-95-2383 (1995).

[8] M. Krishnan, R.Jahn, W. von Jaskowsky, and K.Clark, AIAA J. **15**, 1217 (1977); D.Siegfried and P.Wilbur, Progress Astro. Aeron.**79**, 262 (1981), and AIAA J. **22**, 1405

(1984); A.Salhi and P.Turchi, Papers AIAA-92-3742 (1992), and AIAA-94-3133 (1994).

[9] V.Davis, I.Katz, M.Mandell, and D.Parks, J. Spacecraft **25**, 175 (1988); D.Parks, I.Katz, B.Bucholz, and P.Wilbur, J. Appl.Phys. **74**, 7094 (1993); M.Mandell and I.Katz, Paper AIAA-94-3134 (1994).

[10] M. Martínez-Sánchez and D. E. Hastings, J. Astro. Sci. **35**, 75 (1987).

[11] J.D. Williams and P.J. Wilbur, J. Spacecraft **27,** 634 (1990).

[12] I.Katz, T.Neubert, W.T.Roberts, W.W.L.Taylor, and J.R.Beattie, J.Spacecraft **31**, 1079 (1994).

[13] J.R.Beattie, J.N.Matossian, J.L.Burch, and W.C.Gibson, Paper AIAA-90-2568 (1990).

[14] L. Conde and L. León, Phys. Plasmas **1,** 2441 (1994); G. Vannaroni, M. Dobrowolny, E. Melchioni, F. de Venuto, and R. Giovi, J. Appl. Phys. **71**, 4709 (1992).

[15] E. Ahedo, J.R. Sanmartín, and M. Martínez-Sánchez, Phys. Fluids B **4**, 3847 (1992).

[16] E. Ahedo, Phys. Plasmas **3**, 3875 (1996).

[17] J.G. Laframboise and L.J. Sonmor, J. Geophys. Res. **98**, 337 (1993).

[18] D.E. Hastings, J. Geophys. Res. **92**, 7716 (1987); D.E. Parks and I. Katz, J. Spacecraft **24**, 245 (1987).

[19] M. Dobrowolny et al., J. Geophys. Res. **100,** 953 (1995); G. Vannaroni et al., Geophys. Res. Let. **25**, 749 (1998).

[20] J.G. Laframboise, J. Geophys. Res. **102**, 2417 (1997).

[21] E. Ahedo, submitted to Phys. Plasmas.

6 Current Closure

* Current exchanged between tether and ionospheric plasma makes its way through the ionosphere to close a circuit. This current closure determines an impedance affecting the overall electric circuit. Also, if closure occurs near the tether it might modify the way contactors collect current, and thus contactor impedance. This might be particularly critical for the short tethers here contemplated.

* Note first that, for a tether lying near parallel to the local geomagnetic field, electrons could find an easy direct path along field lines, connecting the cathodic and anodic regions near the tether. This extreme near-field closure could affect both ionospheric and contact impedances. Our tether, however, being at right angle to the orbital plane, is near normal to the magnetic lines for the high-inclination orbits of interest. (The same applies to the usual vertical tethers in the case of low inclinations.)

* Two ways of far-field circuit closure in the plasma traversed by a F-layer tether have been suggested. The motion of moon Io through Jupiter's diluted magnetosphere is somewhat similar to the case of a tether. As in early analyses of Io's case [1], part of the TSS1 community assumed DC-like closure in the E-layer, through transverse (Pedersen) conductivity ("unipolar inductor" model). The argument, however, has been finally settled in favor of an earlier, alternative possibility [2, 3]: closure through current carried in Alfven (and Lower Hybrid) waves radiated to "infinity"; see Ref. [4] for Alfven Wave structure.

For the Alfven waves radiated by tethers in the F-layer, where

$$m_i/m_e \approx 30{,}000 >> v_A^2/v_{sat}^2 \sim 1{,}500\,,$$

one has

$$\varepsilon_1(\omega)/n^2 \sim v_{sat}^2/v_A^2,$$

$$\varepsilon_2(\omega) \sim \varepsilon_1(\omega) << n^2 \equiv c^2k^2/\omega^2 << \varepsilon_3(\omega).$$

Here, v_A is the Alfven velocity, and ε_1 and ε_3 (ε_2) are the usual diagonal (off-diagonal) components of a cold-plasma dielectric tensor. Far-field closure follows from a simple relation between Alfven current-density components parallel and perpendicular to the magnetic field,

$$j_{par}/j_{\perp} \sim \sqrt{\varepsilon_1 / n^2} \sim v_{sat}/v_A \sim 7\ kms^{-1} / 260\ kms^{-1} \sim 1/40.$$

For tethers 10 km long (but not for our short tethers), current closure might thus reach, in principle, into the E-layer. DC closure, however, assumes current makes closed loops, this requiring an impossibly fast current-loop round trip, given the extremely short times thin tethers take to fully cross a magnetic field line. (Io's case, because of its giant size and uncertainties in Alfven velocity, is not yet fully settled [5-7]). Both Alfven and Lower Hybrid impedances are negligible. Alfven impedance is typically about $10\ v_A/c^2$ $\sim 0.3\ \Omega$. The Lower Hybrid impedance varies as $m_i^{1/2}/I$, being about $0.4\ \Omega$ for oxygen and 1 A current [3, 8].

* Tether wave radiation at the topside and plasmaspheric regions does present a novelty over the F-layer case. As already noticed, the Alfven impedance at F-altitudes is determined by the large value of the parameter $m_i v_{sat}^2/ m_e v_A^2$. At the altitudes now of interest, however, hydrogen, rather than oxygen, is the dominant ion species, m_i being thus reduced by one order of magnitude. Further, v_A^2 is inversely proportional to both m_i and density N_∞ which is sensibly reduced itself. The bottom line is that now $m_i v_{sat}^2/ m_e v_A^2$ is small. The result is that Alfven (but not Lower Hybrid) radiation differs from that occurring in the F-layer. Preliminary results still suggest both far-field closure and Alfven impedance negligible for the overall electric circuit, although the impedance is one order of magnitude larger than in the F-layer case.

* Concerning near-field closure, numerical simulations allowing for nonlinear effects, but limited to frequencies well below the ion gyrofrequency (MHD models), have given some evidence of partial (25% and over) closure for moderately short (~140 m) tethers [9, 10]. We note, however, that standard numerical difficulties precluded the carrying out of simulations at the proper thermal-to-magnetic pressure ratio (β), which is less than 10^{-4} in the F-layer, and even smaller in the topside and plasmaspheric ionosphere. Values $\beta = 0.1$ and over were actually used in the calculations. This *introduces the Slow Magnetosonic mode and important false effects from thermal* pressure gradients. For such unrealistically hot, high-β plasmas, the ion thermal speed would replace v_{sat}; with

$$j_{par}/j_{\perp} \sim (\textit{ion thermal speed})/v_A \sim \sqrt{\beta} \geq 0.3$$

partial near-field closure would indeed follow, as found in the calculations.

* A different claim for near-field closure has been put forward. Laboratory experiments suggested that tethers radiate whistler, rather than Alfven, waves [11, 12]. It was then proposed, on the basis of numerical simulations, that whistler waves lead to tether near-field closure [13]. We note that, for whistler waves, one does have indeed, $j_{par}/j_{\perp} \sim 1$. It was later shown, however, that the "satellite" velocity simulated in the 1990 experiments was large compared with the laboratory Alfven velocity v_A, a case opposite the real ionospheric one, this making the difference between whistler and Alfven (and Lower Hybrid) emission [8]; the experiments had a ratio

$$v_{sat}/v_A \sim 200\ \text{kms}^{-1}/\ 4\ \text{kms}^{-1} \gg 1.$$

* There exists some experimental evidence of circuit-closure in the very near field, through interaction of the plasma clouds of anodic and cathodic contactors in tethers carrying both types. The Plasma Motor Generator (PMG) tether, flown in 1993, was

deployed with the contactors on to a full length of 500 m, at a constant rate of 2-3 m/s [14]. The clouds seemed to overlap for the first 5 seconds (up to 10-15 m contactor distance), the current then dropping to a value 2.5 lower. Tether lengths 50 m and over appear quite safe as far as active cathode-anode interaction is concerned.

* Concerning bare-tether effects on closure, note that OML collection reaches a distance perpendicular to the tether itself that is about $\frac{1}{2}p\sqrt{e\Phi_a / kT_e}$; this distance is about 1 m in our case. The anodic contactor, if on, could thus only interact with the tether over a negligible tether length. Note, next, that the effect of the plasma cloud from the cathodic contactor on bare-tether or anodic-contactor collection would be largest if that cloud were isotropic (over a hemisphere). Equating $I_c \sim 2\pi R_{eff}^2 J_{th}$ to I_{BT} (= I_{OML}) one finds an effective cloud radius independent of N_∞,

$$J_{th} \times 2\pi R_{eff}^2 = J_{th} \times L/2 \times perimeter \sqrt{4e\Phi_a/\pi kT_e},$$

leading to $R_{eff} \sim 4.7$ m for values $L = 200$ m, $p = 8$ cm, $\Phi_a \sim V_S \sim 200$ V, and $kT_e \sim 0.2$ eV, which is very small compared with $L/2$. The anodic cloud, if at all, would be smaller in the ratio $\sqrt{I_a / I_c}$.

* *References*

[1] P.Goldreich and D.Lynden-Bell, Astro. J. **156**, 59 (1969).

[2] S.D.Drell, H.M.Foley, and M.A.Ruderman, J. Geophys. Res. **70**, 3131 (1965).

[3] R.D.Estes, J. Geophys. Res. **93**, 945 (1988).

[4] J.R.Sanmartín and R.D.Estes, J. Geophys. Res. **102**, 14625 (1997).

[5] J.E.P.Connerney et al., Science **262**, 1035 (1993).

[6] J.T.Clarke et al., Science **274**, 404 (1996).

[7] F.J.Crary, J. Geophys. Res. **102**, 37 (1997).

[8] J.R.Sanmartín and M.Martínez-Sánchez, J. Geophys. Res. **100**, 1677 (1995).

[9] J.A.Linker, M.G.Kivelson, and R.J.Walker, J. Geophys. Res. **96**, 21037 (1991).

[10] A.Kopp and A.Schröer, "MHD simulations of large conducting bodies through a planetary magnetosphere", Phys. Scripta (1997).

[11] R.L.Stenzel and J.M.Urrutia, J. Geophys. Res. **95**, 6209 (1990).

[12] R.L.Stenzel and J.M.Urrutia, Geophys. Res. Lett. **25**, 733 (1998).

[13] C.L.Chang et al., Geophys. Res. Lett. **21**, 1015 (1994).

[14] J.E.McCoy et al., "Plasma Motor-Generator (PMG) Flight Experiment Results", Proc. 4th Int. Conf. on Tethers in Space, 57-82, Washington, D.C., 10-14 April 19957

7 Tether Attitude

* Here we consider the large net torque exerted by the magnetic field on our tether because of the unequal current distribution arising from bare-tether current collection (Fig.2 in Sec.2); we discuss how to eliminate or reduce the effects of that torque. For simplicity, we shall use a (rigid body) attitude model, which is crude if only because of solar panels, which make a model with two or more bodies in relative motion more appropriate. Our purpose in trying to balance the tether magnetic torque is to make the problem of attitude control look reasonable; given the mass limitations that our deorbiting tether system will face, one should probably lean on 'semipassive' control techniques. In any case, it should be clear that, even if the magnetic torque is balanced out, some auxiliary stabilisation would be needed.

* *Basic equations*

In the orbital frame, the attitude of our system (made of satellite and tether plus contactors), taken as a rigid body, is governed by the angular momentum equation

$$\frac{d\overline{H}_G}{dt}=\overline{M}_G+\overline{M}_i+\overline{M}_m,\ \overline{H}_G=\overline{\overline{I}}_G\cdot\overline{\omega}\,, \qquad (1)$$

where $\overline{\omega}$ and $\overline{H}_G$ are the system's angular velocity and momentum, and $\overline{M}_G$, $\overline{M}_i$ and $\overline{M}_m$ are gravity, inertial and net magnetic torques. For a circular orbit, and using unit vectors for the orbital frame as in Sec.2 [$\bar{i}$ (upward local vertical), $\bar{j}$ (horizontal and perpendicular to the orbital plane), and $\bar{k} \equiv \bar{v}_{sat}/v_{sat}$], one has

$$\overline{M}_G=3\Omega^2\bar{i}\wedge(\overline{\overline{I}}_G\cdot\bar{i}),\quad \overline{M}_i=-\Omega^2\bar{j}\wedge(\overline{\overline{I}}_G\cdot\bar{j})+2\Omega\overline{\omega}\wedge(\overline{\overline{I}}_G\cdot\bar{j}-I_G\bar{j}). \qquad (2)$$

We also introduce a body frame with unit vectors $\bar{i}_0$, $\bar{j}_0$, $\bar{k}_0$ along the principal axes of inertia at the system's center of mass (**G**), with the tether along $\bar{j}_0$, and both frames coinciding at the nominal orientation (we assume the tether deploys following a

principal inertia direction of the satellite). Once the tether has been deployed our system is quasi-axisymmetric from the inertia point of view, with the moment of inertia around the $\bar{j}_0$ axis, I_{y0}, very small compared with near equal moments I_{x0} and I_{z0}; typical values would be $I_{y0} \sim 10^3$ kg·m^2 and $I_{x0} \approx I_{z0} \approx I_t \sim 3\text{-}10 \times 10^4$ kg·m^2, where I_t is the common value for I_{x0} and I_{z0} when only tether and contactors are considered. In Eqs.(1, 2), $\bar{\bar{I}}_G$ and I_G represent the central inertia matrix of the system and the inertia moment relative to **G,**

$$\bar{\bar{I}}_G \equiv \begin{pmatrix} I_{x0} & 0 & 0 \\ 0 & I_{y0} & 0 \\ 0 & 0 & I_{z0} \end{pmatrix}, \quad I_G = \frac{I_{x0} + I_{z0}}{2} + \frac{I_{y0}}{2},$$

with $I_{x0} \approx I_{z0} \approx I_t$, $I_{y0} << I_t$.

* For the current distribution given in Fig. 2.2, the net magnetic torque $\bar{M}_m$ would just depend on the bare-tether current,

$$\bar{M}_m = -\frac{I_{BT}}{12} L^2 \bar{j}_0 \wedge (\bar{j}_0 \wedge \bar{B}) = \frac{I_{BT}}{12} L^2 \bar{B}_n, \qquad (3)$$

where $\bar{B}_n \equiv \bar{B} - \bar{B} \cdot \bar{j}_0$. Note that $\bar{M}_m \cdot \bar{B}_n$ keeps positive independently of $\bar{B}_n$, which fully rotates once per orbit while current direction is reversed twice (in the nominal orientation); this positive sign may be shown to arise from the fact that current in Fig. 2.2 always flows toward the mast with lower average torque. Figures 7.1 and 7.2 show representative values for the magnetic torque during the first 10 revolutions of a polar, circular orbit at 1600 Km altitude, for the tether used in our dynamical simulations of Fig. 3.15, at nominal orientation, and for low and high solar activity, respectively.

* *Tether equilibrium*

At equilibrium in the orbital frame, and in the absence of magnetic torque, Eq.(1) reduces to the equation $\bar{M}_G + \bar{M}_i = 0$, requiring that the principal axes of inertia

lie along the unit vectors $\bar{i}, \bar{j}$, and $\bar{k}$ [1-6]. When some dissipation is allowed for, the only stable equilibrium corresponds to the axis of minimum inertia ('minor axis') lying on the vertical, and the axis of maximum inertia ('major axis') along $\bar{j}$ (the axis of intermediate inertia lying along $\bar{k}$). A satellite is then said to be 'gravity gradient stabilized', one of its faces continually pointing to Earth (Earth-facing satellites).

With dissipation ignored (for not too long times), there are DeBra-Delp equilibria for the nominal orientation of our tether (minor axis -y_0 axis- along normal to orbit), but they do not apply to our system, which has $I_{y0} << I_{x0}, I_{z0}$. Stability can still be achieved, however, by means of a spin of angular speed ν around the tether axis, which is an axis of near symmetry for the entire system (Thomson equilibrium); with our choice of axes $\bar{i}, \bar{j}, \bar{k}$, opposite Thomson and orbital rotations correspond to $\nu > 0$. No-dissipation stability holds in some domain of dimensionless parameters ν/Ω and k_t,

$$k_t \equiv \frac{I_{y0} - I_{x0}}{I_{x0}} \left(\approx \frac{I_{y0} - I_{z0}}{I_{z0}} \right). \qquad (4)$$

In our case, with k_t very close to -1, Thomson stability requires that $|\nu/\Omega|$ be large.

* For an analysis of Thomson stability including the magnetic torque, we linearize Eq.(1), together with Eqs.(2, 3). To determine $\overline{M}_m$ we use the dipole model for the magnetic field, as given by Eqs.(4) and (5a-c) in Sec.2. To locate the body frame (x_0, y_0, z_0) in the orbital frame we use Euler angles in a 3-1-2 sequence, such that ϕ_3 is the angle rotated about the tangent to orbit, ϕ_1 the angle rotated about the intermediate x_0 axis, and ϕ_2 the angle rotated about the tether axis, y_0. The rotation matrix $\boldsymbol{D}$ between orbital and body frames, $[\bar{i}_0, \bar{j}_0, \bar{k}_0] = [\bar{i}, \bar{j}, \bar{k}]\, \boldsymbol{D}$, then is

$$\overline{\overline{D}} = \begin{pmatrix} \cos\phi_2\cos\phi_3 - sin\phi_2 sin\phi_3 sin\phi_1 & -sin\phi_3\cos\phi_1 & \cos\phi_3 sin\phi_2 + sin\phi_1 sin\phi_3\cos\phi_2 \\ \cos\phi_2 sin\phi_3 + sin\phi_2\cos\phi_3 sin\phi_1 & \cos\phi_3\cos\phi_1 & sin\phi_3 sin\phi_2 - sin\phi_1\cos\phi_3\cos\phi_2 \\ -\cos\phi_1 sin\phi_2 & sin\phi_1 & \cos\phi_1\cos\phi_2 \end{pmatrix}.$$

The satellite angular velocity may now be written as $\overline{\omega} \equiv p\bar{i}_0 + q\bar{j}_0 + r\bar{k}_0$, with

$$p = \dot{\phi}_1\cos\phi_2 - \dot{\phi}_3\cos\phi_1 sin\phi_2,$$

$$q = \dot{\phi}_2 + \dot{\phi}_3 sin\phi_1,$$

$$r = \dot{\phi}_1 sin\phi_2 + \dot{\phi}_3\cos\phi_1\cos\phi_2.$$

We next take $k_t + 1$ small and ν/Ω large, introduce the dimensionless time $\tilde{t} \equiv \Omega t$ and write $' \equiv d/d\tilde{t}$, arriving at

$$\phi_1'' - (c+1)\phi_3' - c\phi_1 + bA_2\phi_3 = -2bA_1, \qquad (5a)$$

$$\phi_3'' + (c+1)\phi_1' - bA_2\phi_1 - (c+3)\phi_3 = -bA_3, \qquad (5b)$$

with A_1-A_3 given by Eqs.(5a-c) of Sec.2, and

$$b \equiv L^2 I_{BT} B_0 / 12 I_t \Omega_E^2, \qquad c \equiv (k_t + 1)\nu/\Omega + 1. \qquad (6)$$

For $L = 200$ m, $I_{BT} = 0.8$ A, and $I_t = 5 \times 10^4$ kg·m^2, we have $b \approx 1$.

* Note that the magnetic torque both acts as external driving and modifies the coefficients of the homogeneous part of (5a, b) through the A_2-terms. Since A_2 oscillates slowly in the $\tilde{t}$ time scale, we take it as constant to find an approximate characteristic equation,

$$\lambda^4 + (c^2 - 2)\lambda^2 - 2(c+1)bA_2\lambda + c^2 + 3c + (bA_2)^2 = 0. \qquad (7)$$

For $b = 0$ (no magnetic torque), Eq.(7) determines the stability of Thompson equilibrium, for small $k_t + 1$ and large $|\nu/\Omega|$; equilibrium is stable when the value of c satisfies either $c < -3$ or $c > 3.35$, all the eigenvalues being then imaginary.

* When the current is on, two eigenvalues have positive real part, regardless of the value of c. For our high inclinations, A_2 is small, and Eq.(7) may be approximately solved to give

$$\mathrm{Re}\,\lambda_{1\text{-}4} \approx \pm \frac{(c+1)bA_2}{\sqrt{c^4 - 8c^2 - 12c + 4}}, \qquad b|A_2| << 1. \tag{8}$$

As a result of (8), the behavior of solutions to Eq.(7) is radically dependent on orbital inclination. For exactly polar orbits, i = 90, A_2 averages to zero, changing sign in Eq.(5b) of Sec.2 every half day (12-16 orbits). For the average growth during half a day, and taking c^4 large in (8), we have

$$\left|\mathrm{Re}\,\lambda_{1\text{-}4}\right| \Delta\tilde{t} \approx \frac{b \times average|A_2|}{c} \times (6-8) \times 2\pi \approx 28\,\beta_m \times \frac{b}{c}, \tag{9}$$

which is typically around 1 for, say, $c \approx 5$. Numerical computations show motion is then stable over long periods.

However, as soon as $cosi \neq 0$, no matter how small, the day-average value of A_2 in Eq.(5b) of Sec.2 is $cosi$, and motion becomes unstable after a certain number of orbits, a result again verified by numerical simulations. For $i = 89°$, say, and $c \approx 5$, we have

$$\left|\mathrm{Re}\,\lambda_{1\text{-}4}\right| \Delta\tilde{t} \approx \frac{b \times \cos i}{c} \Omega \Delta t \approx 1, \tag{9'}$$

for $\Delta t \sim 3$ days. For $\Omega \sim 10^{-3}$ s^{-1} and $I_{x0}/I_{y0} \sim 50$, a value $c = 5$ yields $\nu \sim 0.2$ rad/s.

* Controlling the instability using magnetotorquers onboard the S/C faces difficulties. A torquer of magnetic moment $\overline{m}_0$ adds a term $\overline{m}_0 \wedge \overline{B}$ on the right hand side of Eq.(1). If $\overline{m}_0$ is placed along $\hat{j}_0$, its torque, being normal to $\overline{M}_m$ in Eq.(3), cannot balance it; also, the resulting new term in the caracteristic equation for the linearised form of (1) may be shown not to modify the instability. One can balance $\overline{M}_m$,

on the average, placing $\overline{m}_0$ normal to the tether; the torque $\overline{m}_0 \wedge \overline{B}$, however, has now a component along the tether which can substantially disturb its dynamics, since the inertia moment I_{y0} is so small. Anyway, note that torquers with a very high magnetic moment would be required, $I_{BT}L^2/12$ being about 3×10^3 A·m^2 for $I_{BT} \sim 1$ A and $L = 200$ m. A permanent magnet with such a moment would weigh about 10 kg.

* Another way out of the instability involves contactor rearrangement to balance the torques from the anodic and cathodic masts. This may be achieved by using a third contactor located at the S/C, to eject electrons on the cathodic side, just past the voltage source. This contactor should be required to reduce the cathodic current to a value $I_a + I_{BT}/3$. Note, however, that this would degrade tether performances by reducing the average current to a value

$$\tilde{I} = I_a + 5I_{BT}/12, \tag{10}$$

to be compared with Eq.(12) in Sec.2. A second scheme would keep use of two contactors, located, however, not at mast ends but at a distance $\frac{1}{2} L \times 1/\sqrt{3}$ from the S/C. The average current would now be

$$\tilde{I} = \frac{I_a}{\sqrt{3}} + \frac{1+2/\sqrt{3}}{4} I_{BT}. \tag{10'}$$

* The spin required for Thomson equilibrium would have to be imparted to our system at the start of operation by some control-attitude thruster from the primary mission. Since I_{y0} is very small, however, the angular momentum required is small too,

$$\nu I_{y0} = (c - 1)\, I_{x0}\Omega \sim 3 \text{ N} \times \text{m} \times \text{minute},$$

for $c = 5$ and $I_{x0} = 5 \times 10^4$ kg·m^2. Any dissipation, if small, would just make necessary imparting to the system such angular momentum a number of times. We note, however, that structural damping could make our spinning tether very strongly unstable if the spin

frequency is higher than the lowest (vibrational) resonant frequency. A simple estimate shows that this would be the case for CTM Size-1 masts (Sec.3) of length $L/2 \sim 100$ m; to avoid this instability one might need using a length $L/2 \sim 50$ m, making our tether not competitive against electrical thrusters (see Sec.10). We assume here that, as suggested by some nonlinear analyses, stabilizing nonlinear effects allow using masts at spin frequencies above the fundamental vibrational frequency (see Final Report for *WP*-200).

References

[1] C. Hughes, Spacecraft Attitude Dynamics, John Wiley & Sons, New-York (1986).

[2] J. R. Wertz, Spacecraft Attitud Determination and Control, Ed. Reidel Publ. Co., Dordrecht, Holanda, (1978).

[3] F. P.J.Rimrott, Introductory attitude dynamics, Ed.Springer-Verlag, New York (1989).

[4] M. H. Kaplan, Modern Spacecraft Dynamics and Control, Ed. John Wiley & Sons, New York (1976).

[5] T. R. Kane, P. W. Likins and D. A. Levinson Spacecraft Dynamics, Ed. Mac Graw-Hill, New-York (1983).

[6] V. Beletskii, Essais sur le mouvement des corpes cosmiques, Ed. MIR, Moscu (1986).

8 Thermal Balance

* As with tethers in general, each mast can be considered thermally insulated from the S/C because of its length. On the other hand, its entire surface may be taken as isothermal, both because heat input turns out to be nearly uniform over the entire mast length, and because the mast is spinning (and has a small cross-section). There is thus no differential heating. Thermal cycling, however, can pose difficulties as usually.

* In the heat balance equation for each mast,

$$C\frac{dT}{dt} = \dot{Q}_{Sun} + \dot{Q}_{albedo} + \dot{Q}_{Earth} - \dot{Q}_{out} + \dot{Q}_I , \qquad (1)$$

the first two terms in the right hand side are the heat inputs from direct and reflected solar radiation, ranging from maximum values

$$(\dot{Q}_{Sun} + \dot{Q}_{albedo})_{max} = \frac{A}{\pi}\alpha_{UV}\,\dot{w}_s + AF\alpha_{UV}\,a\dot{w}_s \approx \frac{A}{\pi}1.3\alpha_{UV}\,\dot{w}_s , \qquad (2)$$

to zero during eclipses. Here, A is mast surface area, α_{UV} is absorptance (at visible and UV frequencies), $\dot{w}_s$ is the solar constant ($\approx 1.4 \times 10^3$ w/m^2), and a is Earth's albedo (≈ 0.34). In estimating the projected area in the direction of Sun, we took a circle for the mast cross-section. We also took $F \approx 0.3$ for the viewfactor (horizontal tethers at about 1000 km altitude [1]).

The third and fourth terms in Eq.(1) account for thermal radiation (input from Earth, output from mast),

$$\dot{Q}_{Earth} - \dot{Q}_{out} = A\varepsilon_{IR}F\,\dot{w}_E - A\varepsilon_{IR}\,\sigma_B T^4 \approx A\varepsilon_{IR}(0.3\dot{w}_E - \sigma_B T^4), \qquad (3)$$

where ε_{IR} is the emittance (at infrared frequencies) and $\dot{w}_E$ is Earth's heat emission ($\approx 0.24 \times 10^3$ w/m^2). The last term in Eq.(1), arising from the electron bombardment in the bare-tether collection process, only applies to the anodic phase of the mast,

$$\dot{Q}_I \approx V_s I_{BT} = \frac{A}{\pi} eV_s \times N_\infty \sqrt{\frac{2eV_s}{m_e}} \approx \frac{A}{\pi} \dot{w}_I , \tag{4}$$

$$\dot{w}_I \approx 0.019 \times (N_\infty/10^5 \text{ cm}^{-3}) \times 10^3 \text{ w/m}^2. \tag{5}$$

Ohmic heating is clearly negligible (~ 1 watt).

* Assuming the mast heat capacity is small, its temperature T will make excursions between minimum or "cold", and maximum or "hot" values. The cold temperature will occur when the mast acts cathodic during eclipses, the third and fourth terms in Eq. (1), as given in (3), then balancing each other,

$$T_{cold} \approx (0.3\dot{w}_E/\sigma_B)^{1/4} \approx 190 \text{ K}. \tag{6}$$

The hot temperature occurs in the anodic phase at maximum values of solar irradiation. One may take into account the electron bombardment input $\dot{Q}_I$ by just writing $\alpha_{UV} \rightarrow \alpha_{UV} + N_\infty/10^7 \text{ cm}^{-3}$ in Eq.(2), the hot temperature now satisfying

$$\sigma_B T_{hot}^{\ 4} = 0.3\dot{w}_E + \frac{1.3\dot{w}_s}{\pi\varepsilon_{IR}}\left(\alpha_{UV} + \frac{N_\infty}{10^7 cm^{-3}}\right). \tag{7}$$

We can get from (7) a lower bound for maximum temperature by ignoring both $\dot{Q}_{Earth}$ and $\dot{Q}_I$, which are comparatively small,

$$T_{hot} > (1.3\alpha_{UV}\,\dot{w}_s/\sigma_B\pi\varepsilon_{IR})^{1/4} \approx 318\,(\alpha_{UV}/\varepsilon_{IR})^{1/4} \text{ K}. \tag{8}$$

Earth's radiation can be ignored for $\alpha_{UV} >> 0.12\varepsilon_{IR}$; $\dot{Q}_I$ can be reasonably ignored except at F-layer plasma densities. To keep both maximum temperature and thermal excursions low, in order to avoid solar-induced thermal excitation, one might thus need covering the masts with some (conductive) high-emittance coating.

* One may easily show that mast temperature will indeed quasisteadily follow heat input cycles. A Sener's CTM, Size 1, 100 m long mast has heat capacity about 1.2 $\times 10^3$ J/K and surface area $A \approx 8$ m^2. When the heat input jumps as the mast moves from

solar shadow to full irradiation, its temperature takes only $\Delta t \approx 0.9/\alpha_{UV}$ minutes in rising 150 K. This must be compared with cycle times of 25-50 minutes (1/4-1/2 orbital periods).

References

[1] J. Carroll, "Guidebook for Analysis of Tether Applications", in Tethers In Space Handbook (2nd edition), NASA, Washington D.C. (1989).

9 Demonstration Mission

* Although there are important points yet to be settled and preparatory tasks to be carried out, we suggest the short-tether concept should be tested soon as a secondary mission on board some appropriate S/C, if available. S/C mass should be 500-1000 kg and orbital inclination over 70°. To take advantage of solar near-maximum conditions, keeping deorbit time under 1 year, altitude should not exceed 800 Km, with deorbit starting no later than early 2002. With only 2½ years left till start, only a S/C with short (primary) operational life would fit the conditions.

* Since there is no need for optimal design, we propose just using Size-1 masts from Sener's CTM family, each 100 m long (see end of Sec.7), the mass of the two-mast tether being 6.9 kg. Masts should be covered with some conductive polymer coating for protection from thermal cycling (and possibly, F-layer oxygen attack). Mass of deployer mechanism and box for Size-1, allowing for easy storage and retraction of 20 m masts, stands at 1kg. Although the radius of the stowing drum is independent of mast length, a larger box and two drums would be needed. On the other hand, allowing for no retraction saves weight in the deployment mechanism (two clutches plus retraction drive). On the whole, the mass of our deployer could be less than 2 kg.

* *Enclosed-keeper* hollow cathodes would be used as contactors. We propose Proel start developing a model in its Ncc series intermediate between A/300 and A/5000 models. Interpolation on Ncc-family data for the ½ - 2 A range of currents, yields an expellant flow rate of 3.4 kg/year×A, and a running power under 20 watts. With deorbiting time under 1 years, each contactor, if only working half time (as cathode), would consume about 1.7 kg of (Xenon) expellant. From typical tankage data for resistojets and arcjets (5% of propellant mass in Ref.1) we would add 10% of

expellant mass for tankage and plumbing, for a total of 2 kg per contactor when adding the very small mass of the contactor itself.

* The voltage source (~ 200 V) biasing and driving the anodic bare-mast current requires powering by solar arrays at the S/C. The electromotive force induced in the tether by its orbital motion adds another 25-50 V, comes out comparable to the voltage bias required by the cathodic contactor, which is around 30 V. Power requirements, including the 20 watts cathodic running power, could reach up to 300 watts. For the mass of the Power Processor Unit (PPU), which is about proportional to the power; we take a value 4-6 kg/kw, intermediate between typical values for arcjets and hydrazine resistojets, and Hall and ion thrusters [1], or about 1.5 kg. On the whole, we would have a total mass of less than 15 kg.

* Battery masses have not been included in the above mass budget. There are a number of questions and decisions pending, battery cycling being one. Rocket-thrust must set our system spinning at the start of operation, an angular momentum of 3.4 Nm × minute being required for (Thomson) stability; the amount of dissipation arising from eddy currents or thermoelastic deformation is yet to be determined, but it may make necessary imparting such angular momentum more than once to the system. Whether a net magnetic torque may make attitude control too hard, and then ways to make that torque vanish through contactor rearrangement, remain to be determined too. A full parametric study of the entire system should be carried out.

* Figures 1-4 show deorbiting performances for initial altitudes of 500, 800, 1200, and 1600 km. In the parameter $\varepsilon = 2M/pL^2\sqrt{V_S}$, total spacecraft mass M is in kg, mast perimeter p and full length L in meters, and V_S in volts. For M = 500 kg, our

system would have $\varepsilon = 2.1 \times 10^{-2}$. In the calculations we assumed each contactor was switched off when anodic.

* *References*

M. Martínez-Sánchez and J.E. Pollard, J. Propulsion & Power, **14**, 688 (1998).

10 Trade-off Study

* Our short-tether system is here compared with electric thrusters as regards operational cost for the deorbiting mission, with requisites on both total impulse $F\tau$, and allowed duration τ; although cost (indirectly, mass) is the main trade-off characteristic, there are limitations on required power too. Since deorbiting is a secondary mission to be carried out at the end of the satellite operational life, a deorbiting system should somehow satisfy additional requirements: (i) minimal implementation of new hardware; (ii) no new electric power facilities, and weak dependence on batteries (probably degraded at operational life end); (iii) high reliability and low R&D cost of system. Only thrusters with operational status will be considered.

* *Electrical Thrusters*

The cost of placing and operating a propulsive system in LEO orbit can be split into propellant, hardware, and electricity contributions,

$$C = c_P M_P + c_H M_H + \gamma c_w P_w, \qquad (1)$$

with M_P (M_H) propellant (hardware) mass, and P_w electric power. Typical values of specific costs are $c_H = 2c_P = 30$ k$/kg, and $c_w = 1000$ k$/kw [1]. For the electricity generation system of electric thrusters, i.e. solar arrays and batteries, we only consider a residual cost (a small fraction γ of power) attributable to the deorbiting mission, arising, say, from a longer lifetime design.

* Hardware mass M_H is basically made of two parts. The propellant tankage and plumbing mass can be written as a small fraction of propellant mass, αM_P. The rest of the mass [thruster itself and power processor unit (PPU)] can be taken as proportional to power, $\delta \times P_w$. Table 1, based on data from Refs. 1, 2, presents typical values of parameters such as α and δ (kg/kw), for different thrusters; values for chemical propulsion, where appropriate, are also included for comparison. Because deorbiting

requirements are much greater, we assume hardware is new and mission dedicated, not allowing for cost sharing with other missions, like attitude control.

* The propellant mass is

$$M_P = \dot{m}\,\tau = F\tau/v_{sp}, \tag{2}$$

where $v_{sp} \equiv g_E I_{sp}$ is the specific impulse (in velocity units), relating thrust F to propellant flow rate $\dot{m}$. The mission total impulse is determined by mission parameters M (full spacecraft mass) and Δh (deorbiting height drop, down to 250 Km). Typical values are $M \sim$300-1000 kg, $\Delta h \sim$500-1500 Km. From Eq.(1) in Sec.2, one readily finds

$$F\tau = \tfrac{1}{2}\tilde{\Omega}\, M\Delta h, \tag{3}$$

with some mean value for $\Omega = \Omega_E(R_E/a)^{3/2}$.

* The power required for electric propulsion is

$$P_w = v_{sp}F/2\eta \approx \tfrac{1}{2}\,\tilde{\Omega}\, M\Delta h\, v_{sp}/2\eta\tau, \tag{4}$$

where η is thruster efficiency. Using (2-4) in Eq. (1) one finds mass M_d and cost of the deorbiting system in terms of $M\Delta h$ and τ,

$$M_d = M_P + M_H = \frac{\tilde{\Omega}\, M\Delta h}{2v_{sp}}\left[1+\alpha+\frac{\delta}{2\eta}\frac{v_{sp}^{\,2}}{\tau}\right], \tag{5}$$

$$C = c_P\,\frac{\tilde{\Omega}\, M\Delta h}{2v_{sp}}\left[1+2\alpha+\frac{\delta+\gamma\, c_w/2c_P}{\eta}\frac{v_{sp}^{\,2}}{\tau}\right]. \tag{6}$$

For chemical propulsion one would just have

$$C = c_P\tilde{\Omega}\, M\Delta h/2v_{sp}.$$

* Figure 1 shows power, mass, and cost of deorbiting system as given by Eqs.(4-6), for different types of thrusters, in terms of deorbiting time τ. Since all three quantities P_w, C and M_d are proportional to $M\Delta h$, we present values normalized to $M\Delta h$. Note that giving the thrust F determines τ in Eq.(3). Curves are shown for

typical lifetimes of systems (see Table 1). As longer deorbiting times are considered, costs are reduced and thrusters with larger specific impulses become more attractive. The required electric power decreases with τ for a given thruster type. Computed values of required power are within present ranges for the corresponding devices (see Table 1).

	α	δ (kg/kw)	v_{sp} (km/s)	η (%)	P_w (kw)	Peak Volt(V)	Lifetime (months)
Chemical	--	--	2.1	--	--	--	$\ll 1$
Resistojet	0.1	2.5	3	80	0.5 - 1.5	28	0.7
Arcjet	0.1	3	5	35	0.3 - 2	100	1.5
Hall thrus.	0.2	11	16	50	0.3 - 6	300	10
Ion thrus.	0.2	13	27	65	0.2 - 4	900	14

Table 1

Since, in general, very short deorbiting times are not required, the best options (within this group) are Hall thrusters for $\tau \sim$ 2-3 months, and ion thrusters for longer allowed deorbiting times. Note, however, that Hall and ion thrusters require high power and peak voltage. Table 2 resumes their performances for long deorbiting times with thrusters operating continuosly.

	τ (month)	C/MΔh ($/kg.km)	$(M_d/M) \times (10^3 km/\Delta h)$	$P_w/M\Delta h$ (w/kg.km)
Hall thruster	6	1.09	.054	638
Hall thruster	9	1.00	.051	425
Ion thruster	9	0.76	.035	552
Ion thruster	12	0.69	.033	414

Table 2

* *Proposed Tether System*

We can determine an equivalent "specific velocity" for the tether as regards expellant mass consumption, even though there is no direct relation between tether thrust (drag) and expellant flow rate in the contactors. Tether drag is $(R_E/a)^{3/2}$ times the right hand side of Eq. (8) in Sec.2,

$$F = fI_c B_{eq} L\,, \qquad f \equiv \frac{\tilde{I}}{I_c}\frac{E_m}{v_{sat} B_{eq}} = \frac{\tilde{I}}{I_c}\frac{4}{\pi} sin\, i\,. \tag{7a, b}$$

For our high orbital inclinations, the tether factor f is close to unity; to be definite, we shall take $I_a = 0, \rightarrow \tilde{I}/I_c = 3/4, f = (3/\pi) sin\ i,$ in this discussion. We now have a consumed expellant mass

$$M_{exp} = <\dot{m}_c \tau> = <\dot{m}_c/I_c \times I_c/F \times F\tau>, \tag{8}$$

where I_c/F is taken from (7a), and $\dot{m}_c/I_c$ from Eq.(1) in Sec.5,

$$\frac{\dot{m}_c}{I_c} \approx \frac{\sqrt{m_e m_i}}{e\eta_c}\,. \tag{9}$$

Using the value $\dot{m}_c/I_c = 3.4$ kg/year×A found for our (Proel) Xenon contactor (Sec.9) we obtain $\eta_c = 0.026$. Equation (8) for expellant mass now takes the form of Eqs.(2, 3),

$$M_{exp} \approx \tilde{\Omega} M\Delta h/2v_{sp}\,, \tag{10}$$

with a tether "specific velocity",

$$"v_{sp}" \equiv F/\dot{m}_c = f\eta_c \omega_{LH} L, \tag{11}$$

where $\omega_{LH} = e\tilde{B}_{eq}/\sqrt{m_e m_i}$ is some mean value of the Lower Hybrid frequency of expellant ions at the magnetic equator; taking $\tilde{B}_{eq} \approx B_0$ for simplicity, we find $\omega_{LH}{}^0 \sim 1.1 \times 10^4 s^{-1}$ for Xenon. The main feature of the tether specific impulse is its dependence on tether length; for $L = 250$ m, $\eta_c = 0.026$, and $i = 90°$, one has $v_{sp} \approx 68.2$ km/s, well above ion thruster values.

* As general with electrical propulsion, the hardware mass of our system has contributions from tankage and plumbing (including the very small deployer mass, Sec.9), αM_{exp}, and from contactors and PPU, δP_w; characteristic values are $\alpha = 0.1$ and $\delta = 4$ kg/kw (see Sec.9). An important addition here is the tether mass, ρtpL, where we can write $\rho t \equiv \rho^* p$ for geometrically similar mast cross-sections, as in the CTM family (Sec.3), for which we have $\rho^* \approx 0.6\times10^{-3}\rho \approx 4.95$ kg/m^3.

* Neglecting the small running power for the contactor, we have a tether power,

$$P_w = V_s I_c = \frac{\tilde{\Omega}\, M\Delta h}{2v_{sp}} \times \frac{\eta_c e V_s}{\tau\sqrt{m_e m_i}} \quad . \tag{12}$$

Both mass and cost of our tether system may now be written as

$$M_d = \frac{\tilde{\Omega}\, M\Delta h}{2v_{sp}}\left[1+\alpha+\delta\,\frac{\eta_c e V_s}{\tau\sqrt{m_e m_i}}\right] + \rho^* p^2 L, \tag{13}$$

$$C = c_P\,\frac{\tilde{\Omega}\, M\Delta h}{2v_{sp}}\left[1+2\alpha+\left(2\delta+\gamma\, c_w / c_P\right)\frac{\eta_c e V_s}{\tau\sqrt{m_e m_i}}\right] + 2c_P\rho^* p^2 L, \tag{14}$$

with v_{sp} ($\propto L$) in (12-14) given by Eq.(11). Note that P_w, M_d and C are determined in terms of $M\Delta h/L$, V_s/τ and $p^2 L$. Also, using (3) and (7a) in equating I_c to the OML current in Eq.(4') of Sec.2, taken at some deorbit-averaged density $\tilde{N}_\infty$, yields a relation between mission ($M\Delta h$ and τ), design (L, p, and V_s), and ambient ($\tilde{N}_\infty$) parameters,

$$\frac{\pi\tilde{\Omega}}{feB_{eq}}\,\frac{M\Delta h}{pL^2} = \tilde{N}_\infty \tau\sqrt{\frac{2eV_s}{m_e}} \quad . \tag{15}$$

Figure 2 shows relation (15).

* We find that our system is competitive in some bounded parametric domain; it does fail when L, p, or V_s move to large or small values. Start assuming that the τ-term in the bracket of Eq.(14) may be ignored. For each $M\Delta h$ mission-value there is

then a length, L_{opt}, minimizing the cost C; note that the no-buckling condition of Sec.3,

$$L < L_{cr} \propto \sqrt{p} \quad \rightarrow \quad p > p_{cr} \propto L^2, \tag{16}$$

allows writing $p \propto L^2$ in the last (tether mass) term of Eq.(14) when minimizing C, making that term increase with L as L^5. The mimimum-C length now behaves as $L_{opt} \propto (M\Delta h)^{1/6}$; also, tether mass then only accounts for 1/5 of total cost. We now show that there are both upper and lower bounds to L_{opt}, and thus to $M\Delta h$.

For high $M\Delta h$ values, note that ambient plasma densities involved determine a maximum perimeter p for the efficient OML current-law to apply (Sec.3); this determines a maximum mast length in (16). At the opposite end, the tether specific velocity [proportional to L in (11)] will drop as L_{opt} decreases with $M\Delta h$, finally making our system less efficient than ion and Hall thusters. Roughly, we find our tether superior to those electrical thrusters for $L_{opt}/2$ in the narrow range 75-125 m, which, nonetheless, allows a broad mission range for $M\Delta h$ [$\propto L_{opt}^6$]. Clearly, the tether proves better at the high range end (recall, however, the comment at the end of Sec.7). Note finally that applying to Eq.(13) arguments similar to those just used for (14) shows that L_{opt} makes M_d take a value close to its particular minimum.

* Next we note that the left hand side of (15) (slowly) increases with mission value $M\Delta h$ as L_{opt}^2, or $(M\Delta h)^{1/3}$; for the range of allowed values of $M\Delta h$ previously found, that left hand side then lies itself within a narrow range. The average plasma density $\tilde{N}_\infty$, while varying with deorbiting start altitude, is critically dependent on the starting date relative to the solar cycle (Secs.3 and 9). Using a source voltage V_s around 200 V, we find that, considered as starting dates, there are 3-4 years in the cycle with $\tilde{N}_\infty$ such that deorbit time τ is 1-2 years.

For other starting dates, $\tilde{N}_\infty$ is found to be greatly smaller, and our system proves ineffective in a new way: mission duration τ greatly increases, deorbit dragging on till the next solar maximum (except for too small $M\Delta h$, for which, as noted above, our tether is less efficient than electrical thrusters). Augmenting V_s will not help: the τ-terms in Eqs.(13, 14) would raise cost C and mass M_d above corresponding values for Hall and ion thrusters, well before the right hand side of (15) is noticeably increased. Note here, from Fig.1, that Hall and ion systems do allow mission durations that make the τ-terms have a small effect in Eqs.(5, 6). Figures 3 and 4a-i show C, M_d, and P_w versus τ for a variety of values of particular parameters ($\tilde{N}_\infty$, $M\Delta h$, L, L/p, and V_s); we took $\gamma = 0.1$, $\tilde{\Omega} = \Omega_E$, and L/p = 250 m / 7.65 cm in most cases (see Sec.3). If contactor arrangements such as suggested in Sec.7 proved necessary, performance would somehow be degraded.

* *Vertical, flexible tether system*

The simplest configuration for such system consists of (i) a long bare tether, (ii) one cathodic contactor placed at the spacecraft, and possibly (iii) a low power unit to just operate the contactor. For the mass and monetary cost of this de-orbiting system, equations similar to (13) and (14) are used,

$$M_d = \frac{\tilde{\Omega} M \Delta h}{2 v_{sp}} (1+\alpha) + \alpha_t \rho_v A_t L \,, \qquad (17)$$

$$C = c_p \frac{\tilde{\Omega} M \Delta h}{2 v_{sp}} (1+2\alpha) + 2 c_p \alpha_t \rho_v A_t L \,. \qquad (18)$$

Here, the contribution of the low-power unit has been neglected, ρ_v and A_t are tether density and area of cross-section, and α_t, about 2.5 typically, accounts for the masses of deployer and ballast at end of tether. A large ballast mass and a complex deployer are needed because deployment of vertical, flexible tethers makes use of gravity-gradient

pulling. For a vertical tether made of aluminum, however, $\alpha_t \rho_v$ would be actually smaller than the CTM-mast density ρ in Eqs.(13,14).

The specific velocity in Eqs.(17,18) is still given by (11), where, however, f is now small: In Eq.(7b) for f one must here replace law (7b) of Sec.3, $E_m / v_{sat} B_{eq} = (4/\pi)\ sin\ i$, by law (7,7'), making $E_m / v_{sat} B_{eq}$ small at high inclinations. A low f value in Eq.(7b) means that, in order to beat our tether system, the vertical tether must be quite long (L larger than about 250 m $\times$ 2/ $sin\beta_m \sim 2.5$ km). This would make the second terms in (17,18) too large but for the fact that there is now no buckling condition. This allows taking A_t smaller as L is increased, ohmic effects, however, setting in at some point.

A detailed analysis of the current-voltage characteristic of a vertical bare tether with ohmic effects was given by Sanmartín et al. (Ref.1 of Sec.2). Potential and current along the electron-collecting part of the tether ($\Phi > 0$, Fig.5) verify

$$\frac{d\Phi}{dx} = -E_m + \frac{I}{\sigma_t A_t}, \qquad \frac{dI}{dx} = eN_\infty \frac{p}{\pi}\sqrt{\frac{2e\Phi}{m_e}} \quad (\Phi>0), \qquad (19a,b)$$

where σ_t is tether conductivity, and OML collection has been assumed. Ohmic losses limit the current that can be collected to the short circuit value, $I_* = \sigma_t A_t E_m$. If $I_c < I_*$ one has

$$I(x) = I_c, \qquad \Phi(x) = -E_m\,(x - L_{col})(1 - I_c/I_*),$$

in the cathodic ($\Phi < 0$) segment of the tether, with L_{col} the length of the electron-collecting segment.

* Equations (19a,b) may be now used to show that the current reaches the short circuit value, $I_c = I_*$, if i) a voltage source at C keeps the contactor at a potential $\Phi_c(I_c)$ ($|\Phi_c| \sim$ 20-30 V), and (ii) $L > 4\,L_*$, with

$$L_* = \left(\frac{9\pi^2 m_e E_m \sigma_t^2 A_t^2}{32 e^3 N_\infty^2 p^2}\right)^{1/3} = 19.6\,\mathrm{km} \times \left(\frac{E_m}{100\mathrm{V/km}}\right)^{1/3} \left(\frac{A_t/p}{1\mathrm{mm}} \frac{10^{11}\,\mathrm{m}^{-3}}{N_\infty}\right)^{2/3}, \qquad (20)$$

where we used the conductivity of aluminum. We then have $L_{col} = 4\,L_*$, $\Phi_A = E_m L_*$, and $I(x) = L_*$ throughout a segment at zero bias. We also have $\tilde{I}/I_c = 1 - L_*/L > 3/4$ in $f = (\tilde{I}/I_c)\,E_m / v_{sat} B_{eq}$. Note that $\mathrm{L}^* \propto (A_t/p)^{2/3}$ can be reduced by using thin tapes as tethers. Also, the cost of the low voltage source, placed at the spacecraft, should be small.

In this ohmic-dominated limit, the OML current equals $I_* = \sigma_c E_m A_t$, relation (15) taking here the form

$$\frac{v_{sat} \tilde{\Omega} M \Delta h}{\sigma_t E_m^2} = 2 \frac{\tilde{I}}{I_c} \tau A_t L. \qquad (L > 4\,L_*). \qquad (21)$$

One may thus have moderate tether masses in Eqs. (17,18) at the price of long deorbiting times. Because the product of tether mass and deorbit time varies as inversed squared induced field E_m, the vertical tether may prove useless at the high inclinations of interest.

* Figure 6 depicts relative costs and masses of vertical tethers for different plasma conditions, orbit inclinations and de-orbiting missions. Within some parametric domain there is practically a universal curve independent of $\tilde{N}_\infty$. This reflects that, contrary to our tether with anodic bias supplied by an external source, a long tether based on induced voltage does not degrade with adverse plasma densities: as $\tilde{N}_\infty$ decreases, L_* and, thus, the anodic length L_{col} increases. Also, relative cost and mass at fixed τ depend weakly on $M\Delta h$ provided L is appropriately scaled. On the other hand, Figure 6 shows vertical tether performance is heavily dependent on orbit inclination through the (average) E_m value. The consequence is that, for high latitude orbits (i > 60°-65°), with

E_m no larger than 20-25 V/km, the vertical tether is less attractive than our horizontal, rigid tether (except at very low $\tilde{N}_\infty$, when electric propulsion is, anyhow, more efficient). Furthermore, for $i > 90°-\beta_m \approx 78.5°$, long, vertical tethers present an additional drawback: since the current direction reverses every half-orbit a second contactor must be installed at the far end of the tether; long-time power supply of this contactor might be complex. Independently, a vertical tether at high inclinations, poses great dynamical difficulties because the magnetic force is then almost horizontal, driving out-of-plane oscillations at the 2Ω frequency. For $i < 60°$, however, vertical tethers present a clear advantage (even in de-orbiting time) over any other braking system.

References

[1] R.D. Estes, E.C. Lorenzini, J. Sanmartín, J. Peláez, M. Martínez-Sánchez, L. Johnson, and I. Vas, *Bare tethers for electrodynamic spacecraft propulsion,* J. Spacecraft & Rocket (in press).

[2] M. Martínez-Sánchez and J.E. Pollard, J. Propulsion & Power, **14**, 688 (1998).

ORIGIN	ACRONYM	EXPELLANT	MASS FLOW RATE (max. readings)	Kg/Year (expellant)	ELECTRIC POWER (Watts)	TYPE	REF.	COMMENTS
USA	SEPAC	Xe	37.4 Sccm	107.6	> 270	RC	7,8	Flown on STS-45
"	PMG	Xe	15.0 "	43.17	Batteries	OK	9	Flown on delta Rocket
"	ISS	Xe	6.0 "	17.27	53.8 peak, 36 running	EK	2	Planned fur Space Station
EUROPE	STRV	Xe	2.0 Sccm	5.8	< 20	OK	3	ESA Approved
"	Proel A/300	Xe	0.5 "	1.44	38 peak, 7 running	EK	4,5	Engineering model & Testing
"	" A/5000	Xe	3.5 "	10.07	130 " 110 "	EK	"	"
"	" A/10000	Xe	5.5 "	15.83	140 " 110 "	EK	"	"
RUSSIA	EPICURE	Cs	30 mg/seg	945	2 Kw	ArcJet	6	Tested in COSMOS flight and sounding rocket
"	OKA	Cs	30 mg/seg	945	2Kw	"	6	"
"	PROGRESS	Xe	5.5 Sccm	15.6	240 peak, 150 running	EK	10	--------
"	GPC-1	Xe, Ar, Kr	-------	-----	Not rated	EK	6	--------
"	GPC-2	Xe, Ar, Kr	-------	-----	Not rated	EK	6	--------

RC → RING CUSP

EK → ENCLOSED KEEPER

OK → OPEN KEEPER

TABLE 4-1

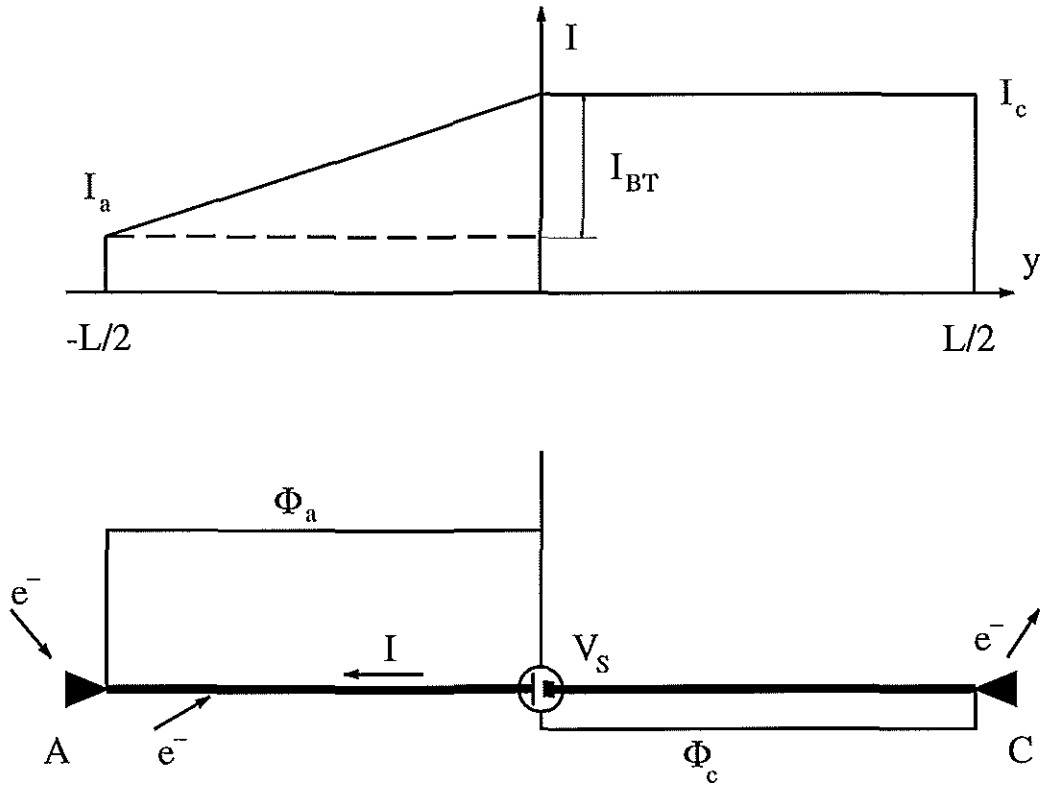
I
I_c
I_{BT}
I_a
y
-L/2
L/2
Φ_a
e^-
I
V_S
e^-
A
e^-
Φ_c
C

Fig. 2.1

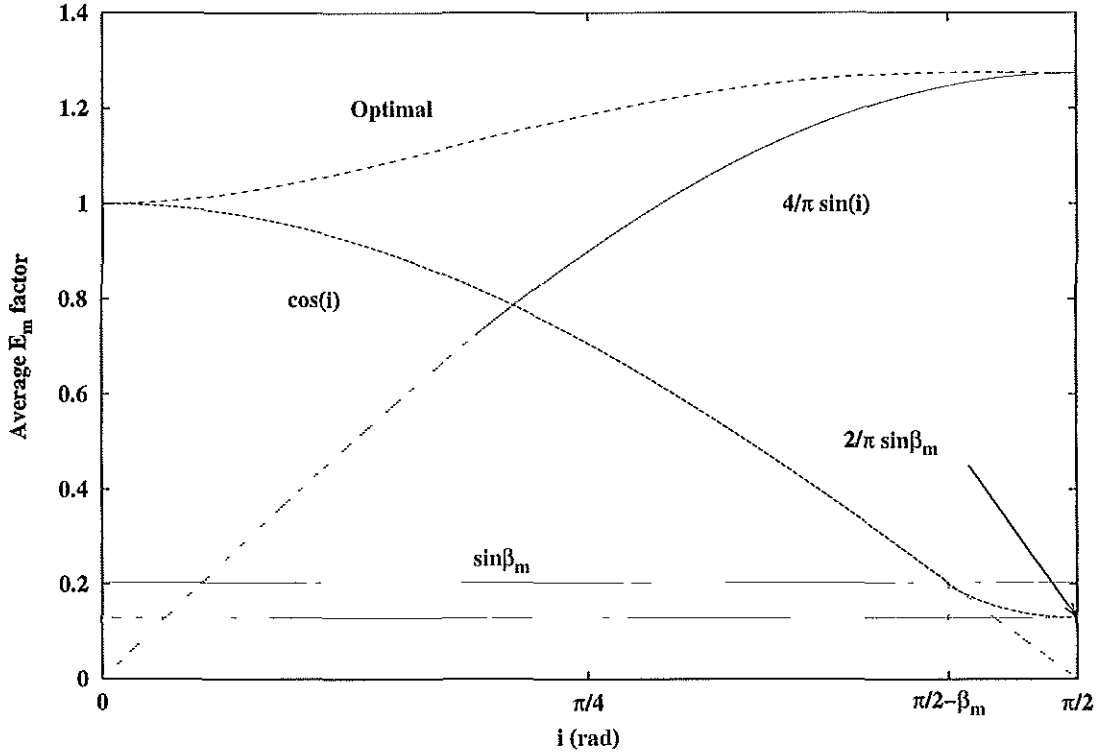
Optimal
4/π sin(i)
cos(i)
2/π sinβm
sinβm
Average Em factor
i (rad)
0
π/4
π/2−βm
π/2
0.2
0.4
0.6
0.8
1
1.2
1.4

Fig. 2.2

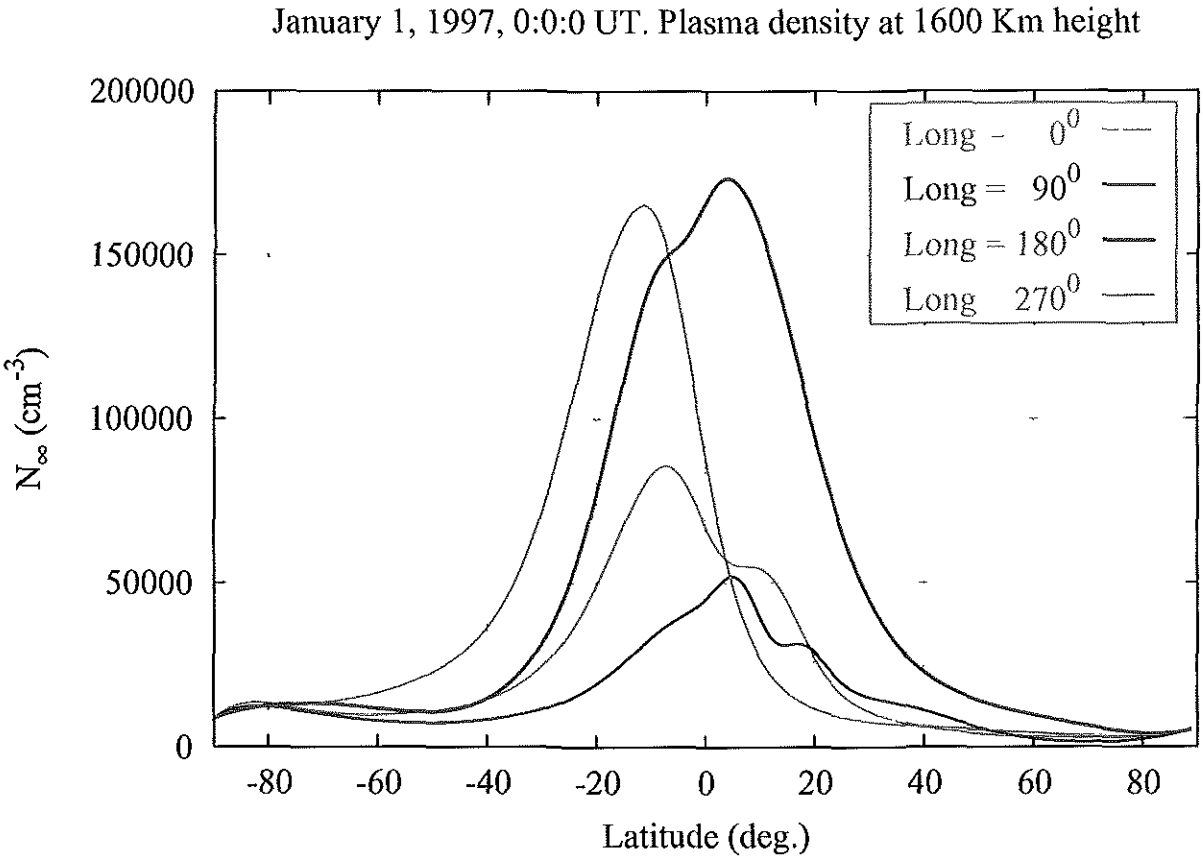
January 1, 1997, 0:0:0 UT. Plasma density at 1600 Km height
Long - 0⁰
Long = 90⁰
Long = 180⁰
Long 270⁰
200000
150000
100000
50000
0
N∞ (cm-3)
-80
-60
-40
-20
0
20
40
60
80
Latitude (deg.)

Fig. 3.1

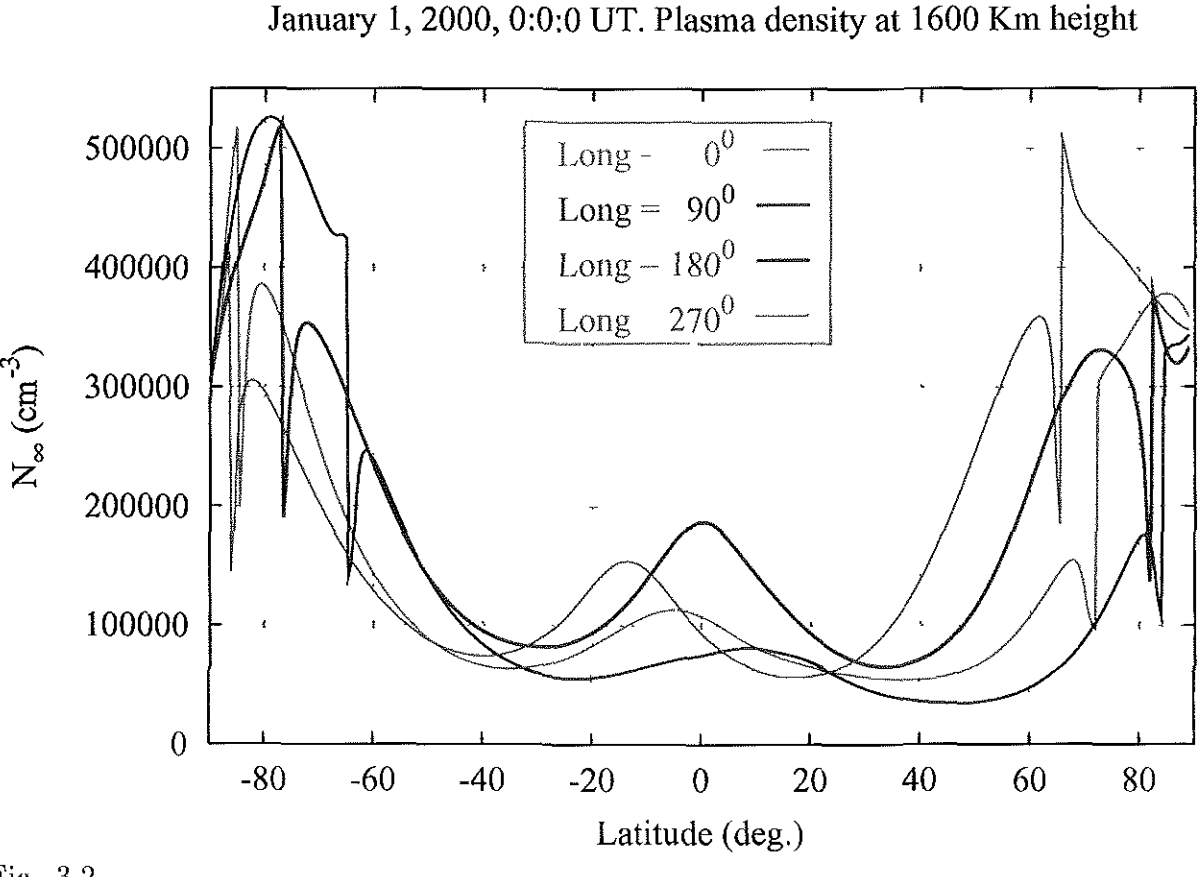
January 1, 2000, 0:0:0 UT. Plasma density at 1600 Km height
Long - 0⁰
Long = 90⁰
Long – 180⁰
Long 270⁰
500000
400000
300000
200000
100000
0
N∞ (cm-3)
-80
-60
-40
-20
0
20
40
60
80
Latitude (deg.)

Fig. 3.2

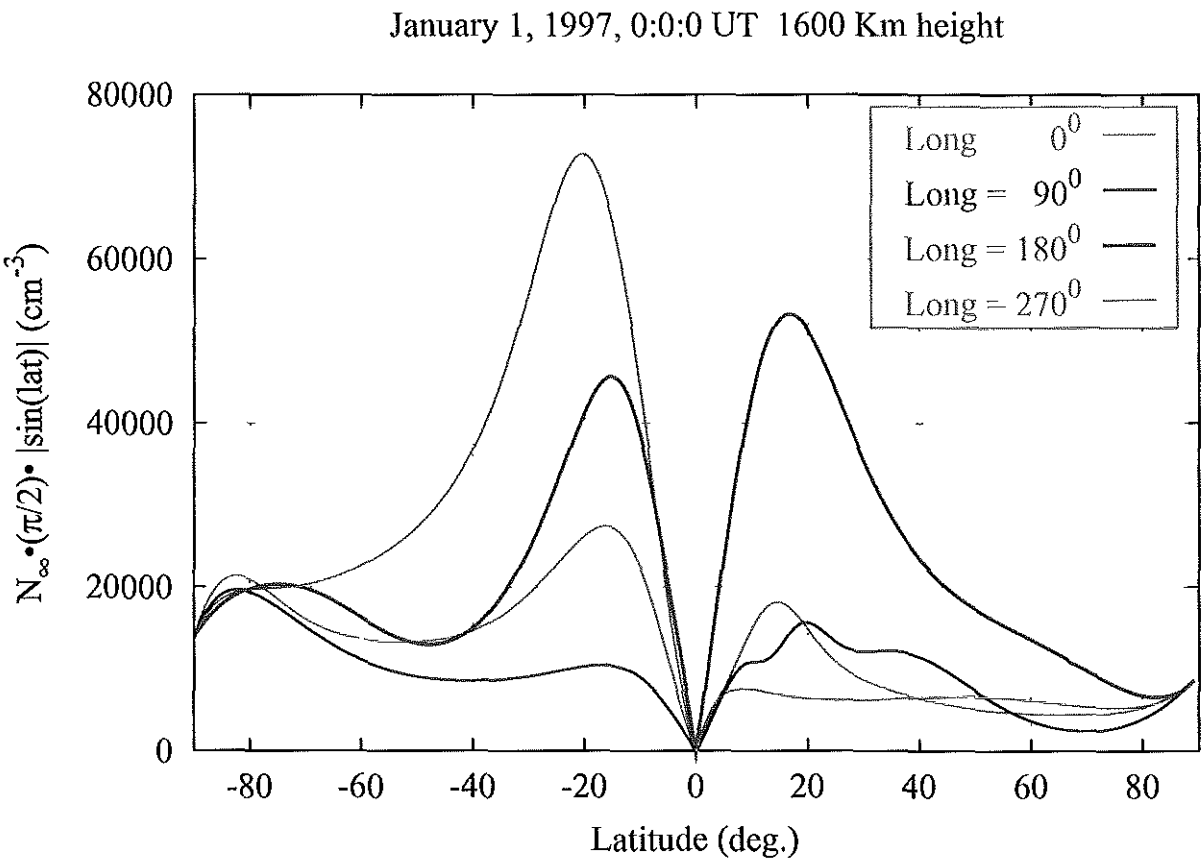
January 1, 1997, 0:0:0 UT 1600 Km height
80000
60000
40000
20000
0
-80
-60
-40
-20
0
20
40
60
80
Latitude (deg.)
$N_\infty \cdot(\pi/2)\cdot |\sin(lat)|$ (cm^{-3})
Long 0^0
Long = 90^0
Long = 180^0
Long = 270^0

Fig. 3.3

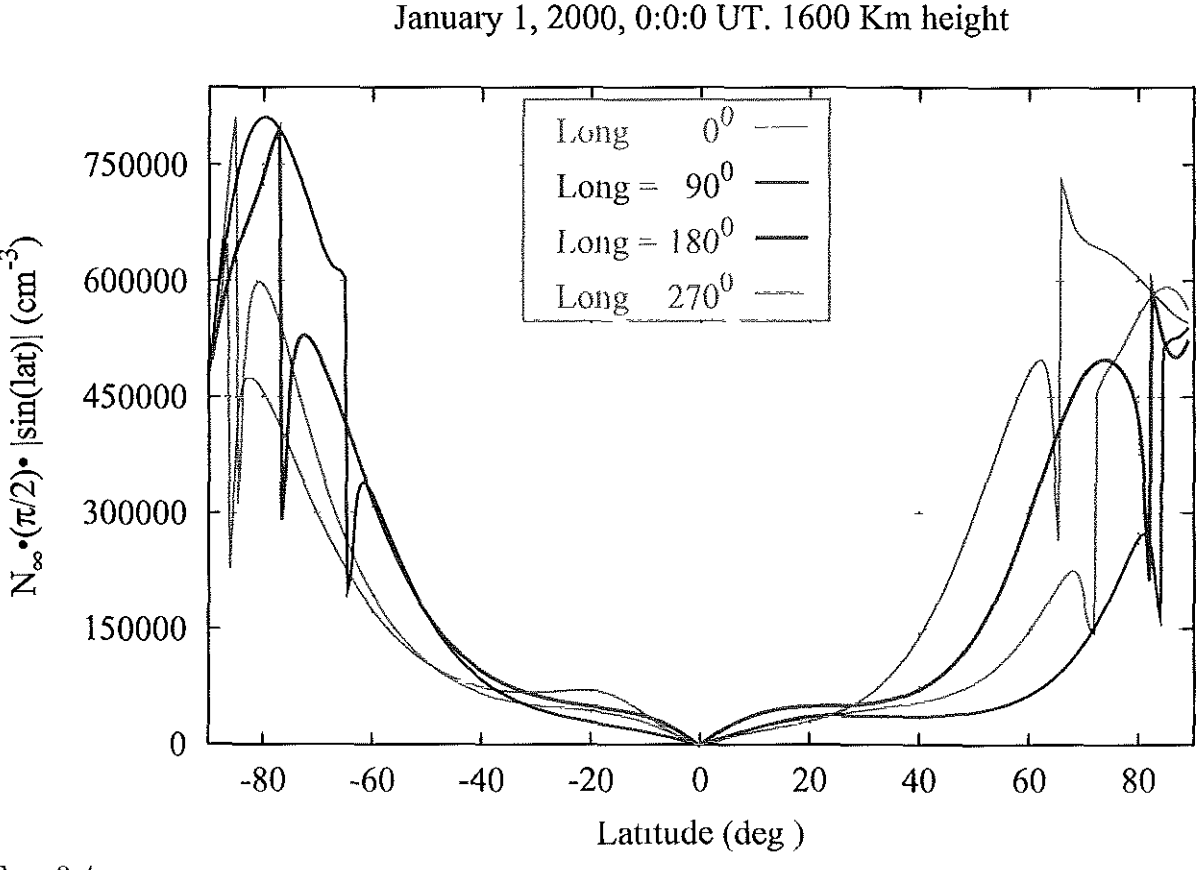
January 1, 2000, 0:0:0 UT. 1600 Km height
750000
600000
450000
300000
150000
0
-80
-60
-40
-20
0
20
40
60
80
Latitude (deg)
$N_\infty \cdot(\pi/2)\cdot |\sin(lat)|$ (cm^{-3})
Long 0^0
Long = 90^0
Long = 180^0
Long 270^0

Fig 3 4

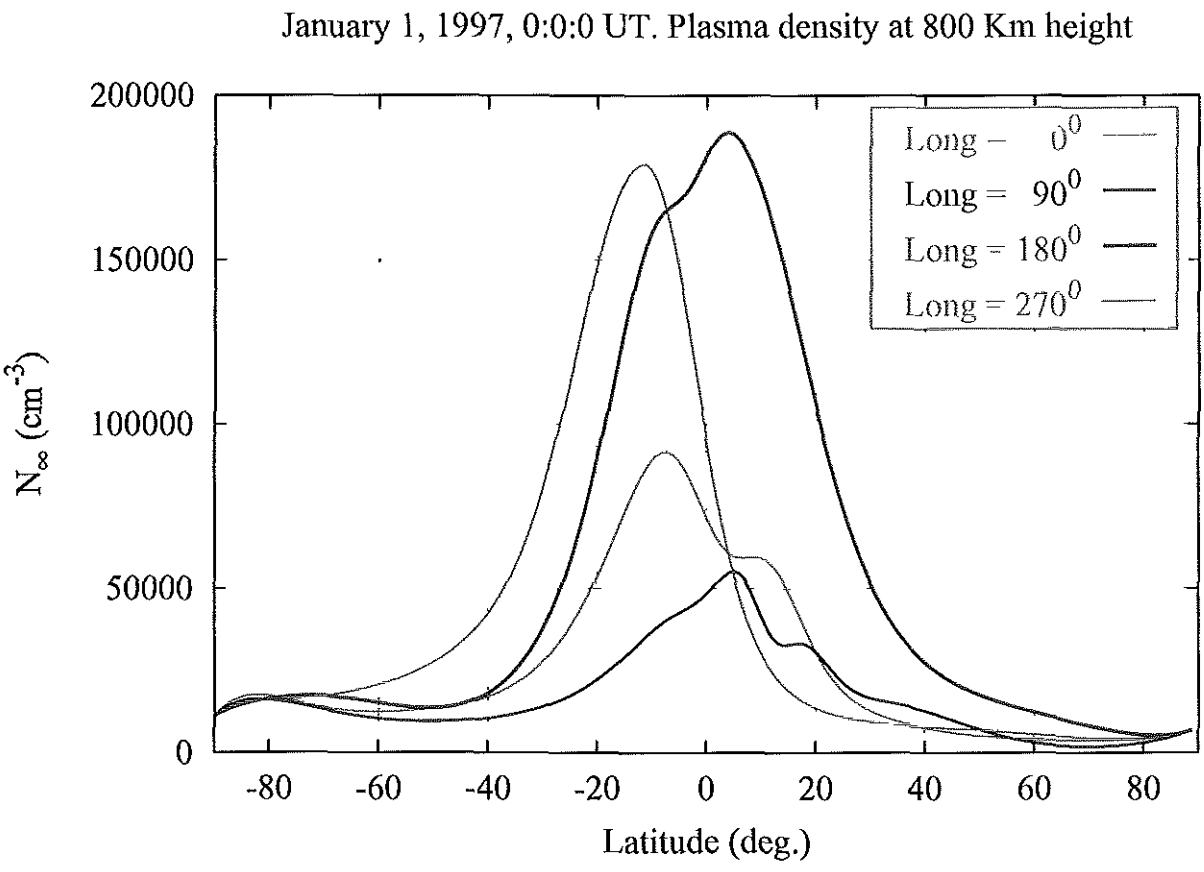
January 1, 1997, 0:0:0 UT. Plasma density at 800 Km height
200000
150000
100000
50000
0
N_∞ (cm^{-3})
-80
-60
-40
-20
0
20
40
60
80
Latitude (deg.)
Long = 0^0
Long = 90^0
Long = 180^0
Long = 270^0

Fig. 3.5

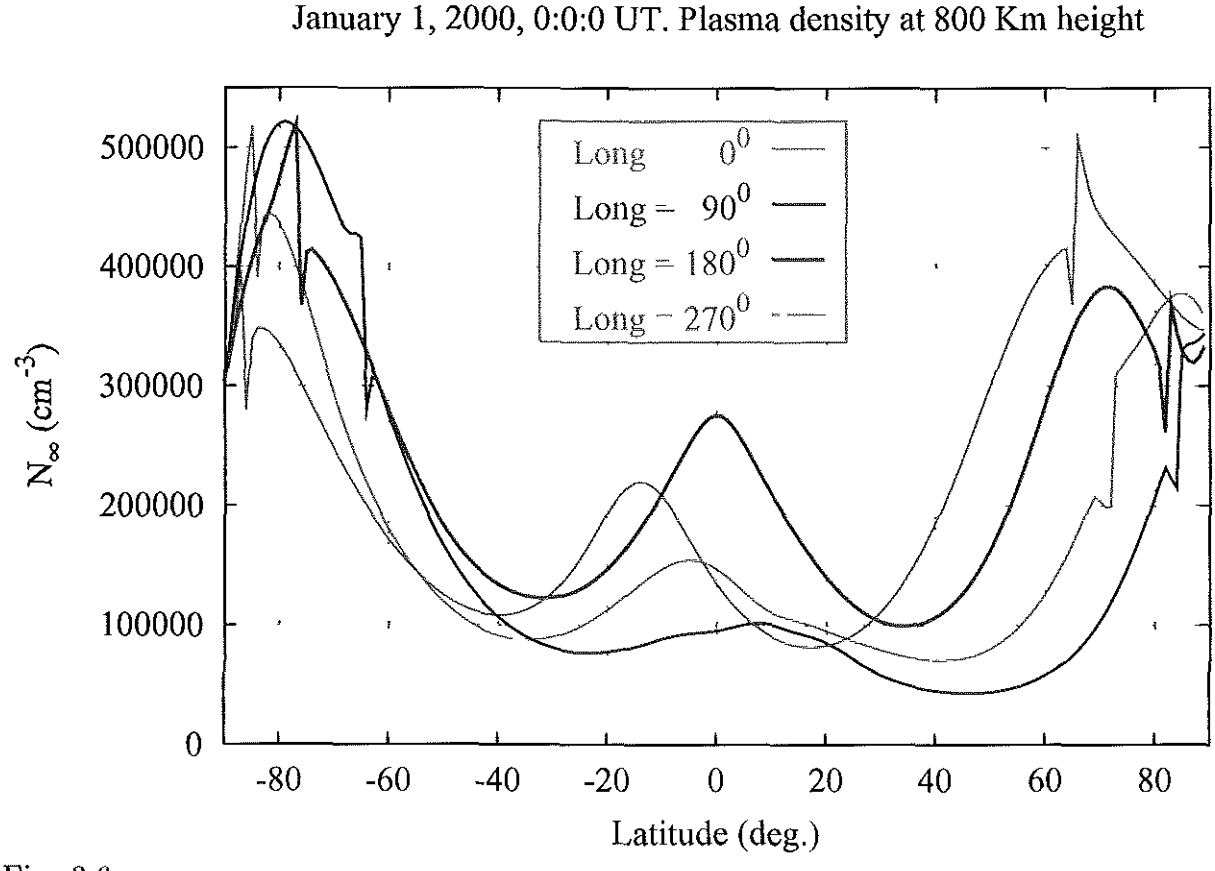
January 1, 2000, 0:0:0 UT. Plasma density at 800 Km height
500000
400000
300000
200000
100000
0
N_∞ (cm^{-3})
-80
-60
-40
-20
0
20
40
60
80
Latitude (deg.)
Long = 0^0
Long = 90^0
Long = 180^0
Long = 270^0

Fig. 3.6

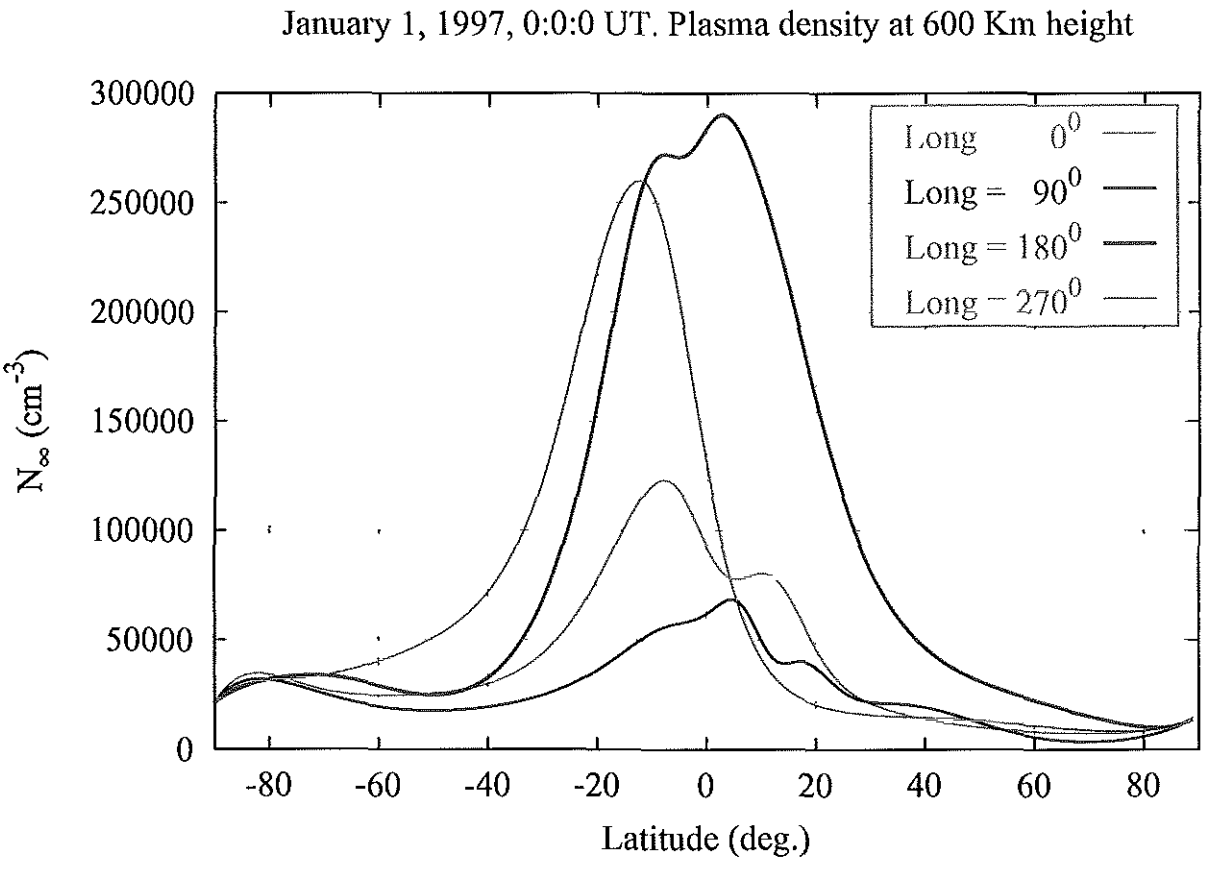
January 1, 1997, 0:0:0 UT. Plasma density at 600 Km height
300000
250000
200000
150000
100000
50000
0
N_e (cm^{-3})
Long 0°
Long = 90°
Long = 180°
Long = 270°
-80
-60
-40
-20
0
20
40
60
80
Latitude (deg.)

Fig. 3.7

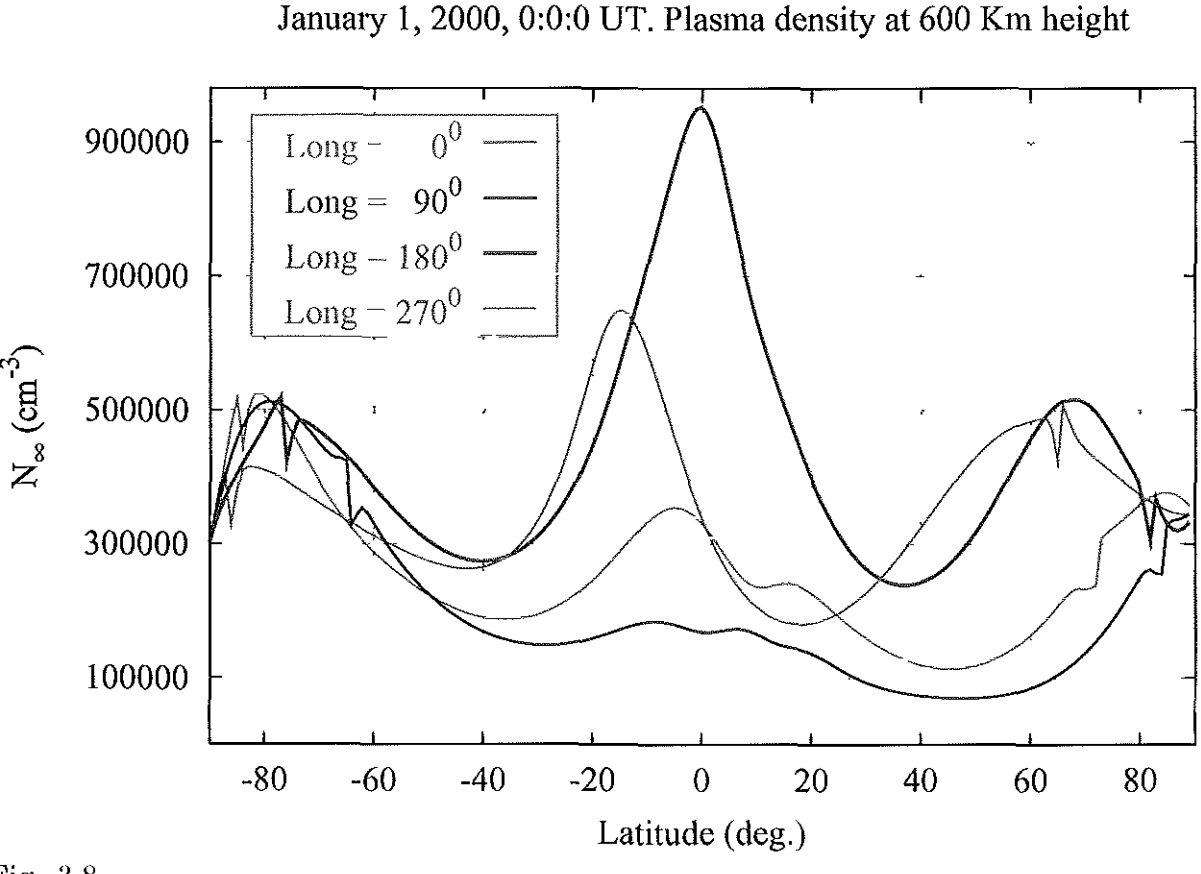
January 1, 2000, 0:0:0 UT. Plasma density at 600 Km height
900000
700000
500000
300000
100000
N_e (cm^{-3})
Long = 0°
Long = 90°
Long = 180°
Long = 270°
-80
-60
-40
-20
0
20
40
60
80
Latitude (deg.)

Fig. 3 8

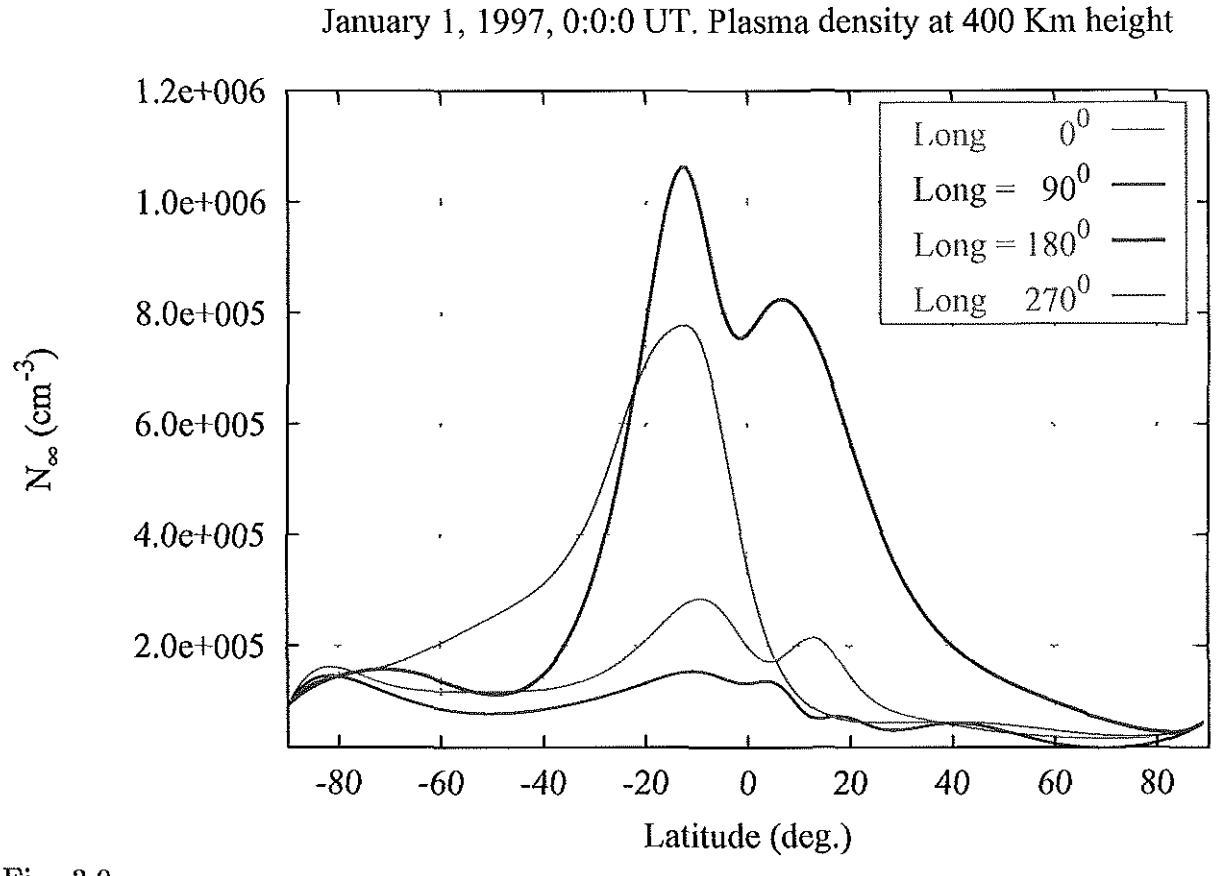

Fig. 3.9

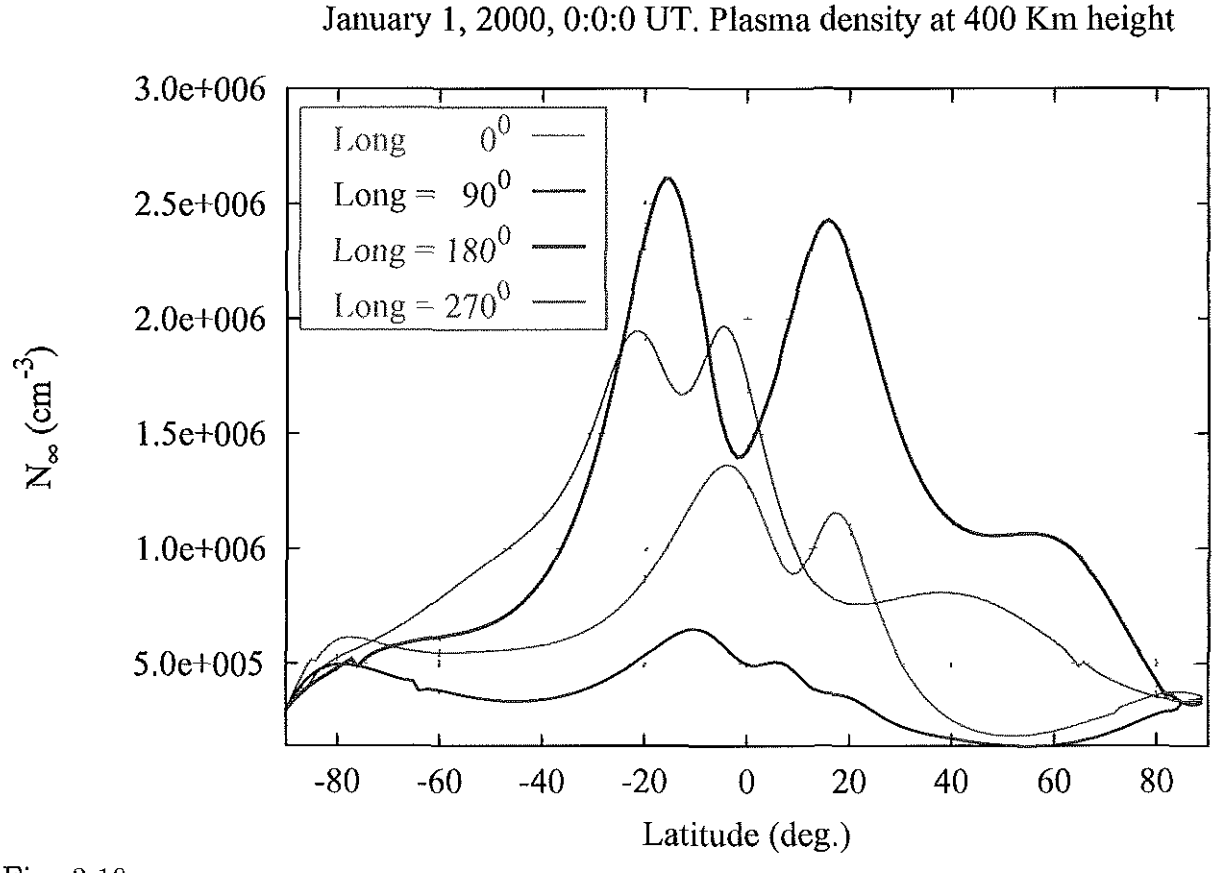

Fig. 3.10

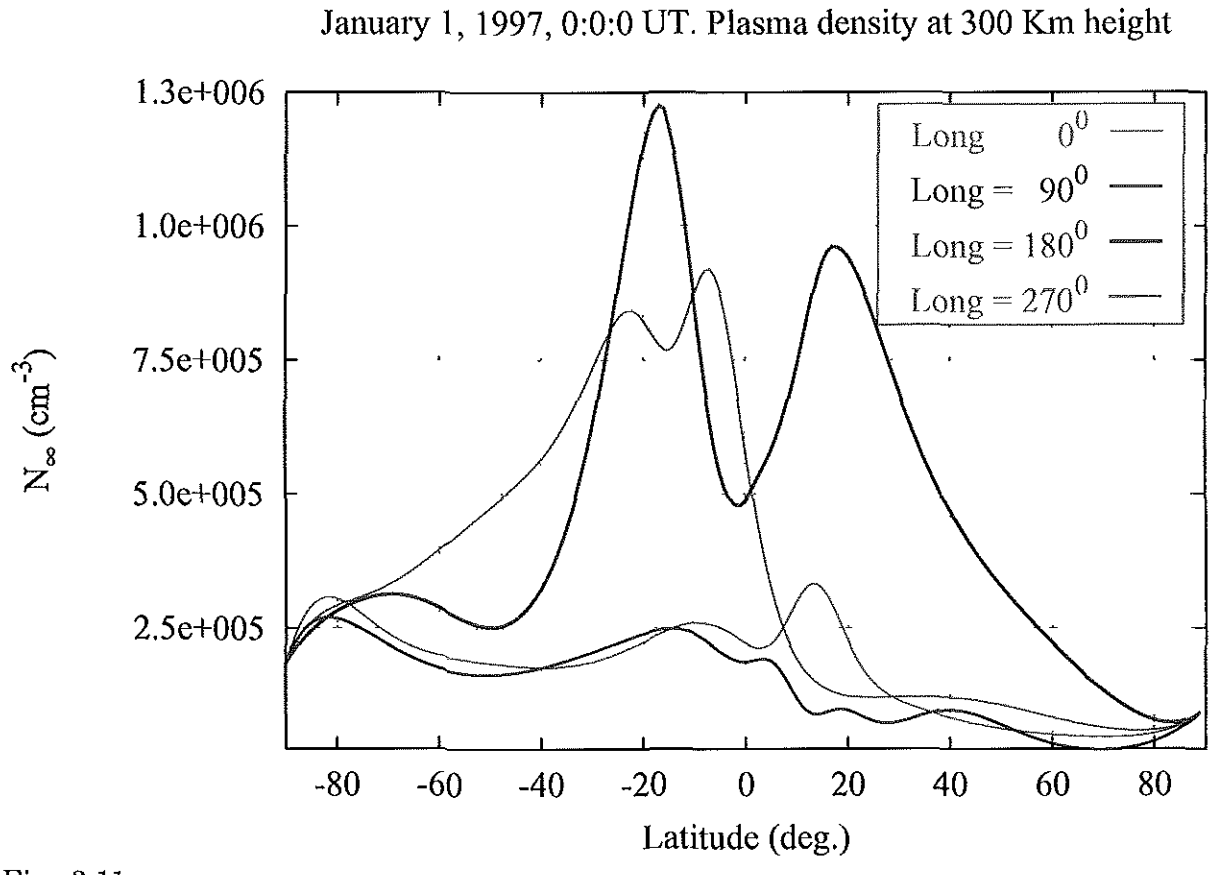

Fig. 3.11

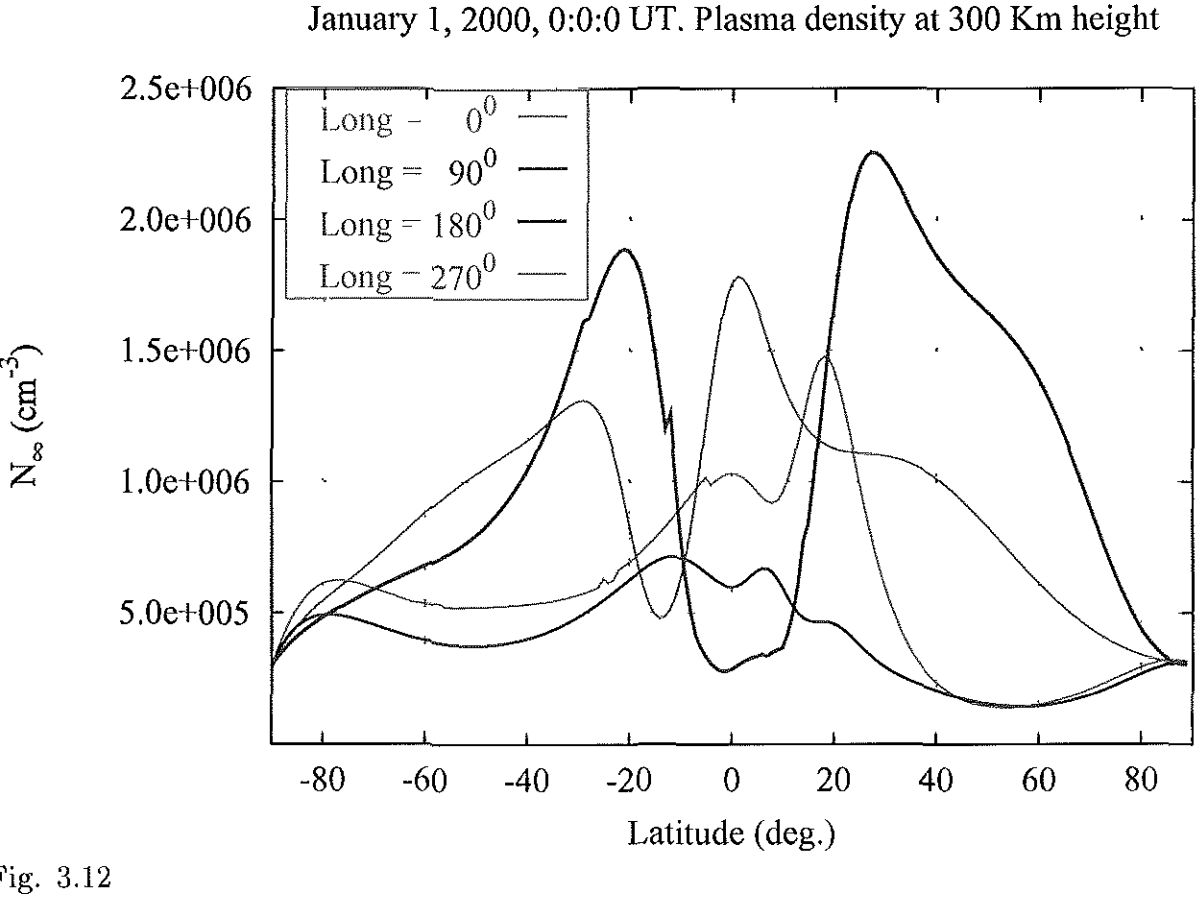

Fig. 3.12

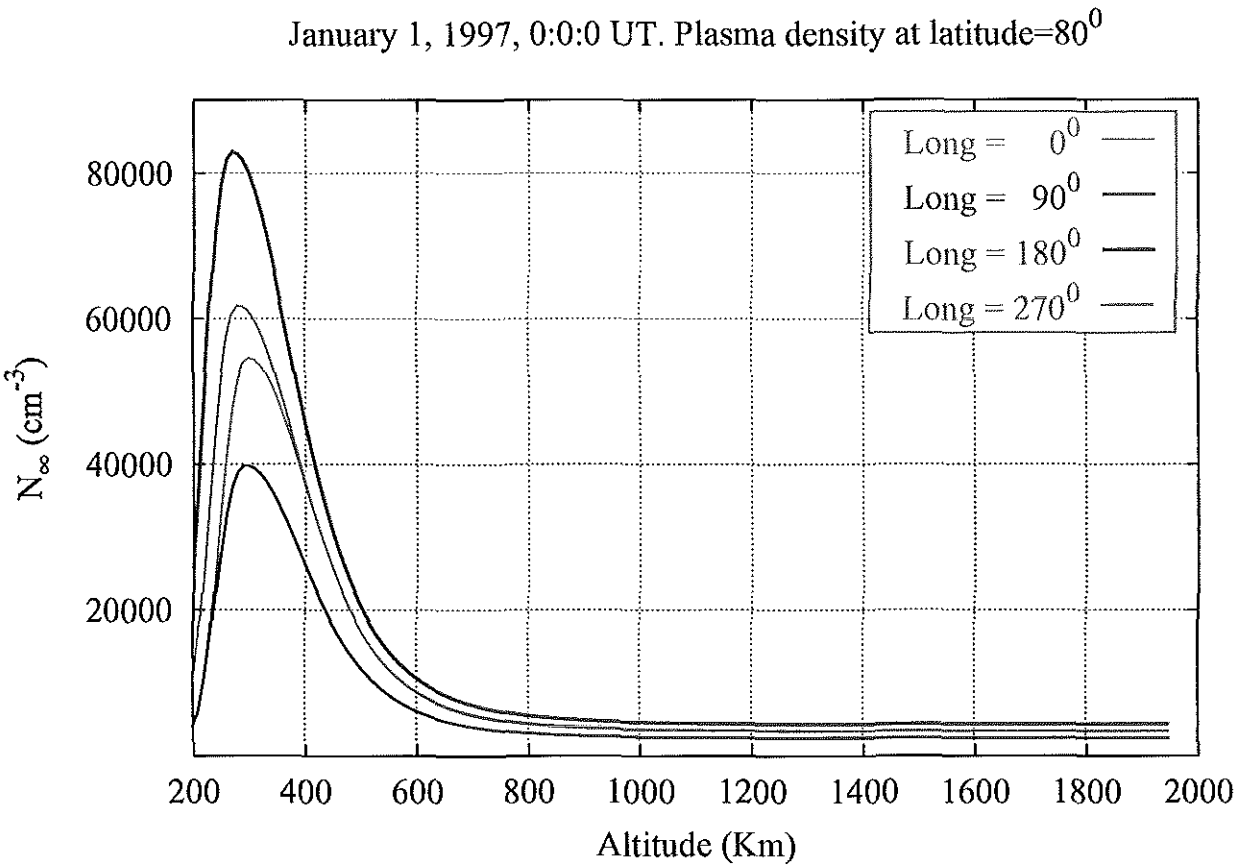

Fig. 3.13

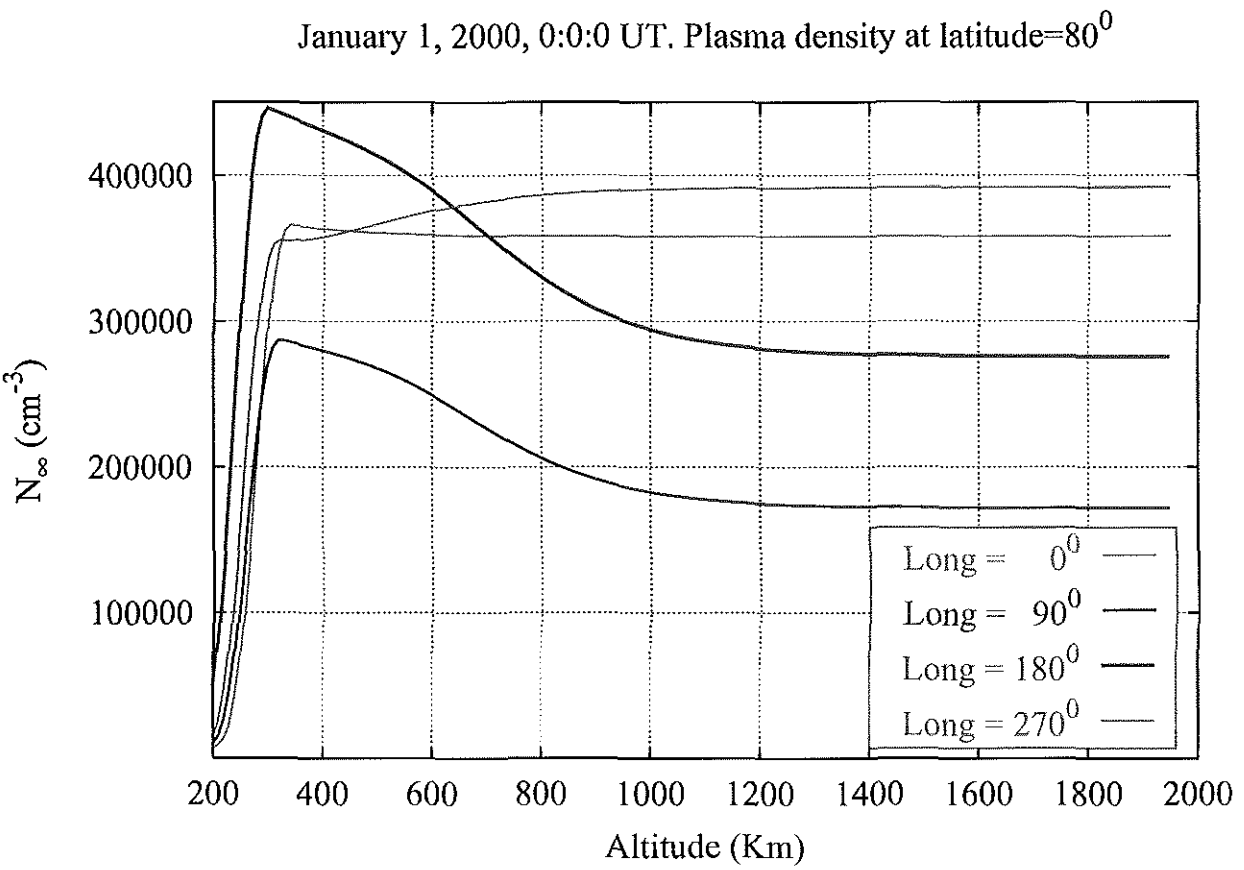

Fig. 3.14

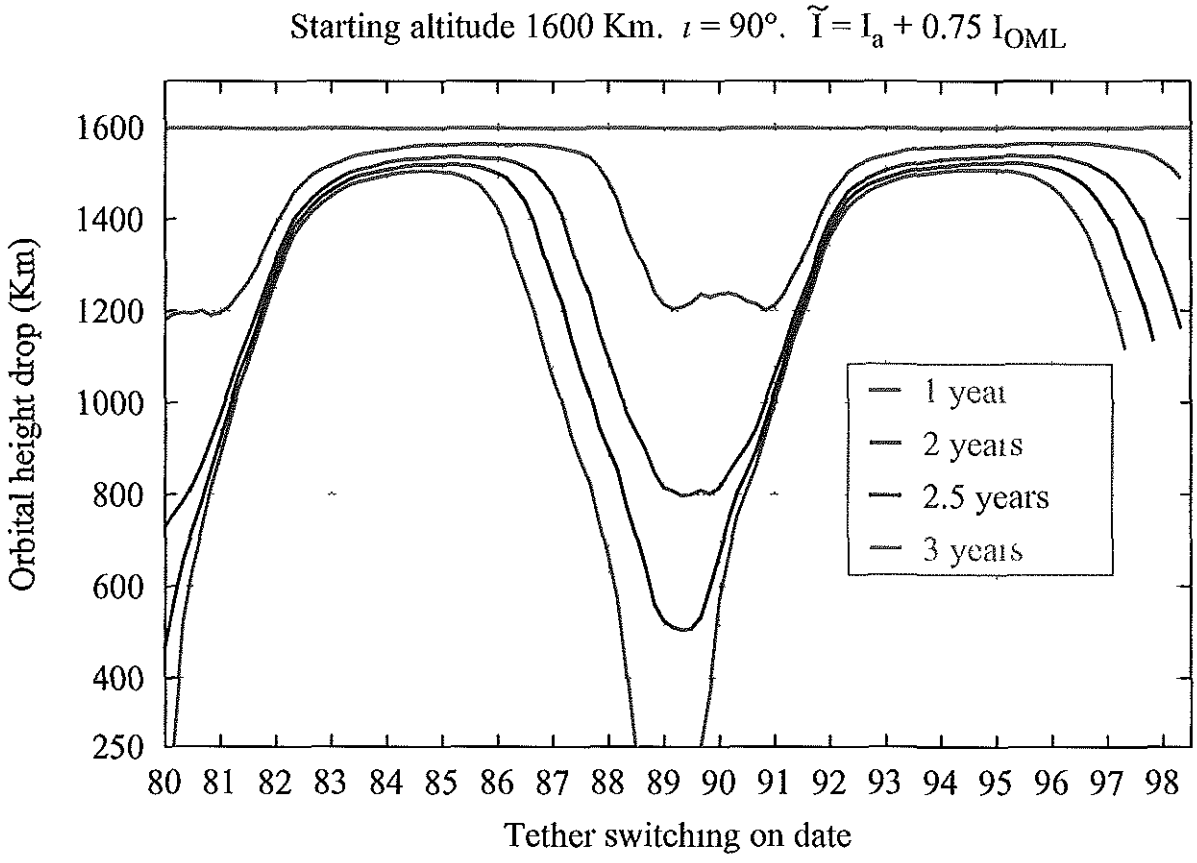

Fig. 3.15

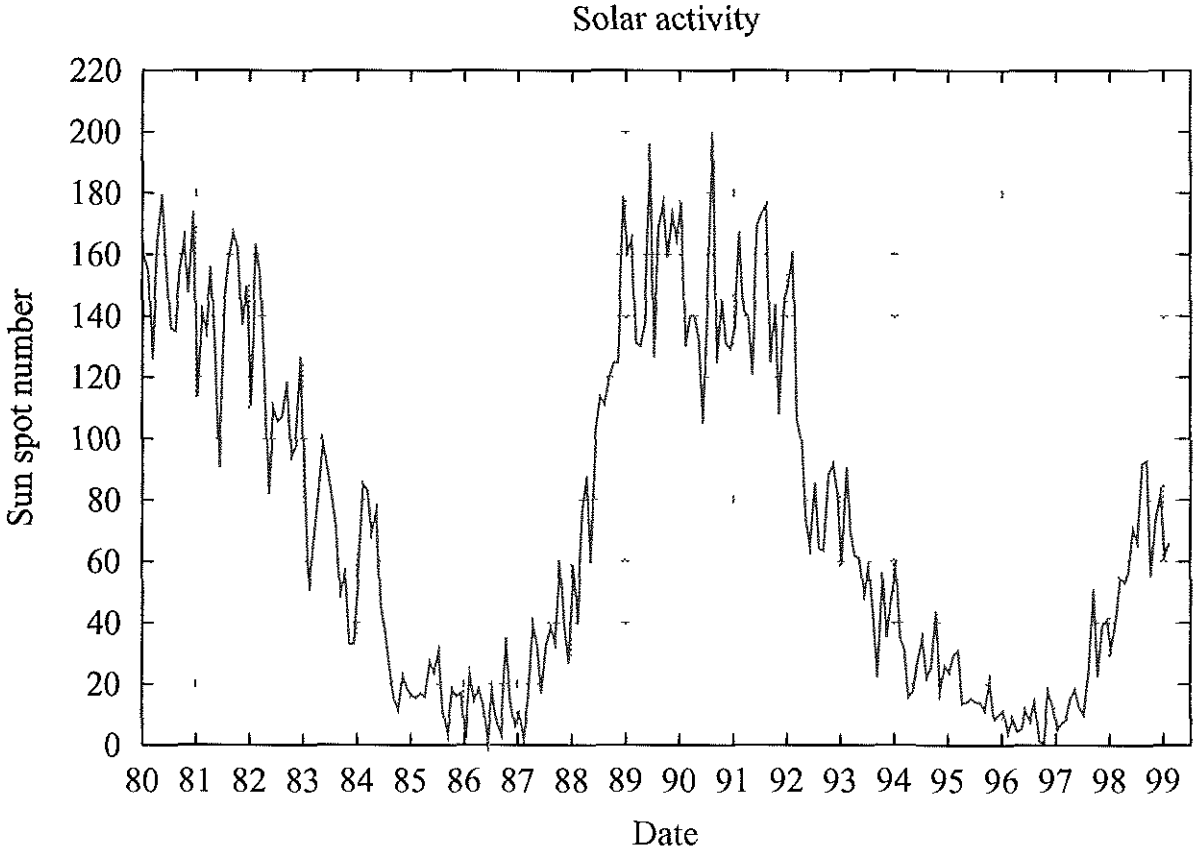

Fig 3.16

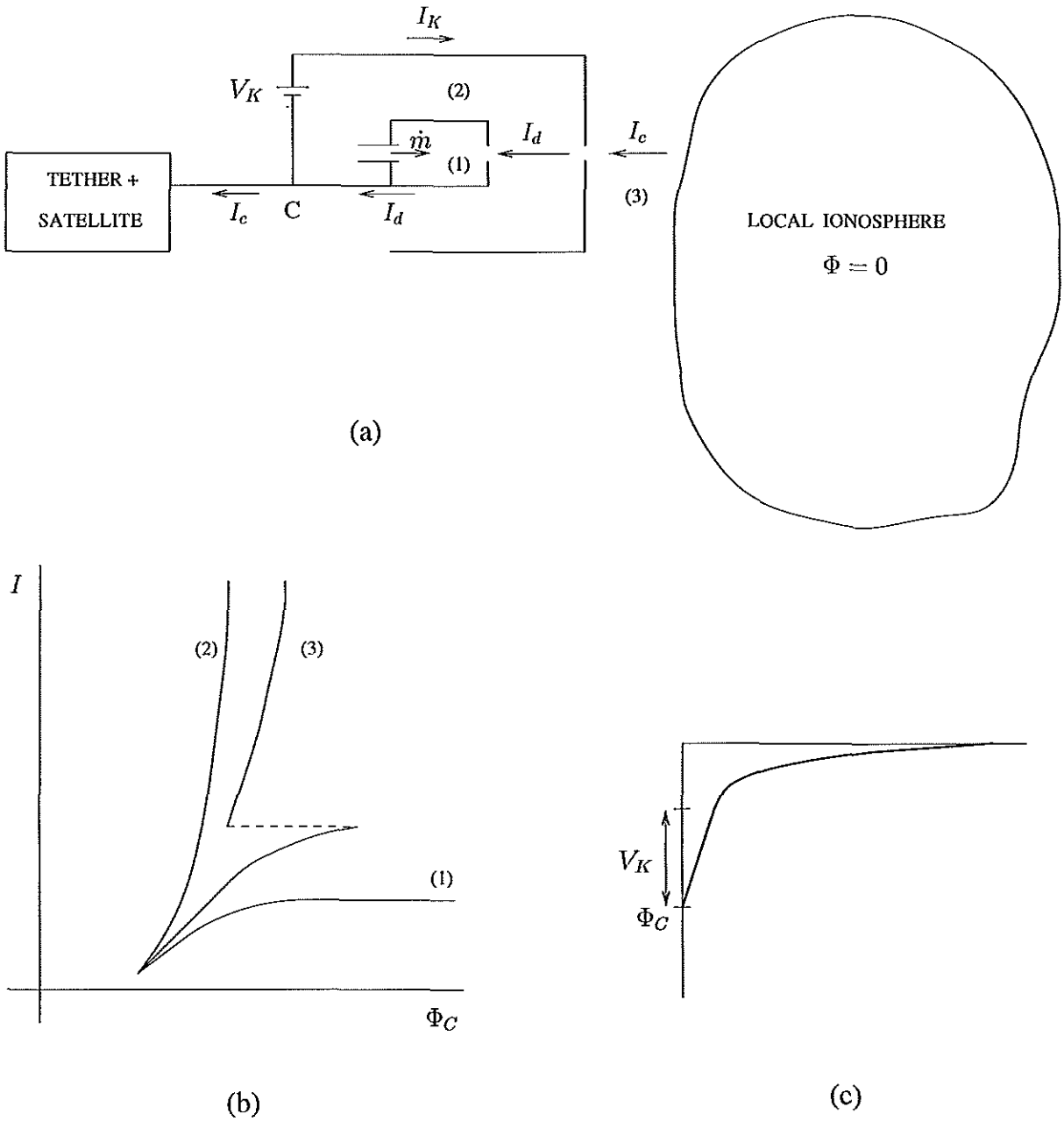

Figure 5.1.- Cathodic contactor. (a) Electrical circuit and the three plasma regions (for an enclosed-keeper design): (1) hollow-cathode, (2) keeper chamber, and (3) ionosphere. (b) C-V response for the (1)plume, (2)spot, and (3)mixed modes. (c) External profile of the electrostatic potential for the spot mode.

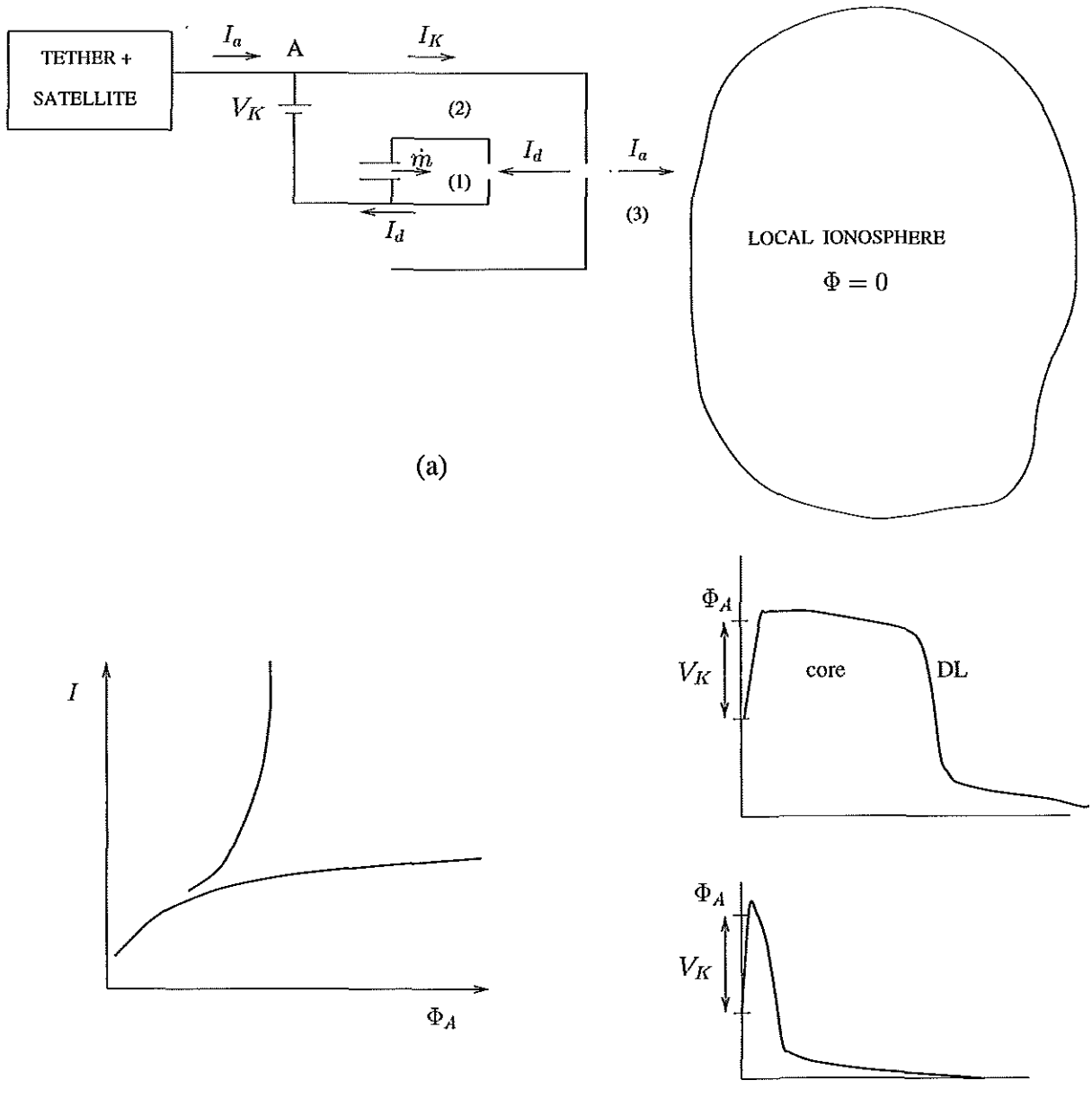

Figure 5.2.- Anodic contactor. (a) Electrical circuit. (b) C-V response for the two operation modes. (c) External profile of the electrostatic potential for the low-impedance mode.

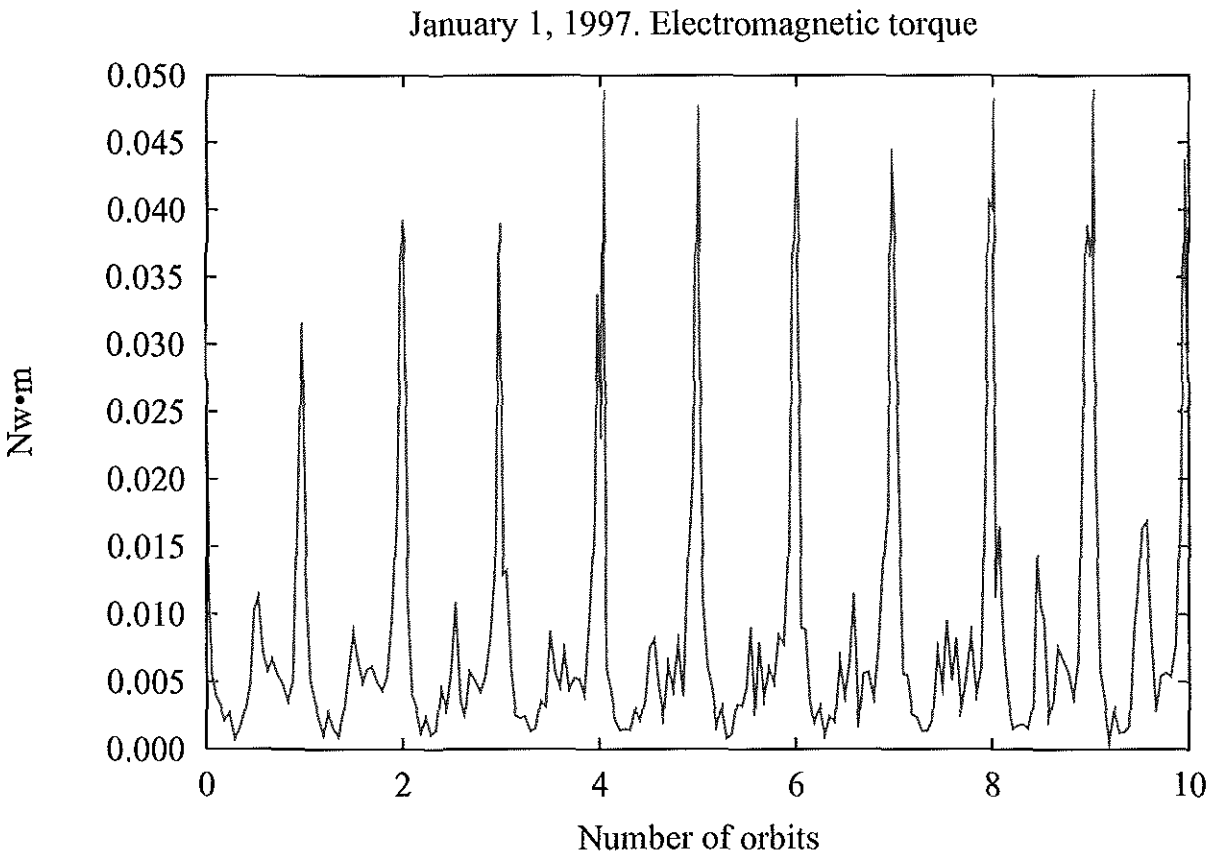
January 1, 1997. Electromagnetic torque
0.050
0.045
0.040
0.035
0.030
0.025
0.020
0.015
0.010
0.005
0.000
Nw•m
0
2
4
6
8
10
Number of orbits

Fig. 7.1

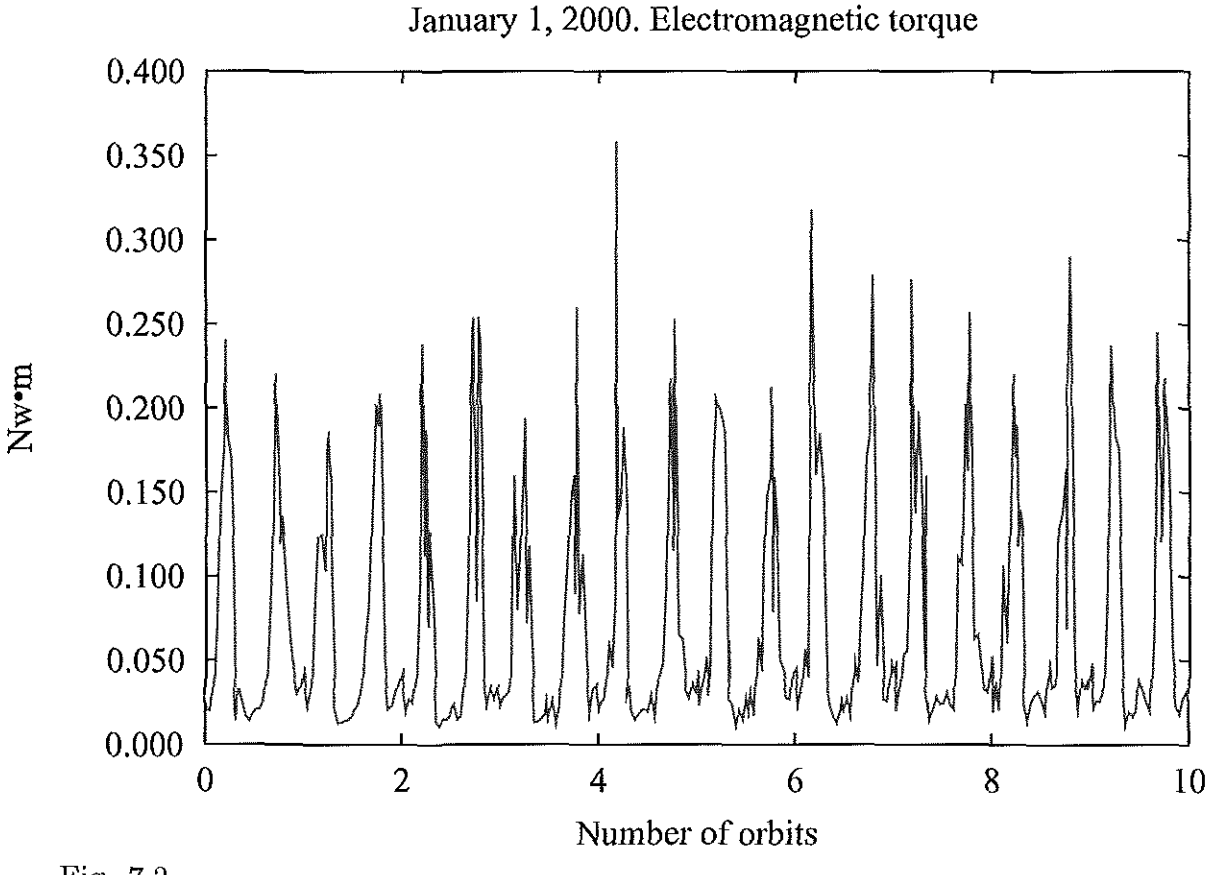
January 1, 2000. Electromagnetic torque
0.400
0.350
0.300
0.250
0.200
0.150
0.100
0.050
0.000
Nw•m
0
2
4
6
8
10
Number of orbits

Fig. 7.2

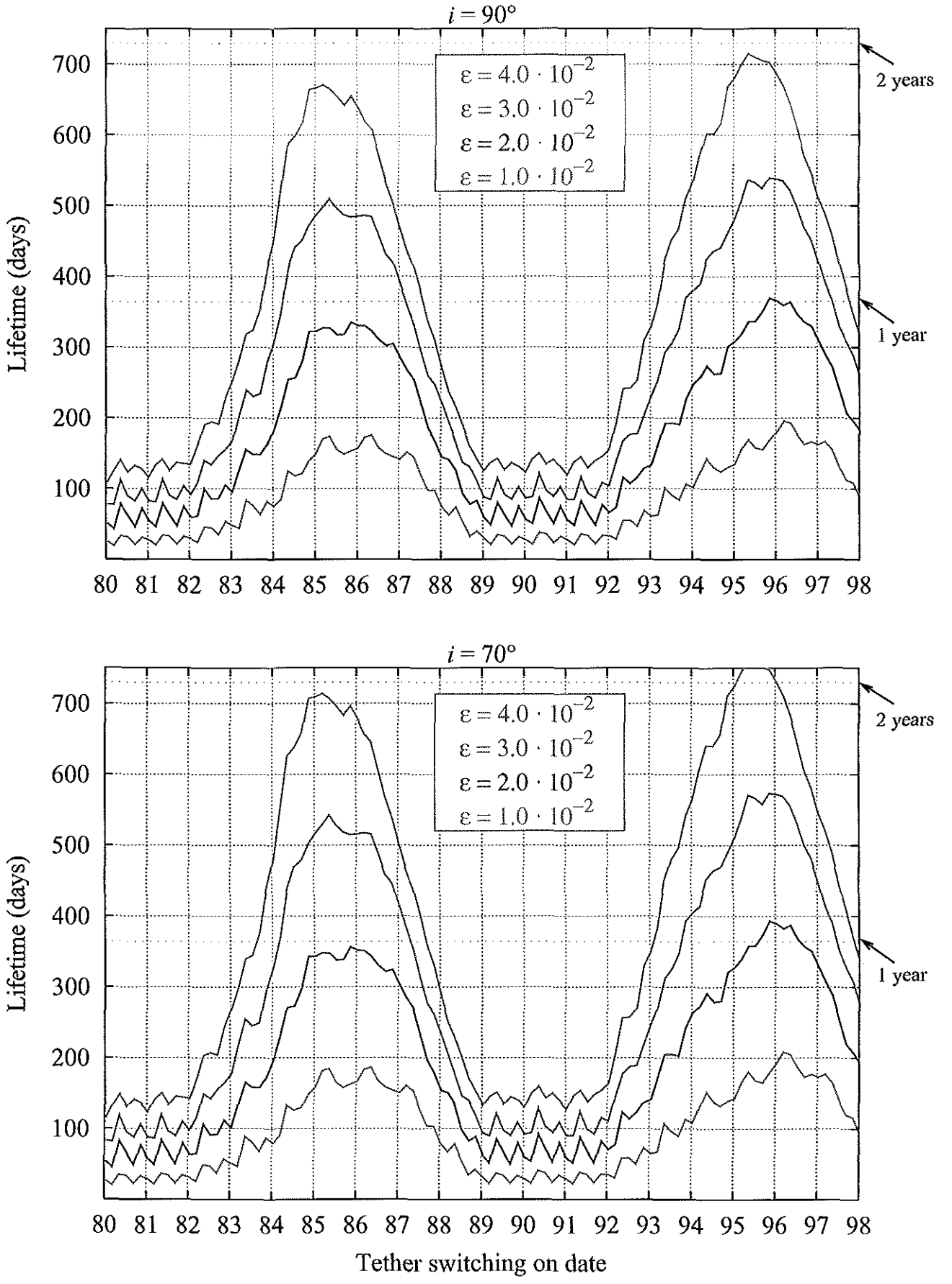

FIG. 9.1 STARTING ALTITUDE 500 KM. LIFETIME (500 → 250 KM)

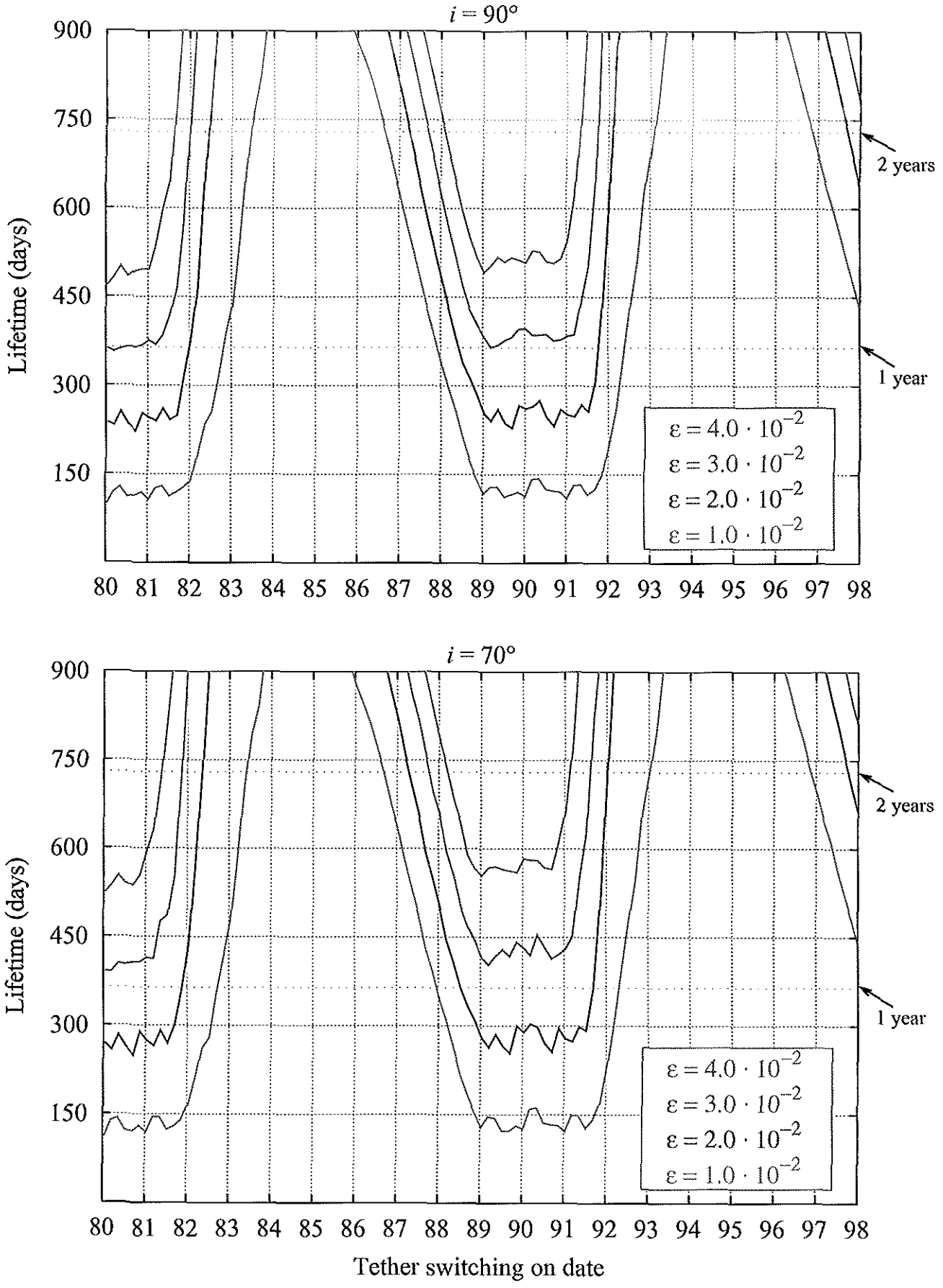

FIG. 9.2 STARTING ALTITUDE 800 KM. LIFETIME (800 → 250 KM)

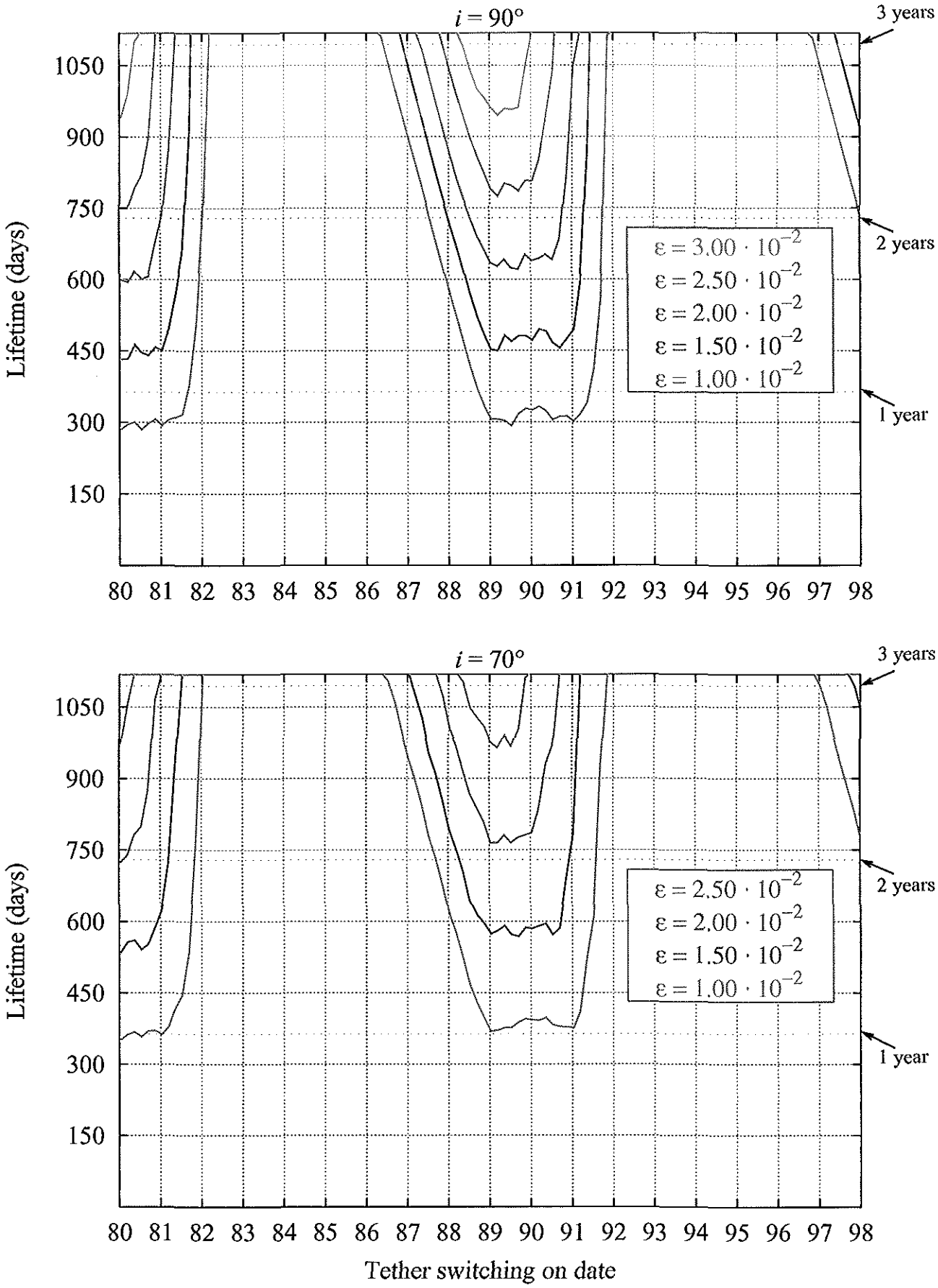

FIG. 9.3 STARTING ALTITUDE 1200 KM. LIFETIME (1200 → 250 KM)

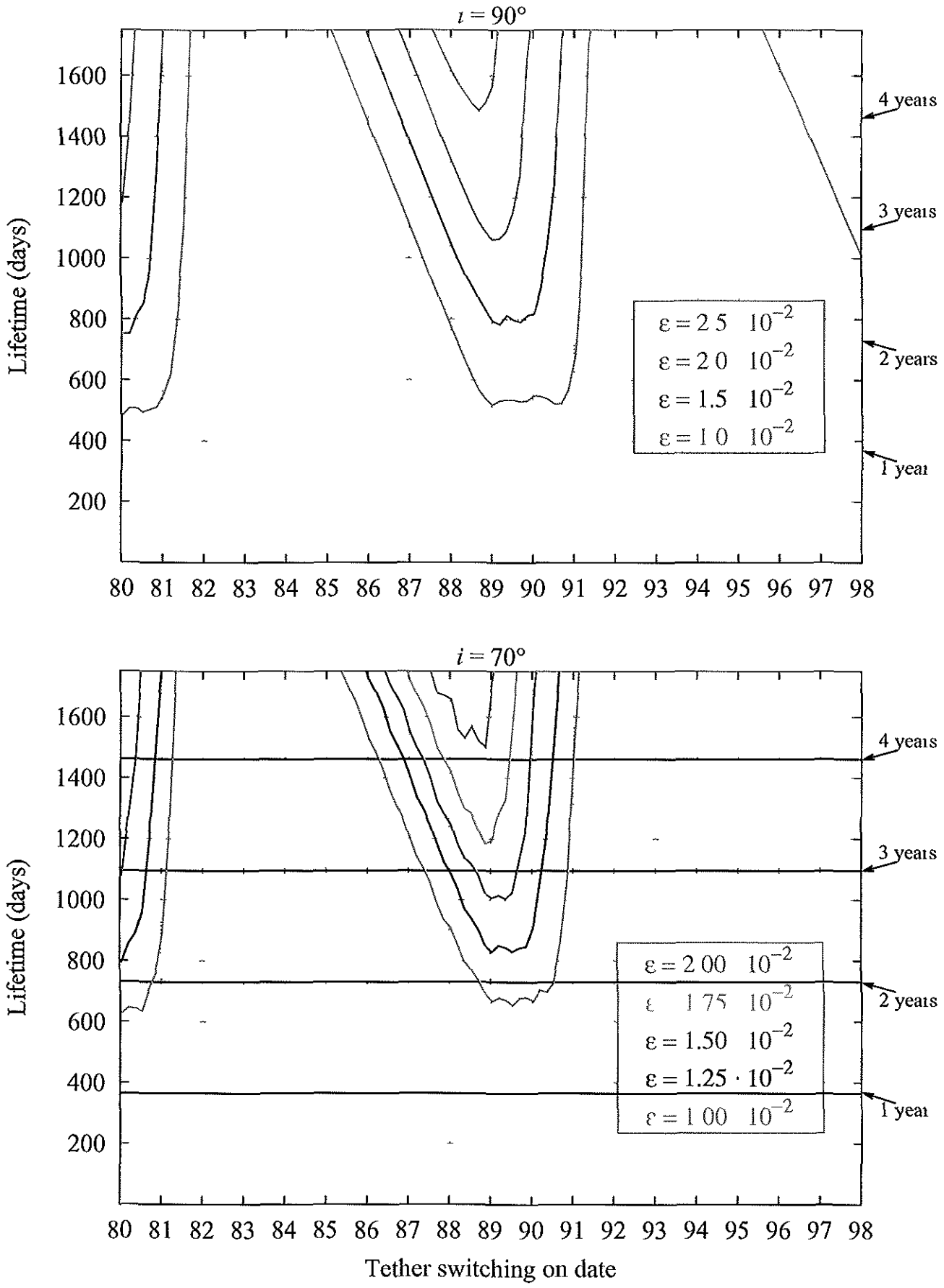

FIG 9.4 STARTING ALTITUDE 1600 KM LIFETIME (1600 → 250 KM)

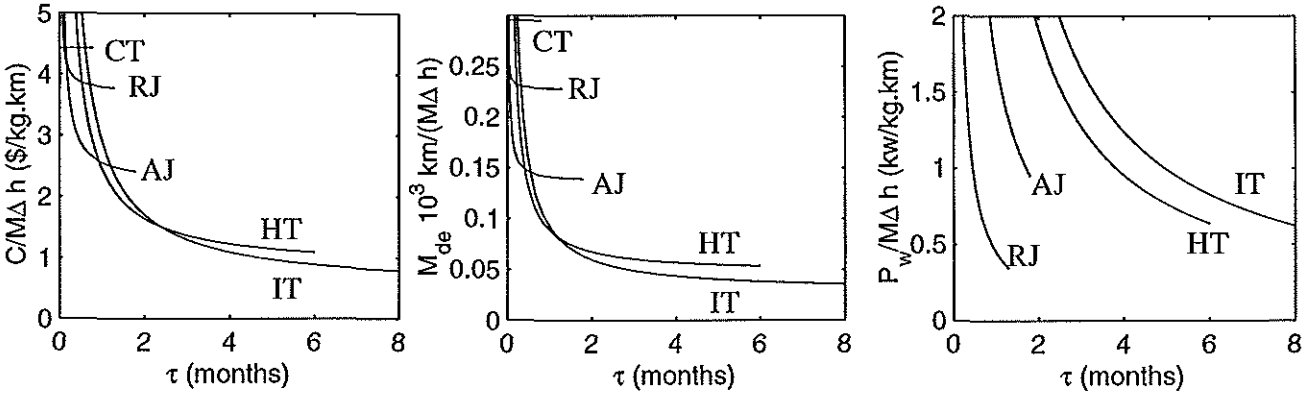

Figure 10.1.- Monetary cost(C), mass of de-orbiting system(M_d), and power requirements(P_w) relative to mission requirements($M\Delta h$), versus de-orbiting time(τ), for different electric thrusters: CT(chemical thruster), RJ(resistojet), AJ(arcjet), HT(Hall thruster), and IT(ion thruster).

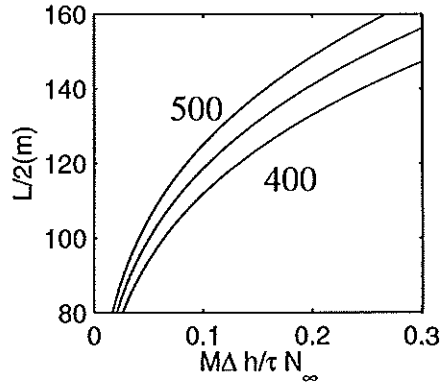

Figure 10.2.- Tether length for different mission conditions, $V_s = 200V$, and $L/2\sqrt{p}(\mathrm{m}^{1/2}) \simeq$ 400, 450 and 500. $M\Delta h$ is in kg.km, τ in months, and N_∞ in cm^{-3}.

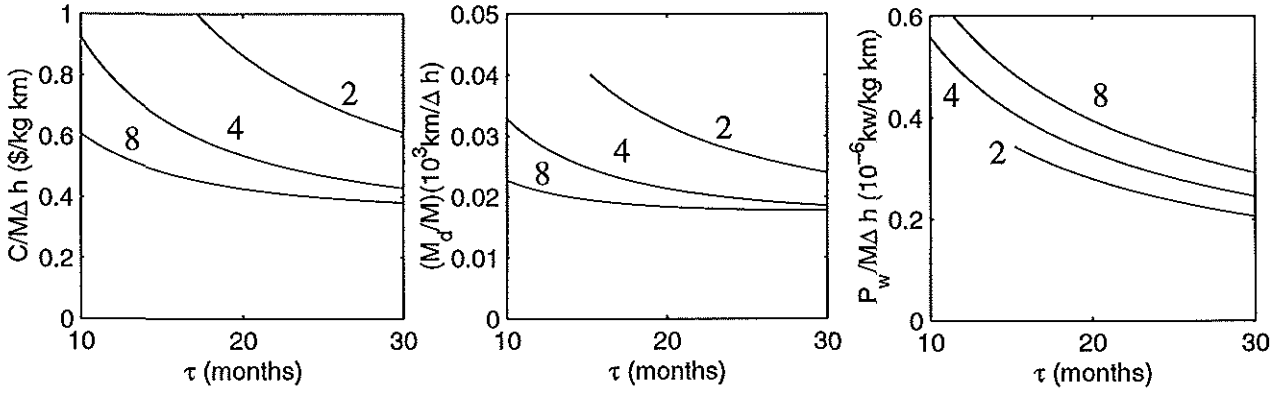

Figure 10.3.- Short-tether system costs versus τ, for three ambient densities: $N_\infty(10^{11}\mathrm{m}^{-3})$ =2,4, and 8; $M\Delta h = 10^6$ kgkm, $V_s = 200V$, and $L/2\sqrt{p} \simeq 450\mathrm{m}^{1/2}$.

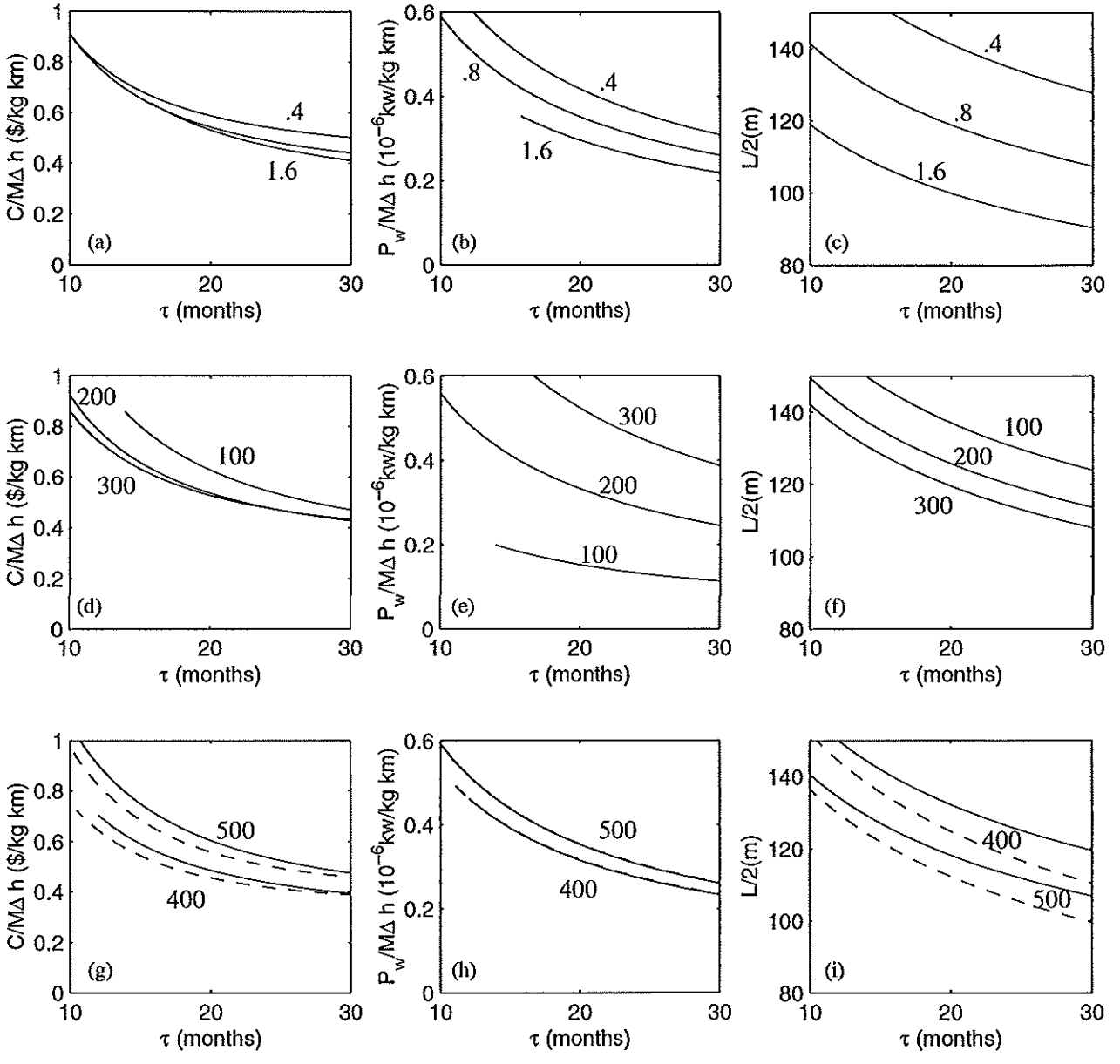

Figure 10.4.- Short-tether system costs versus τ for

(a)-(c) three missions $M\Delta h(10^6\text{kg.km}) = 0.4$, 0.8 and 1.6; $N_\infty = 4 \cdot 10^{11}\text{m}^{-3}$, $V_s = 200\text{V}$.

(d)-(f) three source voltages V_s(V) =100, 200, and 300; $N_\infty = 4 \cdot 10^{11}\text{m}^{-3}$, $M\Delta h = 10^6$ kg.km.

(g)-(i) $L/2\sqrt{p}(\text{m}^{1/2}) = 400$ and 500; $N_\infty = 4 \cdot 10^{11}\text{m}^{-3}$, $M\Delta h = 10^6$ kg.km, $V_s = 200\text{V}$; dashed lines include electron-collection by the anodic contactor with $\mu_M = 1$.

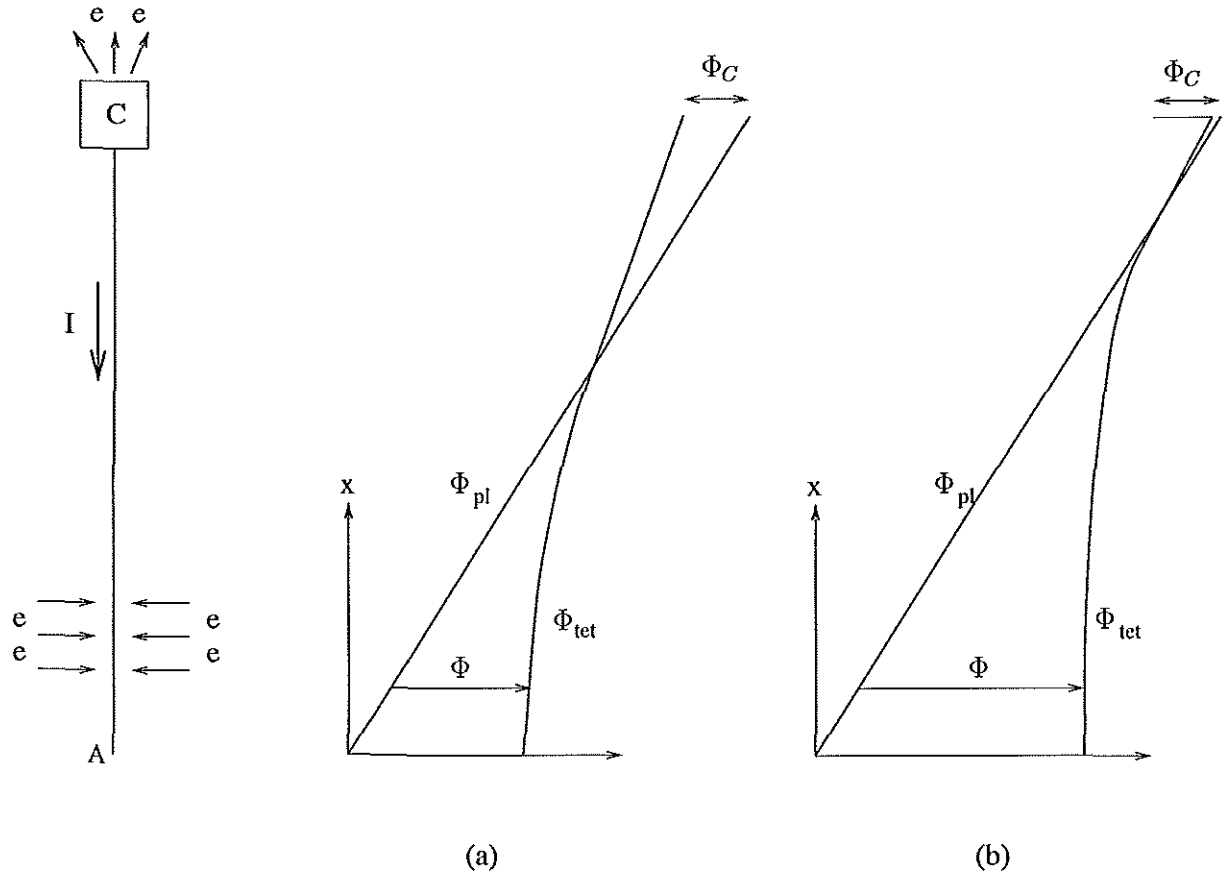

Figure 10.5.- Vertical tether system. Profile of the bias potential between tether and plasma, $\Phi = \Phi_{tet} - \Phi_{pl}$, (a) without and (b) with a voltage source at the electron-emitting contactor(C). The bare tether collects electrons only in the region $\Phi > 0$.

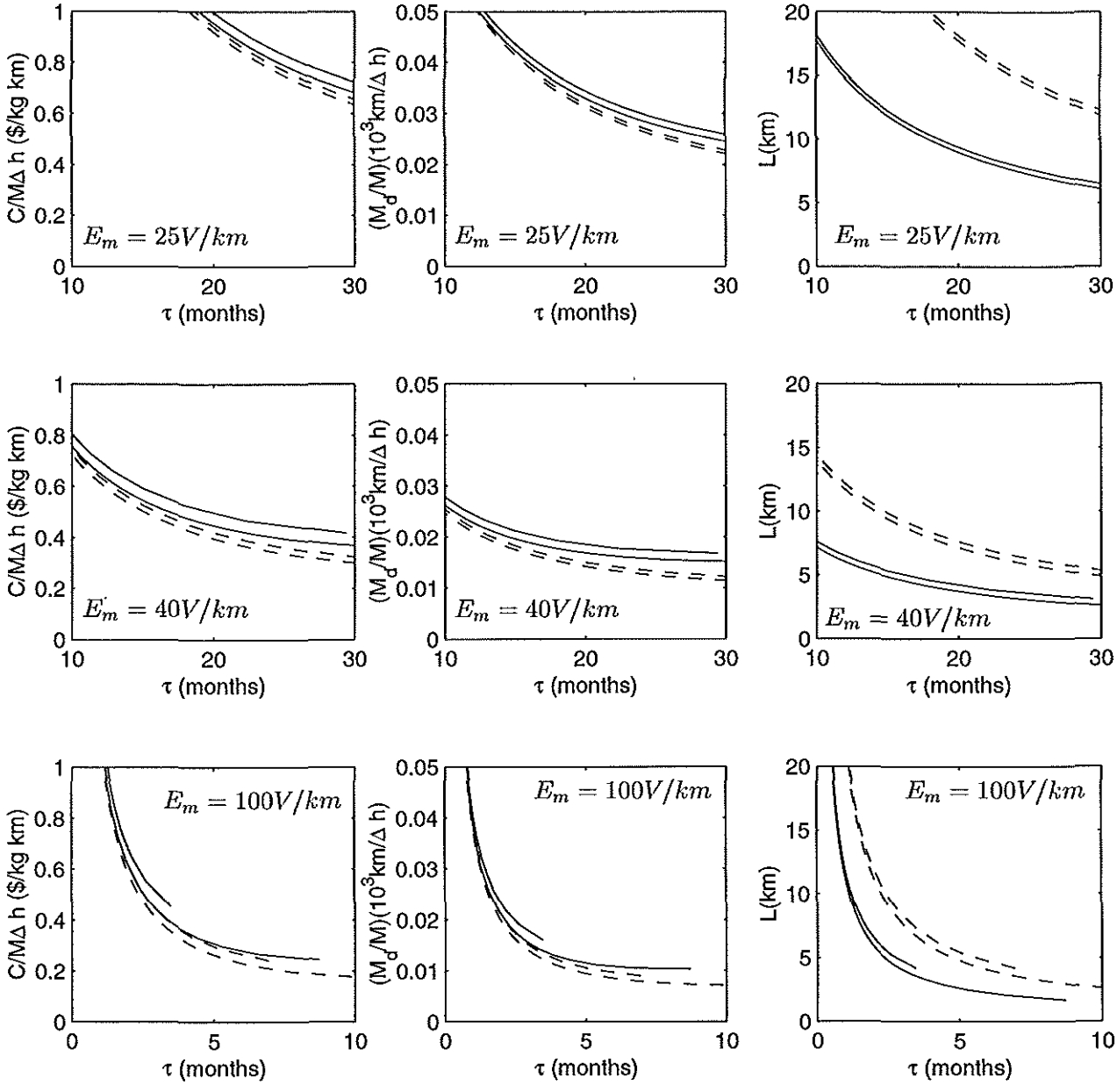

Figure 10.6.- Relative mass and cost of a vertical tether system versus τ, for $M\Delta h(10^6\text{kg.km}) = 0.8$(solid lines) and 1.6(dashed lines), three values of E_m, and two plasma densities: $N_\infty(10^{11}\text{m}^{-3})$ =2(upper lines) and 8 (lower lines). The tether cross-section is a tape 0.5mm thick and 8mm wide.

11. Appendix: Four-Tether Inertially Rotating Satellite

An alternative scenario has been suggested at ESA: four tethers in a plane, at 90° from each other, rotating within that plane for stabilization, and with a single plasma contactor at the satellite. This configuration is briefly analyzed and discarded.

Rigid masts are considered instead. A system with five contactors and zero moment is analyzed first. A simpler system, with only one contactor, is also studied. The complication of the electrodynamic moment only allows numerical analysis. Both have serious flaws.

11.1 Flexible Tethers

The first approach would be to release four tethers at 90° from each other and stabilize them by rotation, as shown in Figure 11.1. Tapes could be used instead of tethers for improved survivability. Centrifugal force would stabilize the system, just as gravity gradient helps stabilize Pro-SEDS.

Beletsky and Levin pointed out that nominally vertical flexible tethers can attain an equilibrium position under gravity gradient and electrodynamic forces [1, 2, 3, 4], as shown in Figure 11.2 (a). However, this configuration is unstable, because coupling between the radial motion and the in-plane libration continuously pumps energy into the system. This is similar to the aerogradient instability studied by several authors [5, 6]. They used a non-tilted dipole geomagnetic model and an equatorial circular orbit: tilt and orbit inclination cause additional oscillations. Studies in connection with the Pro-SEDS program show that there are new instabilities developing as a growing amplitude skip-rope oscillation [7, 8]. Note that this is a relative equilibrium, and that the whole system is being decelerated.

For a rotating tether, however, centrifugal forces are always radial, not parallel to a fixed direction. A relative equilibrium configuration is more difficult to attain: the offset of the tether attachment point is very small compared to the tether length, so that the centrifugal force would have to be much bigger than the electrodynamic force in order to balance moments at the attachment point, as shown in Figure 11.2 (b). Since there is a net moment at the center of mass, the rotation of the system would accelerate.

For a relative equilibrium under steady rotation, the end of the tether should join both masses tangent to the radial direction, and for this it must change its curvature which, under electrodynamic forces, would mean changing the current direction at two points of the tether, as in Figure 11.2 (c). This is not possible.

But this does not address yet the system braking. In relative equilibrium, with either constant or growing angular rate, there is a zero net drag: as each tether rotates, the force changes direction, so that one thether pulls while the opposite one drags. For each tether to produce only drag, the current must be switched off when it begins to accelerate the system. Then, centrifugal force would pull the tether straight, as shown in Figure 11.3 (a). A transverse oscillation of each tether and mass would develop. It seems likely that, at low rotation speeds, oscillation amplitude could grow enough to cause significant winding of the tether about the satellite, while at higher speeds the centrifugal force would avoid winding. Still, the exact evolution cannot be predicted without a detailed study. And meanwhile, rotational speed keeps increasing steadily.

This assumes that rotation is fast enough for the magnetic field not to change over one revolution. Additional perturbations come from the change in the magnetic field over one orbit and over one day.

The continuous increase in rotation speed could be avoided if current direction can be reversed on each tether, so that they always produce drag. This would require additional contactors at the tips. Then, the effect would be again a forced transverse oscillation of each tether and end mass as shown in Figure 11.3 (b). The stability of those oscillations would require a deeper study than is possible here, but preliminary results for Pro-SEDS cited above show important areas of instability that must be avoided. At first sight, a high rotational speed should improve stability, but it has the disadvantages of tether strain and a very fast switching time, that contactors will no be able to provide.

The use of rigid booms could help reduce transverse oscillations. Besides, a simpler model can help clarify the dynamics of the rotation stabilization, which in the case of a flexible tether is somewhat obscured by the complexity of the physical model. Also, the rigid body model can be considered as a first approximation of the flexible tether system.

If the rigid model proves acceptable, a deeper study of the problems caused by flexibility would be required. On the other hand, if the rigid model does not work, the flexible model can be discarded right away.

11.2 Rigid Booms with Zero Electromagnetic Torque

Rigid booms can be used instead, also at 90° from each other, and rotating for centrifugal stabilization.

In order to achieve continuous drag without moment, plasma contactors are needed both at the satellite and at the boom ends. The current will be distributed between both opposing booms so as to achieve zero moment of the electrodynamic forces, as shown in Figure 11.4. This would require five contactors.

As the tether rotates, the drag would turn to push. Contactors and bias should be shifted ever half revolutions to ensure that the electrodynamic force is in the right direction. This puts a limit on the rotation speed, since contactors have a minimum switching time.

Two aspects will be studied: rotational dynamics and centrifugal stresses. If the effect of drag in the orbital elements is neglected, assuming an unperturbed circular orbit, the problem is simple enough for an analytical approach. However, in order to assess the effectiveness of the de-orbit scheme, the evolution of the orbital parameters should be computed. This will be done for the third case, which is complex enough to require numerical analysis.

11.2.1 Motion of a Fast Rotating Satellite in Orbit

The motion and stability of a rotating satellite in orbit has been studied by Beletsky [9]. The simplest case is the symmetric satellite under zero moment (Poinsot). The angular momentum vector $\mathbf{H}_G$ is constant in inertial space, and rotation $\dot{\varphi}$, precession $\dot{\psi}$, and nutation angle θ are constant. Here, θ is defined as the angle between the figure axis and the angular momentum vector.

Let H be the magnitude of the angular momentum, ρ the angle of $\mathbf{H}_G$ with the direction normal to the orbital plane, $\mathbf{n}$, and σ the angle of its projection on the orbital plane with the direction of the pericenter. In orbital axes such that $O\xi$ is directed towards the pericenter and $O\zeta$ is normal to the orbital plane, the angular momentum would be:

$$\mathbf{H}_G = H\,(\sin\rho\cos\sigma, \sin\rho\sin\sigma, \cos\rho) \tag{1}$$

In the Poinsot case, the three are constant, provided the orbital elements do not change with time.

However, when the moment of the gravitational forces is considered, Beletsky obtains equations for the evolution of $\mathbf{H}_G$ through variation of parameters: H, ρ, σ, $\dot{\psi}$, $\dot{\varphi}$, and θ will evolve with time. The derivatives will depend on ψ and orbital anomaly, but these are fast variables and can be averaged, provided the rotation rate is fast enough. Thus the averaged equations give:

$$\frac{dH}{d\tau} = 0; \quad \frac{d\rho}{d\tau} = 0; \quad \frac{d\sigma}{d\tau} = \frac{3\left(I_x - I_z\right)n}{4H\left(1-e^2\right)^{3/2}}\left(3\cos^2\theta - 1\right)\cos\rho \tag{2}$$

where non-dimensional time τ is the mean anomaly, $\tau = nt$, and n is the average orbital rate $\sqrt{\mu/a^3}$. There are two motions now: the fast Poinsot coning about the angular momentum vector, and a slow precession of that vector about the normal to the orbital plane; it is no longer fixed in inertial space, as seen in Figure 11.5, (c).

If the rotation axis is coincides with the orbit normal, we recover the Tomson equilibrium. If it is close to the normal, precession will be small. But if it is near the orbital plane, precession will take it nearly 180° away from the initial position. One way to consider it stable would be to make sure that the precession speed is so slow that the satellite is de-orbited before the axis strays too far.

For the proposed system, in circular orbit, rotating about its symmetry axis at a rate of k times the orbital rate n, with $I_z = 2I_x$—that is, without coning, $H = I_z\omega$, $\theta = 0$—the precession rate would be:

$$\frac{d\sigma}{d\tau} = -\frac{3}{4}\frac{\cos\rho}{k} \tag{3}$$

For the precession period to be just the same as the satellite de-orbiting time (say, one year, or 3000 orbits), the initial rotation should be 2500 $\cos\rho$ times the orbital rate, about 2-3 rad/seg. This is a huge angular speed for a system with 100 m long tethers. And for the axis to drift only a small angle, speeds should be much higher.

Equations (2) and (3) also show that, when the rotation axis is contained in the orbital plane, there is no precession of the angular momentum vector, since $\rho = \pi/2$. This is shown in Figure 11.5 (a).

However, this relative equilibrium is not stable. Any small deviation in orbital inclination or in the angular momentum alignment would result in a small deviation from the right angle, and in a precession that would take the angular momentum nearly 180° from its first position, as shown in Figure 11.5 (b).

Besides, the above considerations only apply to unperturbed Keplerian orbits. When the effect of J_2 is taken into account, the ascending node and the argument of perigee will experience appreciable changes, affecting ρ and σ as well. The obvious effect is that rotations inside the orbital plane are no longer fixed in inertial space. As J_2 forces the ascending node to regress, $\mathbf{n}$ also rotates about the North-South axis, and would no longer be orthogonal to $\mathbf{H}_G$. Angular momentum would start a precession about a *moving* axis.

For exactly polar orbits, the regression of the ascending node is zero. Only in this case would the rotation within the orbital plane remain as a relative equilibrium position. Still, the fact that it is unstable makes it useless without some sort of attitude control.

In all other cases, there will be two attitude motions: Poinsot coning about the angular momentum vector, and precession of the angular momentum about the direction normal to the orbit, which is itself slowly rotating about the North-South axis.

In short, fast rotation cannot stabilize the satellite. There is only one relative equilibrium position, the *exactly* polar orbit with in-plane rotation exactly about the symmetry axis, but it

is unstable: Small changes induce a slow precession that takes the rotation axis away. Still, the faster the rotation, the longer it takes to drift away from the initial direction. But centrifugal stresses must be taken into account as well.

11.2.2 Centrifugal Stresses

A tether of length L and density ρ, rotating at an angular speed ω, experiences a maximum stress at the hub amounting to $\sigma_{max} = \rho\omega^2 L^2/2$. If the breaking stress is σ_*, the tether breaks when the critical angular speed is reached:

$$\omega_* = \frac{1}{L}\sqrt{\frac{2\sigma_*}{\rho}} \tag{4}$$

If a contactor of mass m_c is placed at the tip of a tether of mass m_t, the breaking angular speed is further reduced:

$$\omega_*^t = \frac{1}{L}\sqrt{\frac{\sigma_*}{\rho\left(\frac{1}{2}+\frac{m_c}{m_t}\right)}} \tag{5}$$

The breaking angular speeds for different tether materials are given below, assuming the end mass to be the same as the tether mass, and without any safety factor. The physical properties are taken from [4, 10].

Material	σ_* (MPa)	ρ (g/cm^3)	ω_* (rad/s)	ω_*^t (rad/s)
Cu-Be	1000	8.23	2.46	1.42
Al alloy	600	2.7	3.33	1.94
Steel	2000	7.9	3.55	2.95
Kevlar	2800	1.45	9.82	5.67

These values can already discard the fast rotation as a stabilization method, since the speeds required would break the tether—not to mention the impossibility of switching the current direction every second or so with present day contactors.

11.3 Rigid Booms with Electrodynamic Torque

The case of four rigid masts with one central contactor will be studied. Electrons will be collected along the tether and ejected at the satellite. Thus electric current is always towards the tip, as shown in Figure 11.6. Therefore, only one of each pair of opposing tethers can be on at each time, if the system is to produce drag: the other would push. The side-effect is that since drag is produced only on one side, there is a torque that accelerates rotation.

The expression of the electrodynamic forces and torque is so complex that an analytical solution, even approximate, does not exist. Only numerical analysis is feasible.

In order to obtain a best-case scenario, a very light satellite (100 kg) will be considered. Since a high inertia moment will increase stability, the inertia tensor will be computed with contactors at the tips as well, although they will not be activated.

The equations for the evolution of the orbital elements will be formulated, although assuming always a circular orbit. This will allow the de-orbiting speed to be assessed. The equations for attitude evolution will be deduced as well, and the external forces and moments computed.

The numerical computation will be done for different ranges of parameters: orbital inclination, initial rotation speed, direction of the initial rotation inside and outside of the orbital plane, and high and low Solar activity.

11.3.1 Reference Frames

The following reference frames will be used:

S_i	$Ex_iy_iz_i$	"Inertial" frame with origin at the center of the Earth, Ex_i towards the Aries point, Ez_i towards the North Pole.
S_1	$Gx_1y_1z_1$	Orbital-inertial frame with origin at the center of mass of the satellite and axes parallel to S_i (Figure 11.7).
S_2	$Gx_2y_2z_2$	Body axes: central and principal inertia axes of the satellite, with two tethers along Gx_2 and $-Gx_2$ and another two along Gy_2 and $-Gy_2$ (Figure 11.8).
S_0	$Gx_0y_0z_0$	Stroboscopic axes, intermediate between orbital-inertial and body axes.
S_3	$Er\theta z$	Cylindrical orbital axes: $\mathbf{u}_r$ along the local vertical, $\mathbf{u}_\theta$ within the orbital plane towards growing anomaly, and $\mathbf{u}_z$ normal to the orbital plane. Since the orbit is circular, orbital speed will always be along $\mathbf{u}_\theta = \mathbf{u}_v$.
S_4	$Er\Theta\varphi$	Unit vectors of the spherical coordinates related to the inertial frame.
S_E	$Ex_Ey_Ez_E$	Earth-bound frame such that Ez_E is parallel to Ez_i and Ex_Ez_E contains the axis of the magnetic dipole.

11.3.2 Equations for the Orbital Elements

If the orbit is assumed to be nearly circular, the orbital elements are reduced to the longitude of the ascending node Ω, inclination i, and semiaxis or radius a. Anomaly θ must be measured from the ascending node. Neither argument of perigee nor time of perigee passage are defined. Instead, the time of passage by ascending node could be used, or the initial anomaly θ_0 at the initial time. The orbital rate, n, is $\sqrt{\mu/a^3}$. The anomaly is given by:

$$d\theta = n\,dt = \sqrt{\mu/a^3}dt \tag{6}$$

Assuming that the perturbation acceleration in inertial axes is $\mathbf{a}_p = [a_x, a_y, a_z]$, the following planetary equations are deduced:

$$\frac{d\Omega}{dt} = \sin\theta\,(\mathbf{u}_z \cdot \mathbf{a}_p)\,/an\sin i \tag{7}$$

$$\frac{di}{dt} = \cos\theta\,(\mathbf{u}_z \cdot \mathbf{a}_p)\,/an \tag{8}$$

$$\frac{da}{dt} = 2\,(\mathbf{u}_\theta \cdot \mathbf{a}_p)\,/n \tag{9}$$

$$\frac{d\theta_0}{dt} = \{3\,(t-t_0)\;(\mathbf{a}_p \cdot \mathbf{u}_v) - \mathbf{a}_p \cdot [2\mathbf{u}_r - (\mathbf{u}_r \cdot \mathbf{u}_3)\;\mathbf{u}_3]\,/n\}\,/a \tag{10}$$

where $\mathbf{u}_3 = \mathbf{k}_1 \wedge \mathbf{u}_{AN}$ is normal to the line of nodes. The equation for θ_0 need not be used if equation (6) is integrated along with the other 3, instead of using the Kepler equation to find θ.

11.3.3 Euler Angles

Attitude will be studied relative to the orbital-inertial frame. Euler Angles will be used in a 1-2-3 sequence, such that ϕ_1 is the angle rotated about Gx_1, ϕ_2 the angle rotated about the

intermediate Gy_0 axis, and ϕ_3 the angle rotated about the body revolution axis, Gz_2. Their associated rotation matrices will be A_1, A_2, and A_3. It is not easy to relate these angles to pitch, roll, and yaw, since the orbital-inertial axes are different from the typical orbital axes.

Rotations ϕ_1 and ϕ_2 lead from the orbital-inertial to the stroboscopic axes, so that their rotation matrix is $\mathsf{C} = \mathsf{A}_1 \cdot \mathsf{A}_2$; rotation ϕ_3 finally leads to the body axes, whose rotation matrix is $\mathsf{A} = \mathsf{C} \cdot \mathsf{A}_3 = \mathsf{A}_1 \cdot \mathsf{A}_2 \cdot \mathsf{A}_3$. The components of a vector in both frames will be related as:

$$\begin{Bmatrix} x_2 \\ y_2 \\ z_2 \end{Bmatrix} = \mathsf{A}^\mathsf{T} \begin{Bmatrix} x_1 \\ y_1 \\ z_1 \end{Bmatrix}$$

11.3.4 Attitude Dynamics

Angular Speed

Angular speed about the orbital-inertial frame can be computed through matrix derivation, $[\boldsymbol{\omega}_{21}]^\times = \mathsf{A}^\mathsf{T} \cdot \dot{\mathsf{A}}$, or through vector projection in body axes:

$$\boldsymbol{\omega}_{21} = \begin{Bmatrix} p \\ q \\ r \end{Bmatrix} = \begin{Bmatrix} \dot{\phi}_2 \sin\phi_3 + \dot{\phi}_1 \cos\phi_2 \cos\phi_3 \\ \dot{\phi}_2 \cos\phi_3 - \dot{\phi}_1 \cos\phi_2 \sin\phi_3 \\ \dot{\phi}_3 + \dot{\phi}_1 \sin\phi_2 \end{Bmatrix} \tag{11}$$

or in stroboscopic axes:

$$\boldsymbol{\omega}_{21} = \begin{Bmatrix} \dot{\phi}_1 \cos\phi_2 \\ \dot{\phi}_2 \\ \dot{\phi}_3 + \dot{\phi}_1 \sin\phi_2 \end{Bmatrix} \tag{12}$$

The angular speed of the stroboscopic axes is the same, except for $\dot{\phi}_3$:

$$\boldsymbol{\omega}_{01} = \boldsymbol{\omega}_{21} - \dot{\phi}_3 \mathrm{k}_3 = \begin{Bmatrix} \dot{\phi}_1 \cos\phi_2 \\ \dot{\phi}_2 \\ \dot{\phi}_1 \sin\phi_2 \end{Bmatrix} \tag{13}$$

Inertia Tensor

The satellite inertia tensor is dominated by the contribution of the four tethers. Let L be each tether's length, m_t their mass, and m_c the mass of the end contactors, and I_i the principal moments of the core satellite. The inertia tensor will be:

$$\mathsf{I}_\mathsf{G} = 2\left(\frac{m_t}{3} + m_c\right) L^2 \begin{bmatrix} 1+\epsilon_1 & 0 & 0 \\ 0 & 1+\epsilon_2 & 0 \\ 0 & 0 & 2+\epsilon_3 \end{bmatrix} \approx I_t \begin{bmatrix} 1 & 0 & 0 \\ 0 & 1 & 0 \\ 0 & 0 & 2 \end{bmatrix} \tag{14}$$

since $\epsilon_i = \frac{I_i}{I_t} \ll 1$.

Taking the case of a light satellite: $L = 100$ m, $m_s = 100$ kg, $m_t = 3.5$ kg, $m_c = 3.5$ kg, leads to: $I_t = 75833$ kg·m^2.

Attitude Motion Equations

The Newton-Euler equations in stroboscopic axes give:

$$\frac{d\vec{H}_G}{dt} = \mathsf{I}_\mathsf{G} \cdot \dot{\boldsymbol{\omega}}_{21} + \boldsymbol{\omega}_{01} \wedge \mathsf{I}_\mathsf{G} \cdot \boldsymbol{\omega}_{21} = \vec{M}_{gi} + \vec{M}_m \tag{15}$$

where $\vec{M}_{gi}$ is the moment of the gravity and inertia forces in G, and $\vec{M}_m$ the moment of the electrodynamic forces.

Since the satellite will be rotating initially about the Gz_2 axis, the variables to be used will be ϕ_1, ϕ_2, and ψ_3 such that $\phi_3 = \omega t + \psi_3$. In these variables, the Euler equations become:

$$I_t \left[\ddot{\phi}_1 \cos \phi 2 + 2\dot{\phi}_2 \left(\omega + \dot{\psi}_3 \right) \right] = M_x \tag{16}$$

$$I_t \left\{ \ddot{\phi}_2 - \dot{\phi}_1 \cos \phi_2 \left[\dot{\phi}_1 \sin \phi_2 + 2 \left(\omega + \dot{\psi}_3 \right) \right] \right\} = M_y \tag{17}$$

$$2I_t \left(\ddot{\psi}_3 + \ddot{\phi}_1 \sin \phi_2 + \dot{\phi}_1 \dot{\phi}_2 \cos \phi_2 \right) = M_z \tag{18}$$

Isolating the highest order derivatives:

$$\ddot{\phi}_1 = \frac{-2\dot{\phi}_2 \left(\omega + \dot{\psi}_3 \right) + M_x / I_t}{\cos \phi_2} = u \tag{19}$$

$$\ddot{\phi}_2 = \dot{\phi}_1 \cos \phi_2 \left[\dot{\phi}_1 \sin \phi_2 + 2 \left(\omega + \dot{\psi}_3 \right) \right] + M_y / I_t \tag{20}$$

$$\ddot{\psi}_3 = -\dot{\phi}_1 \dot{\phi}_2 \cos \phi_2 - u \sin \phi_2 + M_z / 2I_t \tag{21}$$

The equations are highly non-linear. Linearization could be used if there is some law of conservation of angular momentum, i.e., $M_z = 0$. This cannot be said until the moments are computed.

11.3.5 External Forces

Inertia Forces

Inertia forces over a particle P moving about the non-rotating orbital-inertial axes reduce to:

$$\mathbf{F}_i^P = -m_P \boldsymbol{\gamma}_{1i}^P = -m_P \boldsymbol{\gamma}_{1i}^G = -\frac{m_P n^2}{a} \mathbf{u}_r \tag{22}$$

where $\mathbf{u}_r$ is:

$$\mathbf{u}_r = [\cos \Omega \cos \theta - \sin \Omega \sin \theta \cos i, \sin \Omega \cos \theta + \cos \Omega \sin \theta \cos i, \sin \theta \sin i] \tag{23}$$

Since the origin of the reference frame is the center of mass of the satellite, these forces will only be used to compute the moment for the attitude equations.

Gravitational Perturbation

Given the initial height and the time-frame of the electrodynamic breaking, the only perturbation to be considered is the effect of Earth oblateness, J_2. Taking East-longitude λ and latitude φ as coordinates, the perturbational acceleration is:

$$a_r = -3\epsilon \frac{1 - 3\sin^2 \varphi}{r^4}, \qquad a_\lambda = 0, \qquad a_\varphi = -6\epsilon \frac{\sin \varphi \cos \varphi}{r^4} \tag{24}$$

where $\epsilon = \frac{\mu_\oplus R_\oplus^2 J_2}{2}$. This acceleration must be projected in the inertial axes. $\mathbf{u}_r$ is already known, since it is the same as that of the orbital axes. $\mathbf{u}_\varphi$ can easily be obtained from $\mathbf{u}_r$, being rotated 90° North-wards:

$$\mathbf{u}_\varphi = \left[-(\mathbf{u}_r)_x \cdot (\mathbf{u}_r)_x, -(\mathbf{u}_r)_z \cdot (\mathbf{u}_r)_y, (\mathbf{u}_r)_x^2 + (\mathbf{u}_r)_y^2 \right] / \sqrt{1 - (\mathbf{u}_r)_z^2} \tag{25}$$

Geomagnetic Field

The tilted dipole model will be used:

$$\mathbf{B} = \frac{\mu_m}{a^3}\left[\mathbf{u}_m - 3\left(\mathbf{u}_m \cdot \mathbf{u}_r\right)\ \mathbf{u}_r\right] \tag{26}$$

where $\mathbf{u}_m$, projected in S_E, is:

$$\mathbf{u}_m = [\sin\beta_m, 0, \cos\beta_m] \tag{27}$$

The rotation matrix from S_E to S_1 is:

$$\mathsf{A}_m = \begin{bmatrix} \cos(\alpha_m + \Omega_E\, t) & \sin(\alpha_m + \Omega_E\, t) & 0 \\ -\sin(\alpha_m + \Omega_E\, t) & \cos(\alpha_m + \Omega_E\, t) & 0 \\ 0 & 0 & 1 \end{bmatrix} \tag{28}$$

where α_m is the East longitude of the magnetic South Pole, β_m its co-latitude, and Ω_E the Earth's rotation rate. The expression of B in inertial axes is rather involved, since $\mathbf{u}_m$ must be multiplied by $\mathsf{A}_m^{\mathsf{T}}$ and $\mathbf{u}_r$ by B. Its components will be referred to as $[B_x, B_y, B_z]$.

Electrodynamic Force

A contactor and power supply at the satellite core permits switching on and off each individual tether. When the power is on, electrons collected along the tether are ejected at the central contactor, so that the intensity distribution falls linearly from a maximum at the satellite to zero at the tether tip, as shown in Figure 11.6.

Under OML regime [11], the intensity collected by the bare tether will be a function of density of free electrons, tether perimeter, bias, etc.:

$$I_0 = \frac{p}{\pi} L e N_\infty \sqrt{\frac{2e\Phi_a}{m_e}} \tag{29}$$

Φ_a will be approximately the same as the applied bias, 200 V, $L = 100$ m, and perimeter $p = 20$ cm, while the free electron density N_∞ is dependent on time and location. The IRI95 model will be used for computations. In the numerical integration, the value of N_∞ and I_0 will be computed at 5° intervals of orbital anomaly.

The force over an element of tether is: $d\mathbf{F} = I d\mathbf{l} \wedge \mathbf{B}$. Since the current distribution along the tether is $I(x) = I_0(L - x)/L$, the total force over tether i, of length L and direction $\mathbf{u}_i$, is:

$$\mathbf{F}_i = \frac{I_0 L}{2}\mathbf{u}_i \wedge \mathbf{B} \tag{30}$$

where L is short enough for B to be considered constant along the tether.

Since tethers can be switched on and off individually, only one of each opposing pair (x_2 and $-x_2$, y_2 and $-y_2$) would be on at a given time: the one whose force produces drag, as shown in Figure 11.9. Taking two adjacent tethers, the forces can be written as:

$$\begin{aligned} \mathbf{F}_1 &= \tfrac{I_0 L}{2}\mathbf{i}_2 \wedge \mathbf{B}\left[-\text{sign}\left(\mathbf{i}_2 \wedge \mathbf{B} \cdot \mathbf{v}\right)\right] \\ \mathbf{F}_2 &= \tfrac{I_0 L}{2}\mathbf{j}_2 \wedge \mathbf{B}\left[-\text{sign}\left(\mathbf{j}_2 \wedge \mathbf{B} \cdot \mathbf{v}\right)\right] \end{aligned} \tag{31}$$

In order to compute the acceleration, all vectors must be projected in inertial axes: $\mathbf{i}_2$ and $\mathbf{j}_2$ through A, $\mathbf{v} = v\mathbf{u}_\theta$ through B, and B through A_m.

The complete analytical expression of the force as a function of the orbital parameters, geomagnetic parameters, Euler angles and time is too complex in the general case. For the numerical integration, it is simpler to find individually each vector in the proper axes, and perform the multiplications and additions.

11.3.6 Averaging the Force over One Revolution

The electrodynamic forces in equations (30) depend on the instant position of each tether, that is, on ϕ_3. Since the tether rotation is fast with respect to the other characteristic times in the problem (orbital period, day, characteristic time of orbital elements evolution), the step for numerical integration would be too small. It is interesting to find the average force over one revolution.

A reference frame will be used such that Gy is the velocity direction, $\mathbf{u}_v$, Gyz contains the magnetic field intensity B, and Gx is in the direction of $\mathbf{u}_v \wedge \mathrm{B}$, as shown in Figure 11.10.

The active tether will be projected in the directions u, w determined by the intersection of the tether plane Gx_2y_2 with the new Gyz plane determined by speed and magnetic field intensity:

$$\mathrm{w} = \frac{\mathrm{k}_2 \wedge (\mathrm{u}_v \wedge \mathrm{B})}{|\mathrm{k}_2 \wedge (\mathrm{u}_v \wedge \mathrm{B})|}, \qquad \mathrm{u} = \mathrm{w} \wedge \mathrm{k}_2 \tag{32}$$

such that w is along the intersection of both planes, and u helps form a right-handed frame. The tether will be along the direction:

$$\mathrm{i} = \cos\alpha \mathrm{u} + \sin\alpha \mathrm{w} \tag{33}$$

and the force over the tether will be:

$$\mathrm{F} = \frac{I_0 L}{2}\, \mathrm{i} \wedge \mathrm{B} = \frac{I_0 L}{2} \left[\cos\alpha\, (\mathrm{u} \wedge \mathrm{B}) + \sin\alpha\, (\mathrm{w} \wedge \mathrm{B})\right] \tag{34}$$

It can be shown that this force is always opposed to v while the tether is in the u side of the v and B plane. The scalar product $\mathrm{v} \cdot \mathrm{F}$ leads to the expression:

$$\mathrm{v} \cdot \mathrm{F} = I_0 L\, |\mathrm{B}|\, \cos\alpha \left(-\cos^2 c - \cos^2 b + 2\cos a \cos b \cos c\right)/2 \tag{35}$$

where $a = \langle \mathrm{v}, \mathrm{B} \rangle$, $b = \langle \mathrm{k}_2, \mathrm{B} \rangle$, and $c = \langle \mathrm{v}, \mathrm{k}_2 \rangle$. Applying the formulas for spherical triangles, it can be shown that the expression between parentheses is always negative, and therefore the tether produces drag for $\alpha \in [-\pi/2, \pi/2]$. Outside of this range, the opposite tether would be activated.

The force can be averaged over one half revolution:

$$\langle \mathrm{F} \rangle = \frac{1}{\pi} \int_{-\pi/2}^{+\pi/2} \mathrm{F} d\alpha = \frac{I_0 L}{\pi}\, \mathrm{u} \wedge \mathrm{B} \tag{36}$$

Over the next half revolution, the opposite tether would continue giving the same average force. Since there are two pairs of tethers, the total average force would be twice this amount. Obviously the vectors must be projected in the inertial axes through the appropriate rotation matrices.

This allows the use of greater integration steps, since now the smaller characteristic time is the orbital period. The use of the average force requires that the rotation speed be high, so that v and B can be considered constant over one revolution.

11.3.7 Averaging the Force over One Orbit

In order to compare the effectiveness of the method with other schemes, the drag force can be averaged over one orbit. Because of the complexity of the expressions of B, v, and the other

terms in the force, this is done for the simplest case: $i = 90°$; besides, Ω can be made 0 because its effect will be averaged out by the Earth's rotation.

For a polar orbit, the product $\mathbf{u} \wedge \mathbf{B} \cdot \mathbf{u}_v$ is:

$$-\frac{4\mu_m \left(2 \sin\beta_m \cos\beta_m \sin\theta \cos\theta - 2\cos^2\beta_m \cos^2\theta + \cos^2\beta_m + \cos^2\theta\right)}{a^3 |2 \sin\beta_m \cos\theta + 2 \sin\theta \cos\beta_m|}$$

which can be integrated over the interval $\theta = [-\beta_m, -\beta_m + 2\pi]$ to give $-8\mu_m/a^3$. Since there are two active tethers, the average drag force for the polar orbit is:

$$\langle F \rangle = -8\frac{I_0 \mu_m}{\pi^2 a^3} = -16\frac{\tilde{I}\mu_m}{\pi^2 a^3} \tag{37}$$

which is a factor of only $4/\pi$ greater than the two mast system, at the expense of twice the mass. This result would apply to the zero-torque case as well, with the corresponding $\tilde{I}$ and tether length.

11.3.8 External Moments

Gravity and electrodynamic forces will produce moments. Inertia forces will not be included because the reference frame considered does not rotate.

Gravitational Moment

As is well known, the moment in G of the gravitational forces is:

$$\mathbf{M}_{gi} = \frac{3\mu_\oplus}{a^3}\, \mathbf{u}_r \wedge (\mathbf{I}_G \cdot \mathbf{u}_r) \tag{38}$$

the cross product is simple in stroboscopic axes: $I_0 \left[u_y u_z, -u_x u_z, 0\right]$, but the expression of $\mathbf{u}_r$ in those axes, as a function of orbital elements and Euler angles, is rather involved:

$$\mathbf{u}_r|_0 = \mathbf{C}^\mathsf{T} \cdot \mathbf{B} \cdot [1, 0, 0] \tag{39}$$

Again, it is better not to obtain the full expression, but proceed by intermediate results in the numerical integration.

Electrodynamic Moment

The requirement that electrodynamic forces always produce drag results in switching and the use of the sign function in the force expression. Forces can be averaged over one revolution in order to avoid the switching function and dependence on ϕ_3. The moment in G, however, does not require averaging, since it is not affected by switching. The moment of the forces along the tether is obtained by integrating $d\mathbf{M}_i = x\mathbf{u}_i \wedge [I(x) dx \mathbf{u}_i \wedge \mathbf{B}]$, which yields:

$$\mathbf{M}_i = \frac{I_0 L^2}{6} \mathbf{u}_i \wedge (\mathbf{u}_i \wedge \mathbf{B}) = \frac{I_0 L^2}{6} (-\mathbf{B}_N) \tag{40}$$

Since the component of the magnetic field normal to the tether, $\mathbf{B}_N$, is the same for both opposing tethers, the result is not affected by which one is active at the moment. It is enough to add the moments of the two pairs, which leads to:

$$\mathbf{M}_m = \frac{L^2 I_0 \mu_m}{6a^3} \begin{Bmatrix} -\cos\phi_2 B_x + (-\sin\phi_1 B_y + \cos\phi_1 B_z) \sin\phi_2 \\ \cos\phi_1 B_y - \sin\phi_1 B_z \\ 2\left[-\sin\phi_2 B_x + (\sin\phi_1 B_y - \cos\phi_1 B_z)\cos\phi_2\right] \end{Bmatrix} \tag{41}$$

where the moment is projected in stroboscopic axes, and B_i are the components of the geomagnetic field in inertial axes computed from equation (26). Note that it does not depend on ϕ_3.

11.3.9 Numerical Integration

The equations for attitude motion and orbital elements evolution are integrated numerically for 100 days and different values of orbital inclination. This is done for an epoch of maximum Solar activity, 1990 (JD2000 -3652), and for a Solar minimum, 1996 (JD2000 -1461).

Initially, the tethered system is set to rotate about the South-North axis (Gz_1) at a rate of 50 times the orbital rate in all cases. This means that the rotation axis is contained in the orbital plane only for the polar orbit. For lower inclinations, the angle of the angular momentum with the orbit normal, ρ, will be precisely i.

Figure 11.11 shows that the system is not directionally stable. For $i = 90°$, the drift is small enough to be considered practically stable. For the other inclinations, there are large excursions that tend to diminish with time.

The behavior of the zero-torque case can still be identified, somewhat altered by the magnetic torque. Excursions can be loosely identified with angular momentum precession. Still, the time needed for the rotation axis to drift is much greater than what is predicted by equation (3) for $k = 50$ and $\rho = \pi/2 - i$.

The reason can be seen in Figure 11.12: rotation $\dot{\phi}_3$ is increasing continuously due to the electrodynamic torque. k is going beyond the values computed in Section 11.2.1. An angular speed $\dot{\phi}_3$ of several rad/s after 100 days, and growing steadily, is really dangerous. Note that it goes beyond the breaking speeds for some materials. Also note that the inertia moment was intentionally enlarged by including tip contactors. Without these, the angular speed would be even higher.

For a polar orbit, which is the best case, the orbit height goes down about 400 km in 100 days. This may seem high, but it should be remembered that satellite mass is very small. For heavier satellites, the results should be scaled down. For lower inclinations, braking efficiency falls as expected. Figure 11.13 shows that the other orbital elements evolve as expected.

At the solar minimum (epoch 1996), the effect of the electrodynamic moment is not enough to keep the rotational motion stable, and the system tumbles even for $i = 90°$, as shown in Figure 11.14 (but is later stabilized, at least for $i = 90°$). This is due to the slower buildup of rotational speed, which is inverted after tumbling, as shown in Figure 11.15.

Besides, the polar orbits are no longer the most efficient for braking. Due to the different distribution of electron density with latitude, lower inclinations yield faster descents, although still much slower than for the Solar maximum.

Two points require further analysis: how fast does the stability of the polar orbit degrade with inclination, and the effect of the direction of the initial rotation on stability. To study the first point, higher inclinations are considered, for maximum and minimum Solar activity.

Figures 11.16 to 11.19 show that, with high Solar activity, stability properties degrade slowly with inclination, and braking efficiency is maintained. But the fast rotational acceleration is maintained, with its effect on breaking stress. The figures also show that drift, though slow, is increasing with time.

For low Solar activity, however, electrodynamic moment is weak and cannot provide enough rotation to stabilize. Then the main effect is the gravitational moment, and behavior follows more closely what was predicted in Section 11.2.1. Rotational speed builds up slowly, and in so doing reduces the precession amplitude. Only for the polar orbit again, after the initial tumbling, is the original behavior recovered, though scaled down both in rotation and in braking efficiency: angular acceleration prevents further tumbling or precession.

As for the direction of the initial rotation, a new run is made with the initial rotation axis contained in the orbital plane. Results are shown in Figures 11.20 to 11.23. Basically, the atti-

tude evolution corresponds to precession about the orbit normal in each case, which is changing with Ω; the electrodynamic moment further complicates attitude evolution. The fact that the rotation axis is initially within the orbital plane does *not* increase stability: since it is *further* from the orbit normal (in non-polar orbits), the angle ρ increases and ϕ_1 and ϕ_2 increase accordingly. Braking efficiency is only slightly affected.

For lower Solar activity, the behavior is the same, but with even less stability and braking efficiency. Lower inclinations continue to perform better than higher ones.

In order to study the influence of rotational speed, a new run is done for $i = 88°$—thus avoiding the special case of the exactly polar orbit—and initial speeds ranging from 25 to 100 times the orbital rate. The second case is thus the same as in Figures 11.16 to 11.19, and can be used as reference.

Initial rotational speed does improve stability, but only marginally. For high inclinations, the initial speed need only be high enough to keep it stable while rotation picks up speed from the electrodynamic moment. It has little effect over braking efficiency, as shown in Figures 11.24 to 11.27. Indeed, the most unstable cases descend faster. The period of precession increases with speed, while amplitude decreases. Still, in all cases a slow growing deviation can be seen, which signals that precession about the orbit normal has not been eliminated: only its period is getting longer and longer.

For low Solar activity, since there is tumbling in all cases, initial speed increases instability: after tumbling, rotation decelerates to zero and starts increasing again in the new direction. The rotation axis does a high-amplitude precession about the orbit normal, and $\dot{\phi}_3$ is lost and useless in this motion. As it later picks up speed, stability increases. But a higher initial speed means a longer period of instability: a longer fall to zero, before it starts to grow again. 50 times the orbital rate seems to be a good initial speed for this combination of weight and moment of inertia.

11.4 Conclusions

- The central contactor, four-boom rotating satellite is not an efficient de-orbit system:
  a) Mass is doubled while effectiveness is only $4/\pi$ times greater.
  b) The satellite is not directionally stable, showing at best a slow precession about the orbit normal.
  c) For high inclinations, a certain degree of stability is achieved through a continuous acceleration of the rotational speed: this leads to high centrifugal stresses and tether tensional fracture.
  d) A high frequency switch is required for the tethers.
- Items a) and b) apply to the five-contactor, four-boom configuration as well. The cons of item c) are reduced, but so are its pros. The major problem is that reversing current does not only requires a switch: it needs turning contactors on and off, a matter of minutes, while a fast rotation needs switching in milliseconds or less.
- The flexible tether configuration suffers the same problems as the boom configuration, plus the additional problem of tether oscillations or winding about the satellite.

References

[1] E. M. Levin. "Stability of the Time-Independent Tethered Motions of Two Bodies in Orbit Under the Action of Gravitational and Aerodynamic Forces". *Komicheskie Issledovanya*, 22(5):675–682, Sep-Oct 1984.

[2] E. M. Levin. "Stability of the Stationary Motions of an Electromagnetic Tether System in Orbit". *Cosmic Research*, ISSN 0010-9525, January 1988.

[3] V.V. Beletsky and E.M. Levin. "Dynamics of the Orbital Cable System". *Acta Astronautica*, 12(5):285–291, 1985.

[4] V.V. Beletsky and E.M. Levin. *Dynamics of Space Tether Systems*. Number 83 in Advances in the Astronautical Sciences. American Astronautical Society, San Diego, CA, 1993.

[5] Junjiro Onoda and Naoyuki Watanabe. "Tethered Satellite Swinging from Atmospheric Gradients". *J. Guidance, Control and Dynamics*, 11(5):477–479, 1988. Nota técnica.

[6] Junjiro Onoda and Naoyuki Watanabe. "Effects of Atmospheric Density Gradient on Control of Tethered Subatellites". *J. Guidance, Control and Dynamics*, 12(3):431–433, May-Jun 1989. Nota técnica.

[7] E.C. Lorenzini, R.D. Estes, M.L. Cosmo, and J. Peláez. "Dynamical, Electrical and Thermal Coupling in a New Class of Electrodynamic Tethered Satellites". In *Proc. AAS/AIAA Space Flight Mechanics Meeting*, number AAS 99-192, Breckenridge, CO, February 1999.

[8] J. Peláez, M. Ruiz, O. López-Rebollal, and E.C. Lorenzini. "On the Radial Oscillation of an Electrodynamic Tether". In *Proc. AAS/AIAA Space Flight Mechanics Meeting*, number AAS 99-194, Breckenridge, CO, February 1999.

[9] V.V. Beletsky. *Essais sur le Mouvement des Corps Cosmiques*. Éditions Mir, Moscow, 1986.

[10] D.E. Gray et al., editors. *American Institute of Physics Handbook*. McGraw Hill, New York, third edition, 1972.

[11] J.R. Sanmartín and R.D. Estes. "Validity of the Orbital-Motion-Limited Regime of Cylindrical Probes". In J.K. Harrison, editor, *Proceedings of the Tether Technology Interchange Meeting*, number NASA/CP-1998-206900, pages 399–417, Huntsville, Alabama, September 1997. NASA Marshall Space Flight Center.

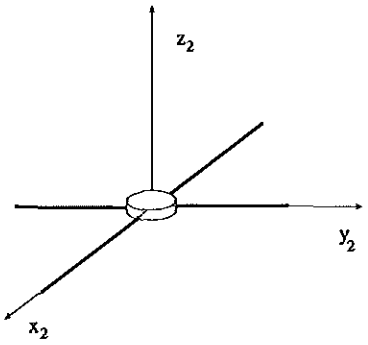

Figure 11.1: Mass distribution of the satellite and tethers

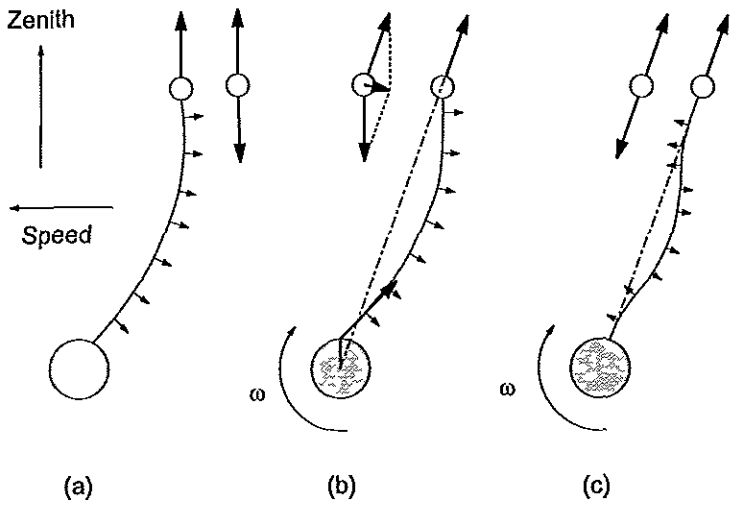

Figure 11.2: Gravity gradient and centrifugal configurations

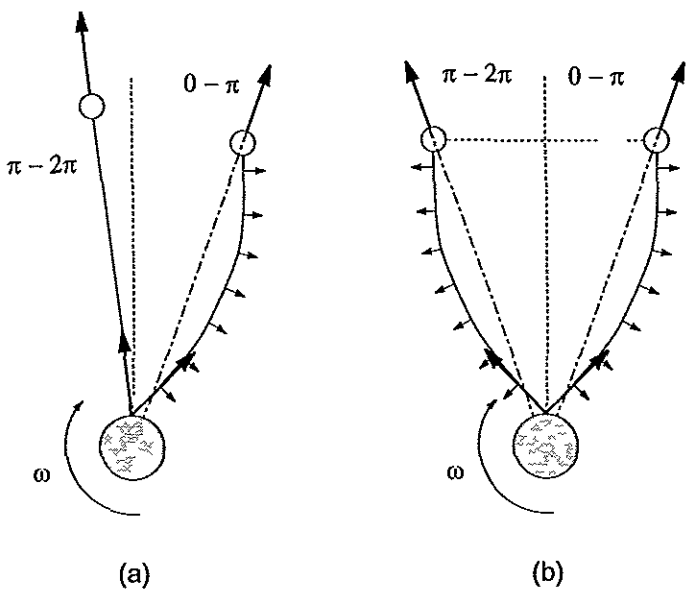

Figure 11.3: Gravity gradient and centrifugal configurations

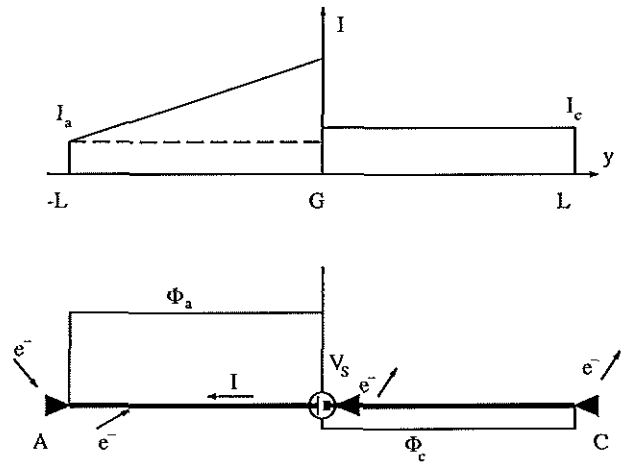

Figure 11.4: Intensity distribution for zero moment

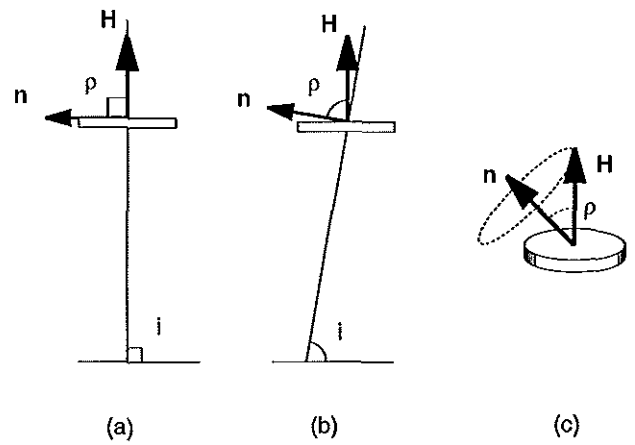

Figure 11.5: Precession of $\mathbf{H}_G$ under gravitational torque

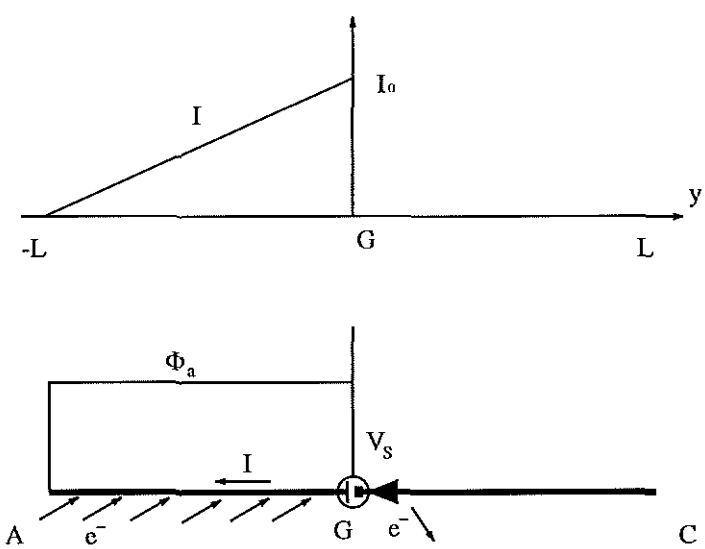

Figure 11.6: Intensity distribution with only one contactor.

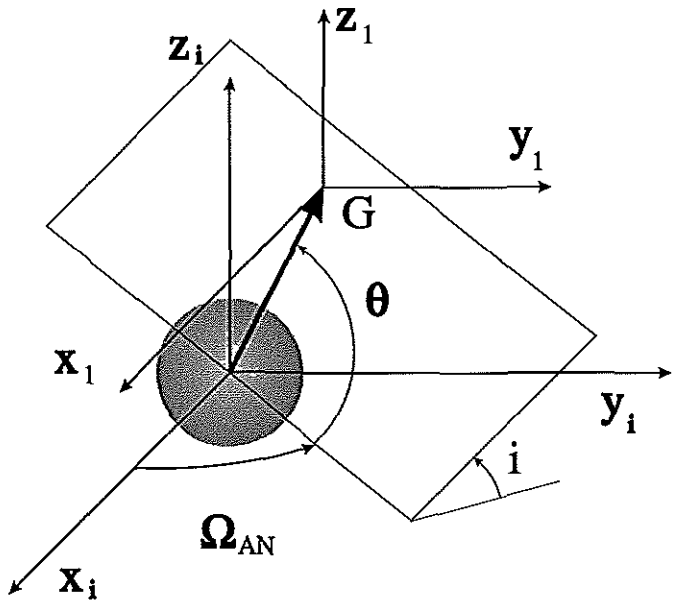

Figure 11.7: Orbital-inertial reference frame

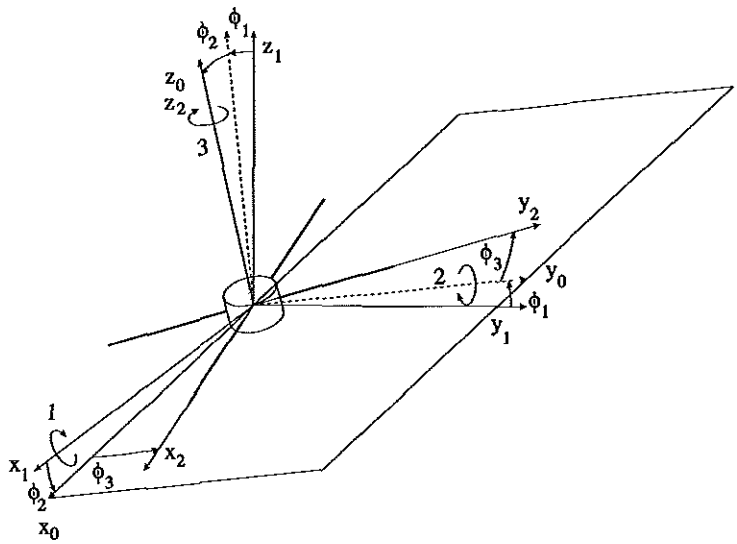

Figure 11.8: 1-2-3 Euler angles

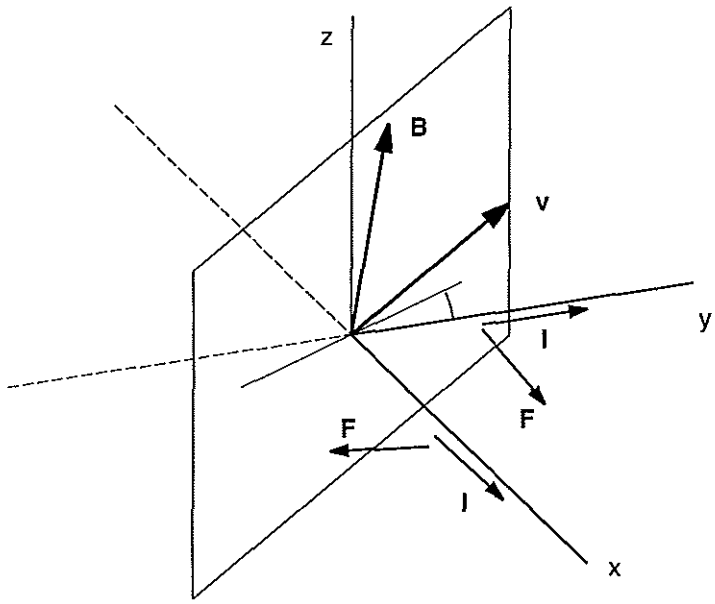

Figure 11.9: Tether orientation and current switching.

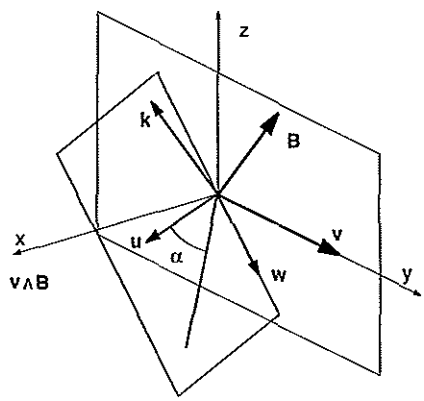

Figure 11.10: Frame for averaging the electrodynamic force

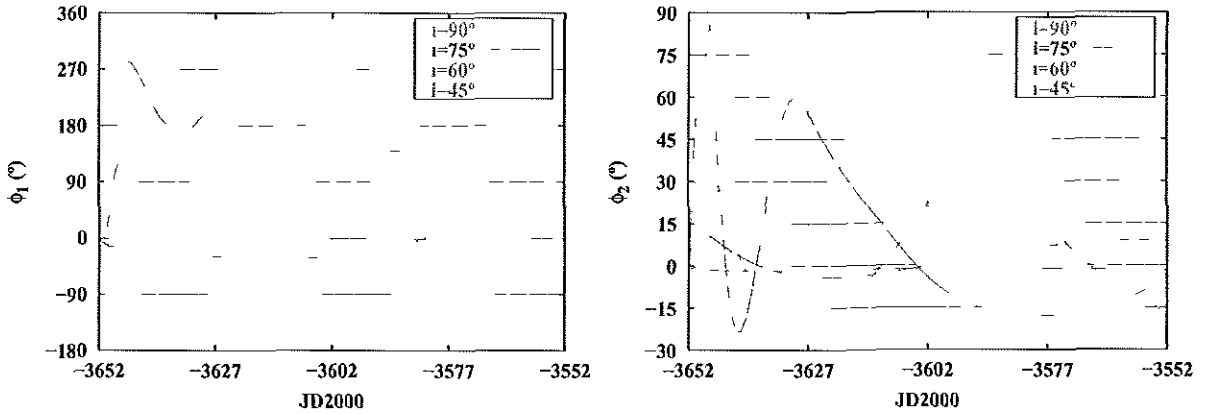

Figure 11.11: Euler Angles for epoch 1990 (Solar maximum)

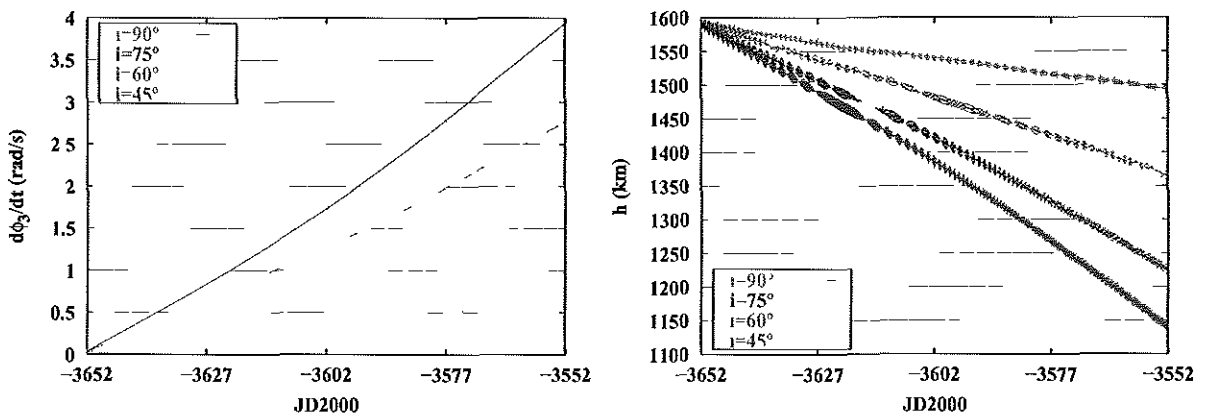

Figure 11.12: Rotation rate and height evolution for Solar maximum

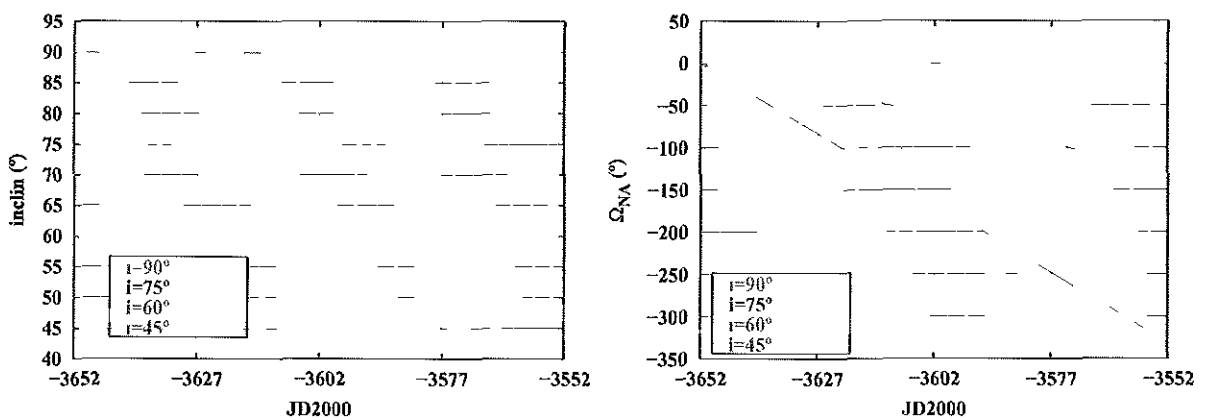

Figure 11.13: Evolution of orbital elements for epoch 1990

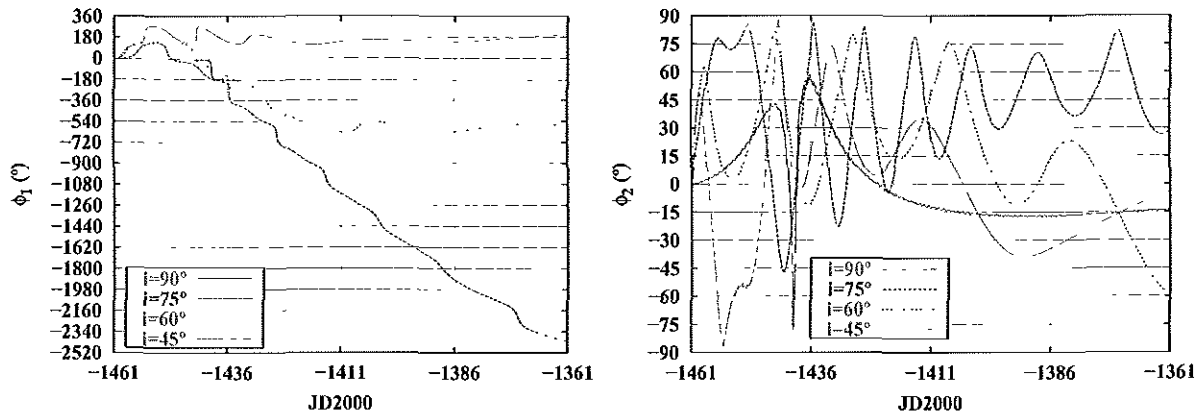

Figure 11.14: Euler Angles for epoch 1996 (Solar minimum)

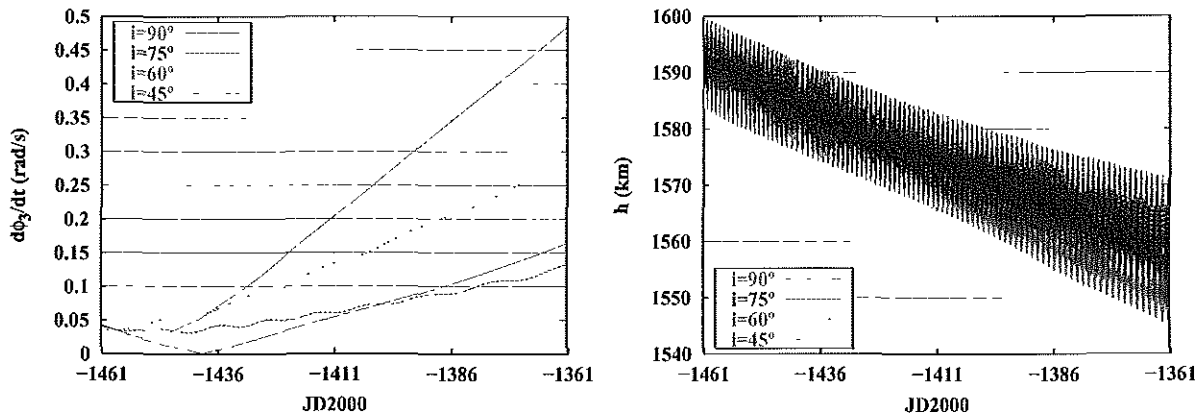

Figure 11.15: Rotation rate increase and height evolution for Solar minimum

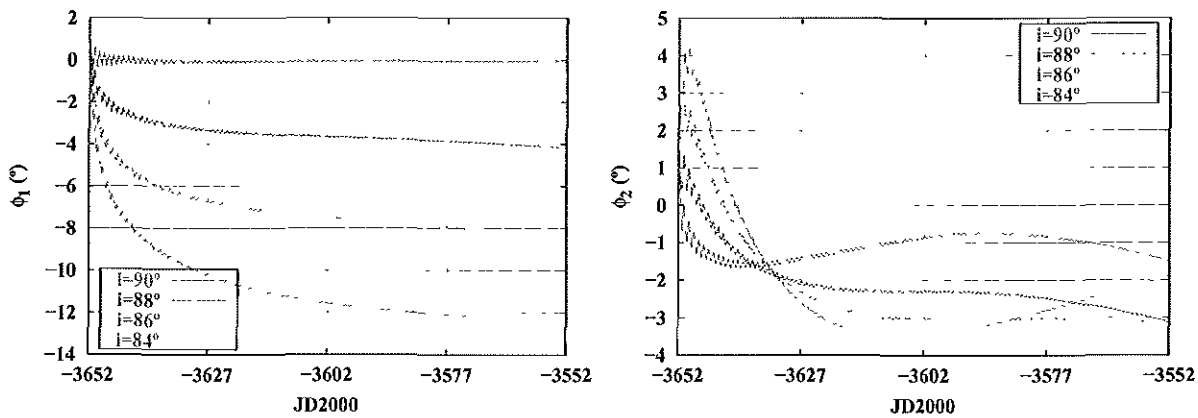

Figure 11.16: Euler Angles for high inclination and Solar maximum

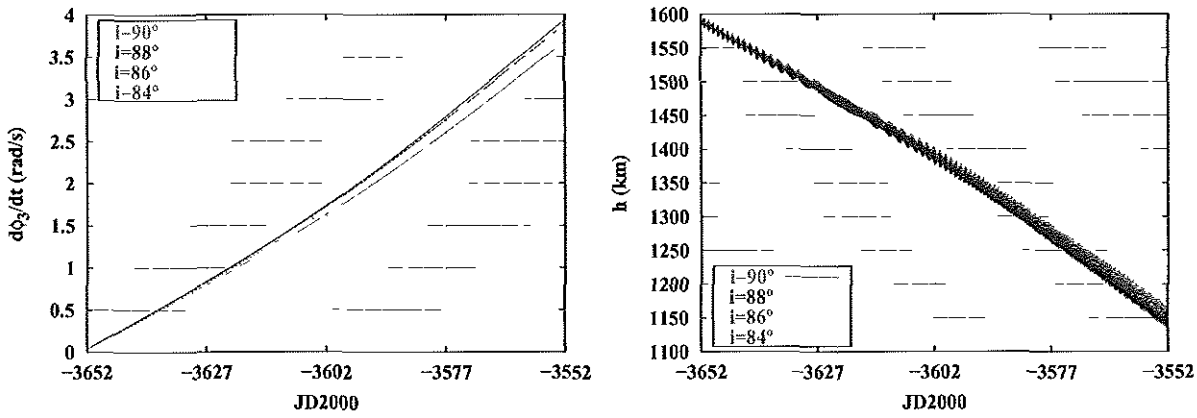

Figure 11.17: Rotation rate and height evolution for high inclination (Solar maximum)

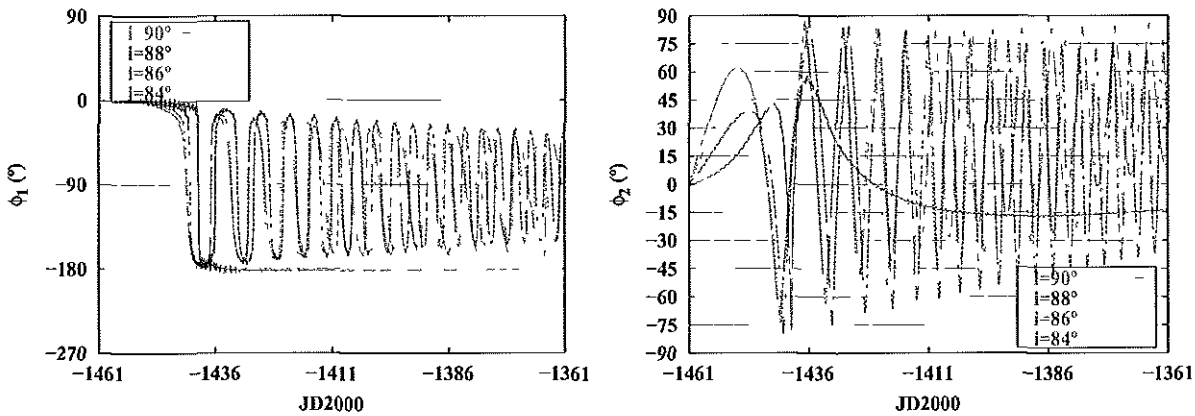

Figure 11.18: Euler Angles for high inclination (Solar minimum)

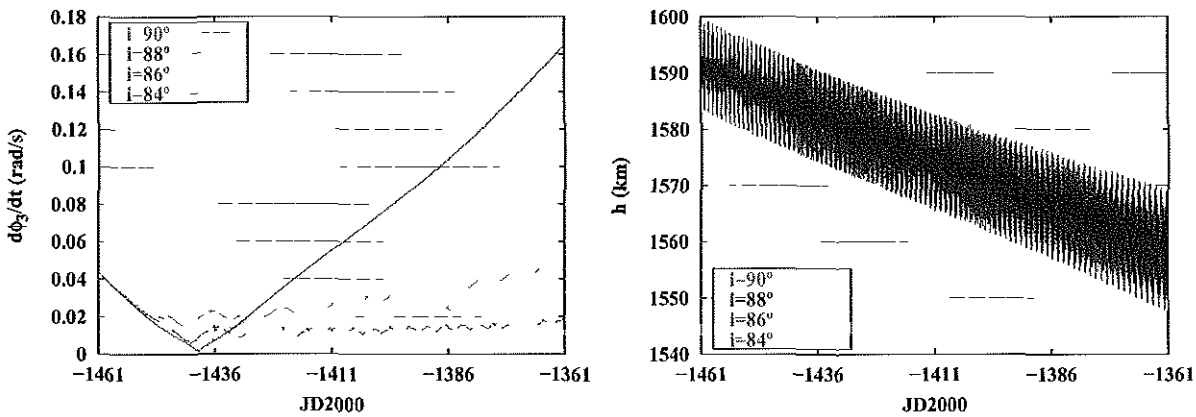

Figure 11.19: Rotation rate and height evolution for high inclination (Solar minimum)

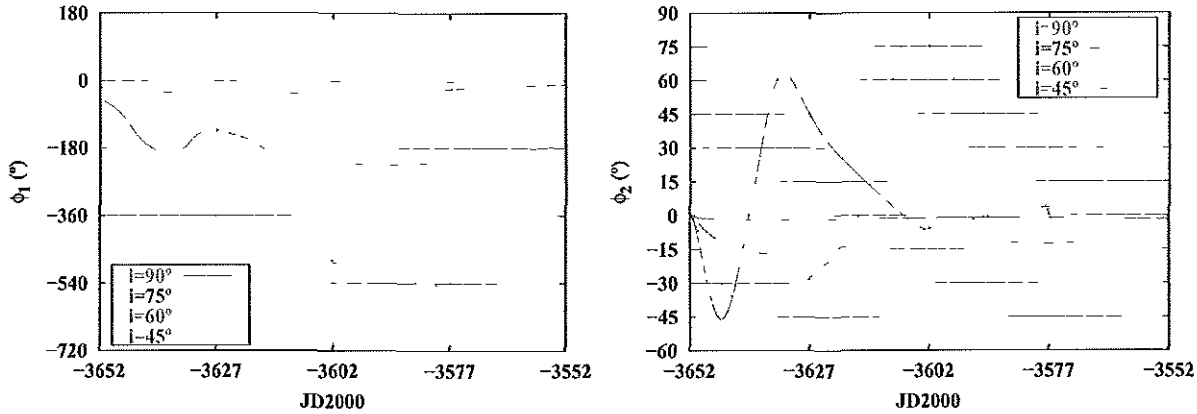

Figure 11.20: Euler Angles for rotation in the orbital plane (Solar maximum)

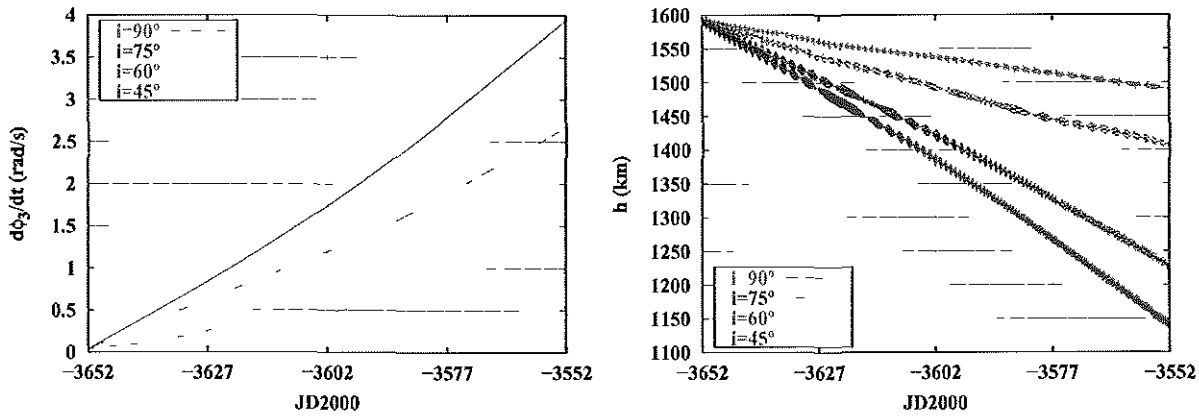

Figure 11.21: Rotation rate and height evolution for rotation in the orbital plane (Solar maximum)

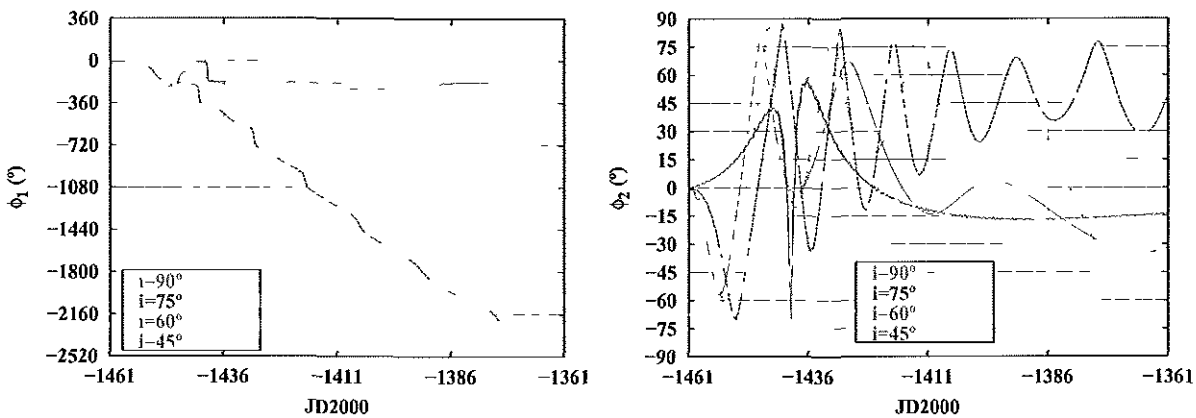

Figure 11.22: Euler Angles for rotation in the orbital plane (Solar minimum)

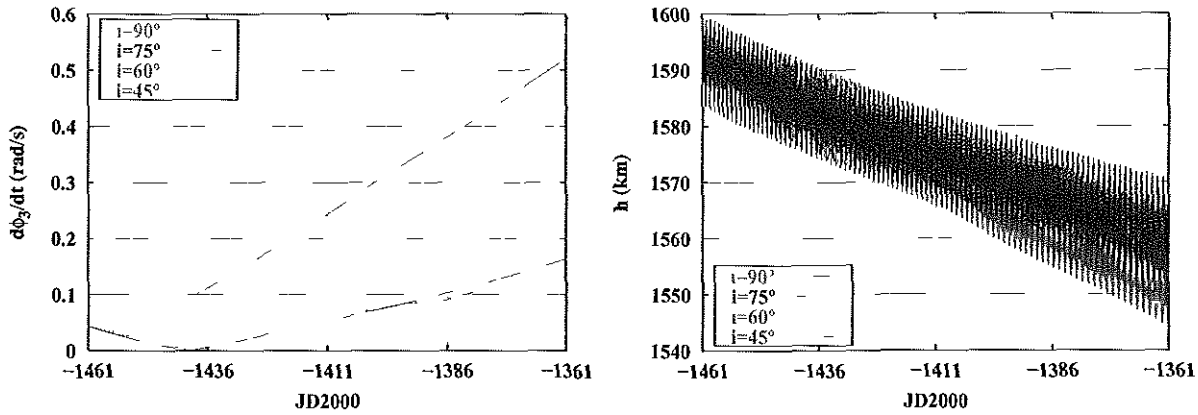

Figure 11.23: Rotation rate and height evolution for rotation in the orbital plane (Solar minimum)

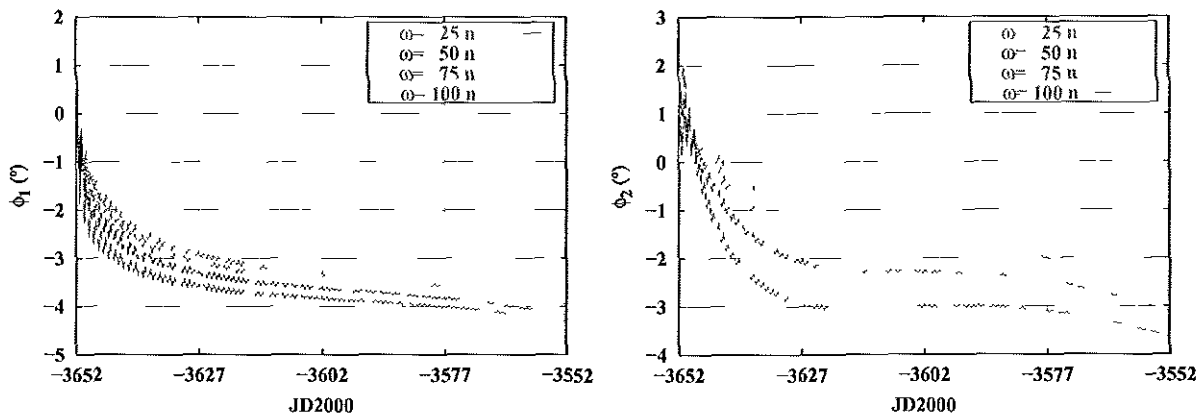

Figure 11.24: Euler Angles for different initial speeds (Solar maximum)

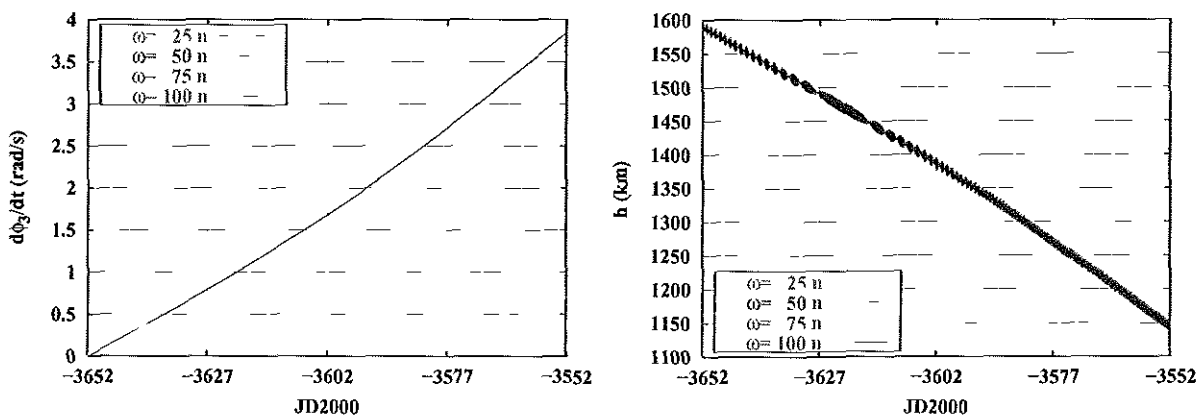

Figure 11.25: Rotation rate and height evolution for for different initial speeds (Solar maximum)

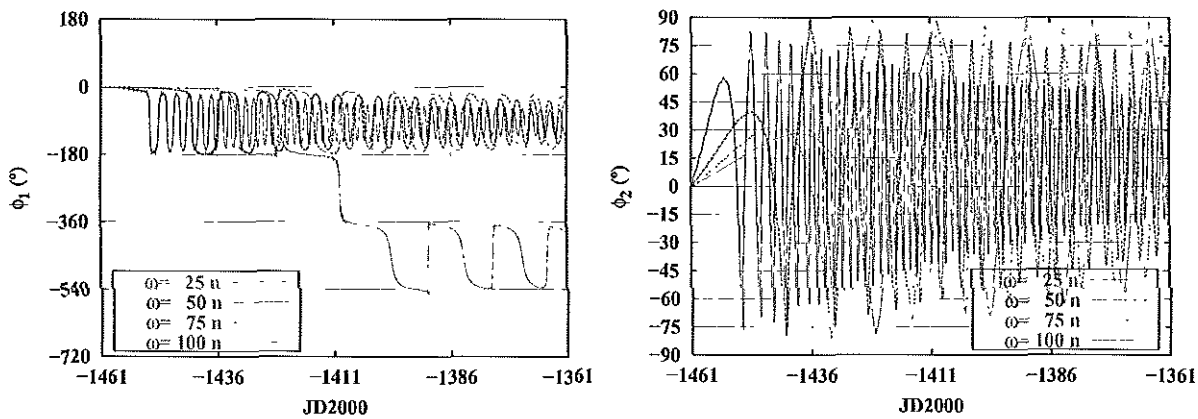

Figure 11.26: Euler Angles for different initial speeds (Solar minimum)

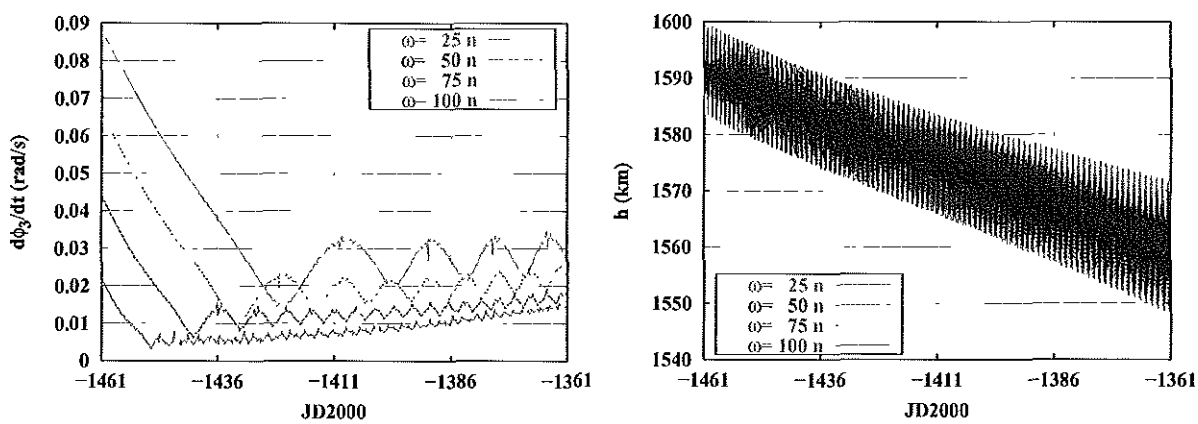

Figure 11.27: Rotation rate and height evolution for different initial speeds (Solar minimum)